Spin and Orbital Ordering in Ternary Transition Metal Oxides

Simon A. J. Kimber

A thesis presented for the degree of
Doctor of Philosophy in the College
of Science and Engineering at the
University of Edinburgh, 2007.

Declaration

I hereby declare that this thesis is of my own composition. It is all my own work, unless otherwise stated, carried out at the University of Edinburgh between September 2004 and September 2007. It has not been submitted for any other degree or professional qualification.

Simon A.J. Kimber

Abstract

Spin and orbital orderings are amongst the most important phenomena in the solid state chemistry of oxides. Physical property and powder neutron and X-ray diffraction measurements are reported for a range of mostly low dimensional ternary transition metal oxides which display spin or orbital order.

Extensive studies of the physical properties and crystal structure of In_2VO_5 are reported. The structure of this material consists of one dimensional zig-zag chains of orbitally ordered S = 1/2 V^{4+}. Magnetic susceptibility measurements show an unusual crossover from dominant ferromagnetic (θ = 17 K) to antiferromagnetic (θ = -70 K) exchange at 120 K, which is attributed to ferromagnetic dimerisation driven by magnetic frustration. The magnetic moment also increases from 1.81 to 2.2μ_B at the 120 K crossover. Heat capacity measurements confirm this scenario as the magnetic entropy tends towards 1/2 Rln3 below 120 K before approximating to Rln2 at high temperature. Synchrotron x-ray diffraction and high resolution neutron powder diffraction show no bulk structural changes, but the ***b*** axis, along which the VO_6 chains run, shows an anomalous expansion below 120 K. At low temperatures, a downturn in the magnetic susceptibility is seen at 2.5 K, signifying a spin freezing transition. Heat capacity and powder neutron diffraction measurements show no evidence for long range magnetic order down to 0.42 K.

The low dimensional brannerite materials MV_2O_6 (M = Mn, Co, Ni) were synthesised by a sol-gel method. Magnetic properties were investigated by magnetisation, powder neutron diffraction and in the case of CoV_2O_6, heat capacity measurements. The structure of these materials consists of linear chains of edge sharing MO_6 octahedra. Monoclinic MnV_2O_6 is an isotropic antiferromagnet with T_N = 20 K and a reduced magnetic coherence length due to 3 % Mn/V antisite disorder. The magnetic structure consists of ferromagnetic edge-sharing chains with **k** = (0,0,1/2) and a refined Mn moment of 4.77(7) μ_B. The triclinic materials CoV_2O_6 and NiV_2O_6 are also antiferromagnetic with T_N = 7 and 14 K respectively and both show metamagnetic type transitions. Unusually, M(H) isotherms recorded below 5 K for CoV_2O_6 show a plateau at 1/3 of the saturation magnetisation. This feature, together with a long period modulated magnetic structure, is attributed to strong single ion (Ising) type anisotropy and nearest neighbour ferromagnetic exchange. Preliminary high pressure experiments on NiV_2O_6 have confirmed a previously reported transition to a columbite phase at 6 GPa and 900 °C. The high pressure polymorph is also antiferromagnetic with T_N = 2.5 K.

The previously uncharacterised perovskite, $PbRuO_3$ has been prepared using high pressure/temperature synthesis techniques (10 GPa, 1000 °C). Synchrotron powder X-ray diffraction measurements show that the room temperature structure is orthorhombic, *Pnma*. A first order orbital ordering transition occurs at 75 K with an associated metal insulator transition. Below 75 K, the d_{xz} orbitals are preferentially occupied and the structure is

orthorhombic *Imma*. The transition may be driven by an increase in antiferroelectric Pb^{2+} displacements, whcih reach a peak at ~ 125 K. A further structural transition to a larger monoclinic cell is also identified at 9.7 K.

The physical properties and crystal structures of two low dimensional lead manganese oxides have also been investigated. Acentric Pb_2MnO_4, which has a structure consisting of edge sharing chains, is antiferromagnetic with T_N = 18 K. Powder neutron diffraction shows the magnetic structure consists of antiferromagnetic chains with **k** = (0,0,0) and a refined Mn moment of 2.74(2) μ_B. The crystal point group allows piezoelectricity and the magnetic point group symmetry allows piezomagnetism. We speculate that coupled magnetic and electric properties may be observed in this material. The layered material, $Pb_3Mn_7O_{15}$, with a structure consisting of 1/2 filled Kagomé layers has also been studied. Single crystals were prepared by a flux growth method and polycrystalline material was prepared by the ceramic method. Powder neutron and synchrotron x-ray diffraction studies show that the single crystals are hexagonal and that the polycrystalline material is orthorhombic. Furthermore, heat capacity measurements show that the hexagonal single crystal material undergoes a glassy magnetic transition. In contrast, powder neutron diffraction shows that the orthorhombic polycrystalline material has coherent long range magnetic order. These differences are attributed to an oxygen deficiency in the polycrystalline material identified by Rietveld refinement of powder neutron diffraction data.

Acknowledgments

I would like to thank my supervisor, Prof. J.P. Attfield and the EPSRC for funding. I would also like to thank the Attfield research group, Dr. J.W.G. Bos, and staff and students of the School of Chemistry and CSEC. Finally, it gives me great pleasure to acknowledge my examiners, Dr. A.V. Powell and Dr. S. Margadonna, for their many useful comments.

For Maria and Simeon

Table of Contents

Chapter 1: Introduction

1.1. Introduction

An isolated d-block cation in an octahedral crystal field has several degrees of freedom, these are illustrated by the case of a cation with configuration t_{2g}^3 e_g^1 as shown in Fig. 1.1.

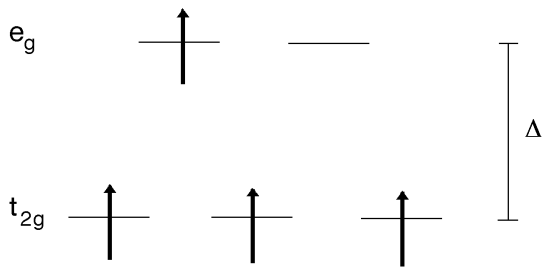

Figure 1.1: Electronic configuration of high spin d^4 cation in octahedral crystal field.

The doubly occupied e_g orbital may be either d_{z2} or d_{x2-y2}, hence there is an *orbital* degree of freedom. Furthermore, if the crystal field splitting, Δ, is comparable to the Hund's rule stabilisation energy, there is an additional ambiguity between high and low spin states. The magnetic moment is also free to point in any direction and represents another *spin* degree of freedom. In the solid state, where a continuous lattice of cations, all with associated degrees of freedom, is formed, several other factors are also important. Some materials with high spin d^4 cations also undergo *charge* disproportionation, for example $CaFeO_3$, which contains a mixture of Fe^{3+} and Fe^{5+} states below room temperature [1]. Finally, all of the above factors may couple with *lattice* degrees of freedom (distortions).

Unravelling the various combinations of *spin*, *orbital*, *charge* and *lattice* degrees of freedom in transition metal compounds is the outstanding problem in solid state chemistry and condensed matter physics [2,3]. The study of transition metal oxides has proven

particularly fruitful in this regard. Several important distinctions between transition metal oxides and transition metal compounds of the heavier chalcoganides or halides can be made. Firstly, synthesis of oxides can be very easy, sometimes only requiring heating the relevant ingredients in air. Secondly, for the heavier transition metals, the oxygen 2*p* level is similar in energy to the metal *d* orbitals and significant hybridisation can occur. The level of hybridisation in the copper oxides in particular, seems to be just right for the emergence of spectacular electronic properties [4].

1.2. Electronic and Magnetic Properties of Transition Metal Oxides

There are two main approaches to solid state chemistry research, optimising technologically useful properties and more fundamental investigations into the microscopic couplings responsible. These two approaches are of course, not mutually exclusive, and advances from fundamental research in particular often drive more applied research. It is useful to mention some of the most important research themes in transition metal oxides and to highlight possible technological applications and the underlying physics.

1.2.1. Magnetoresistance

Magnetoresistance, a change in electrical resistance when a magnetic field is applied, is of great practical use for memory devices and emerging spintronic technologies. Typically, artificial structures consisting of very thin layers of metals are used, however it has become clear that many transition metal oxides also show this property. The most famous are the manganite perovskite family. In these mixed valence materials, colossal negative magnetoresistances (CMR) of up to 99.9 % have been reported [5] and attributed to the combination of charge and orbital ordering, double exchange and phase separation [6]. Magnetoresistance in manganite perovskites is observed at rather low temperatures, however, low field magnetoresistance at room temperature has been observed in the ordered double perovskite Sr_2FeMoO_6 [7]. Large magnetoresistances are also found in mixed valence cobalt perovskites [8] and layered ruthenocuprates [9]. The exact mechanisms of

magnetoresistance in oxides are still hotly disputed, and a great deal of experimental research is therefore performed in this area. The search for new systems showing magnetoresistance also continues.

1.2.2. Multiferroics

Magnetoelectric multiferroic materials show the coexistence of ferroelectricity and (anti)ferromagnetism and coupling between electrical and magnetic order parameters[10]. Controlling electrical polarisation with magnetic field (or vice versa) allows the development of new devices [11]. Classically, a spontaneous polarisation requires an acentric, polar crystal structure, for example α-quartz and magnetism requires unpaired electrons. However, insulating polar ferromagnets in particular, are very rare and much research focuses on novel routes to ferroelectricity. Similarly to magnetoresistive materials, artificial composites are most suitable for real world applications, however several materials that show the coexistence of these properties in a single phase have been studied. In materials with centrosymmetric crystal structures, incommensurate magnetic ordering can induce ferroelectricity. Well known examples include the perovskite $TbMnO_3$, which has a sinusoidaly, modulated magnetic structure [12]. Determining the centricity of potential multiferroic materials can be difficult, for example $BiMnO_3$ was widely held to be ferromagnetic and polar, yet recent diffraction measurements show it to be centrosymmetric [13].

.

1.2.3. Superconductivity

In the superconducting state, electrons are paired and condensed into a superfluid state, which shows zero resistance. These materials thus have obvious applications for generating large magnetic fields and for transporting large currents. Conventional phonon mediated BCS superconductivity is found at very low temperatures in materials such as lead [14], the most spectacular effects are once more found in the transition metal oxides. The discovery of high temperature superconductivity in the layered perovskite copper oxides [15] has prompted more research into oxides than any other single observation. Although the factors that maximise superconductivity in these systems are well known [16], no

accepted theory yet exists. Despite the focus on cuprate materials, new and surprising oxide superconductors are still found, of which the exotic triplet superconductivity found in Sr_2RuO_4 is a notable example [17]. Superconductivity at ~ 5 K has also been found in $Na_xCoO_2.yH_2O$ (x ≈ 0.35, y ≈ 1.3) which has a layered triangular lattice structure {18].

1.1.4. Charge order

Another important electronic instability is charge order. Although not a physical property *per se*, it has been strongly implicated in phenomena such as CMR and superconductivity and is often found as a competing groundstate in these systems. Charge order is the long range order of different oxidation states in systems where the stoichiometry enforces a non-integral value, for example $La_{0.5}Ca_{0.5}MnO_3$. In the case of the half doped manganites, the average manganese oxidation state would be $Mn^{3.5+}$. Diffraction studies evidence two distinct manganese sites with valences close to Mn^{3+} and Mn^{4+} [19]. Examples of charge order are known for nearly all the first row transition metals, the most famous of which is magnetite (Fe_3O_4). This spinel undergoes a first order resistive transition at ~ 120 K which is accompanied by the charge ordering of Fe^{2+} and Fe^{3+} on the B-site spinel sublattice [20,21]. Charge ordering has also been found in vanadates such as NaV_2O_5 [22] and recently, the cuprate chain compounds $Na_3Cu_2O_4$ and $Na_8Cu_5O_{10}$ [23]. Finally, in centrosymmetric compounds such as $LuFe_2O_4$ where the charge ordered arrangement has a polar arrangement, ferroelectricity may be observed [24].

1.3. Low Dimensional Vanadates

A very large variety of low dimensional oxides containing vanadium are found. One reason why is the range of oxidation states and coordinations that vanadium can assume [25]. For example, non-magnetic V^{5+} can be found in distorted octahedral and square pyramidal coordination and also tends to form V_2O_5 type blocks that enforce reduced dimensionality in ternary compounds. This tendency to form edge and face sharing arrangements rather than corner sharing structures like perovskites is because V^{5+} is slightly too small for octahedral coordination in oxides. Furthermore, V^{5+} (and V^{4+}) tend to undergo

displacements in octahedral coordination as a result of vanadyl bond formation through *d* – *p* π-bonding. The more reduced vanadium oxidation states also show distorted coordination, e.g. V^{3+}, which typically has distorted octahedral coordination, and V^{4+}, which normally has a characteristic vanadyl type, square pyramidal coordination. Chains and planes with various connectivity's are also frequently found in V^{3+} and V^{4+} compounds and the magnetic properties of these materials are responsible for much of the interest in vanadium oxides, especially given the low magnetic moments. Finally, it is also possible to prepare compositions containing V^{2+}, e.g. VO_x although x is often rather large [26].

The variety of magnetic phenomena found in the vanadates can be illustrated by considering the simple oxides. Metal-insulator transitions are found in both VO_2 and V_2O_3, at 365 and 170 K respectively [27,28]. Diffraction studies have shown that both are accompanied by structural transitions. In the case of VO_2, the high temperature rutile structure is distorted such that the one dimensional chains become dimerised, with a non-magnetic groundstate. This transition has recently been discussed in the framework of a Peierls transition [29]. In V_2O_3, the magnetic ground state is antiferromagnetic, but the structural transition still introduces a weak dimerisation [30].

As mentioned briefly above, many low dimensional structures are found in ternary magnetic vanadates. Of particular interest are compounds with alkali metals, the most studied example of which is α-NaV_2O_5. Initial studies on this material showed a precipitous drop in the magnetic susceptibility at 34 K and possible spin-Peierls behaviour was suggested [31]. Early low temperature diffraction measurements supported this picture as a complex superstructure was observed [32]. However, the consensus today is that this compound is actually charge ordered at low temperature [33]. The reason why confusion arose is the complex crystal structure, which consists of two types of chains, wrongly assumed to be segregated into V^{5+} and V^{4+} at high temperature. Additionally, and unusually, the high temperature valence mixed phase is insulating. The low temperature charge ordered structure is one of the most complex solved to date, with a very large cell and a large number of V sites [34]. A large number of vanadates with alkaline earth metals are also known, several of which also show unusual magnetic properties. The two dimensional system CaV_4O_9 has attracted much attention in this regard, as magnetic susceptibility

measurements show a spin gap at low temperature [35] The crystal structure of this material consists of plaquettes of four V^{4+} cations, unusually, the magnetic properties can be rationalised by a model of singlet formation amongst all four moments as opposed to simple dimer formation [36-38]. Finally, several spin ladder systems are also known amongst the alkaline earth vanadates. Both MgV_2O_5 and CaV_2O_5 also show a spin gap at low temperature [39].

1.4. Outlook

Most of the 'headline' properties outlined above are not yet fully understood, and characterising the electronic and magnetic properties of materials for which only a crystal structure exists is one way of searching for new examples. The combination of cations with active degrees of freedom and interesting structural motifs is likely to lead to interesting properties and the materials studied herein were chosen on this basis. These reasons are summarised below:

In_2VO_5:

This compound has the combination of reduced dimensionality (pseudo-1D), low moment ($\mathbf{S} = 1/2$) and frustration thought to favour unusual magnetic ground states.

MV_2O_6 (M = Mn, Co, Ni):

These compounds have pseudo-one dimensional structures, and in the case of CoV_2O_6 strong single ion anisotropy.

$PbRuO_3$:

This perovskite was chosen for study as it is orbitally degenerate and because the 4d electrons in ruthenates are on the borderline of localised and itinerant behaviour. Furthermore, the Pb^{2+} cation has a stereoactive lone pair.

Pb_2MnO_4 and $Pb_3Mn_7O_{15}$:

Selected because of the presence of stereoactive Pb^{2+} and mixed valence in the case of $Pb_3Mn_7O_{15}$.

References

[1] P.M. Woodward, D.E. Cox, E. Moshopoulo, A.W. Sleight, S. Morimoto, *Phys. Rev. B*, **62**, 844 (2000)

[2] Y. Tokura, N. Nagaosa, *Science*, **288**, 462 (2000)

[3] M. Imada, A. Fujimori, Y. Tokura, *Rev. Mod. Phys.*, **70**, 1039 (1998)

[4] F.C. Zhang, T.M. Rice, *Phys. Rev. B*, **37**, 3759 (1988)

[5] S. Jin, T.H. Tiefel, M. McCormack, R.A. Fastnacht, R. Ramesh, L.H. Chen, *Science*, **264**, 413 (1994)

[6] H.Y. Hwang, S.W. Cheong, P.G. Radaelli, M. Marezio, B. Batlogg, *Phys. Rev. Lett.*, **75**, 914 (1995)

[7] K.L. Kobayashi, T. Kimura, H. Sawada, K. Terakura, Y. Tokura, *Nature*, **395**, 677 (1998)

[8] R. Caciuffo, D. Rinaldi, G. Barucca, J. Mira, J. Rivas, M.A. Senaris-Rodriguez, P.G. Radaelli. D. Fiorani, J.B. Goodenough, *Phys. Rev. B*, **59**, 1068 (1999)

[9] A.C. Mclaughlin, L. Begg, C. Harrow, S.A.J. Kimber, F. Sher, J.P. Attfield, *J. Amer. Chem. Soc.*, **128**, 12364 (2006)

[10] M. Fiebig, *J. Phys. D: Appl. Phys*,**38**, R123 (2005)

[11] V.E. Wood, A.E. Austin, *Int. J. Magn*, **5**, 303 (1973)

[12] T. Kimura, T. Goto, H. Shintani, K. Ishizaka, T. Arima, Y. Tokura, *Nature*, **426**, 55 (2003)

[13] E. Montanari, G. Calestani, L. Righi, E. Gilioli, F. Bolzoni, K.S. Knight, P.G. Radaelli, *Phys. Rev. B*, **75**, 220101 (2007)

[14] J. Bardeen, L.N. Cooper, J.R. Schrieffer, *Phys. Rev.*, **108**, 1175 (1957)

[15] J.G. Bednorz, K.A. Muller, *Zeit. Phys. B*, **64**, 189 (1986)

[16] P.W. Anderson, *Science*, **235**, 1196 (1987)

[17] Y. Maeno, H. Hashimoto, K. Yoshida, S. Nishizaki, T. Fujita, J.G. Bednorz, F. Lichtenberg, *Nature*, **372**, 532 (1994)

[18] K. Takada, H. Sakurai, E. Takayama-Muromachi, F. Izumi, R.A. Dilanian, T. Sasaki, *Nature*, **422**, 53 (2003)

[19] P.G. Radaelli. D.E. Cox, M. Marezio. S-W. Cheong, P.E. Schiffer, A.P. Ramirez, *Phys. Rev. Lett.*, **75**, 4488 (1995)

[20] E.J.W. Verwey, *Nature*, **144**, 327 (1939)

[21] J.P. Wright, J.P. Attfield, P.G. Radaelli, *Phys. Rev. Lett.*, **87**, 266401 (2001)

[22] H. Sawa, E. Ninomiya, T. Ohama, H. Nakao, K. Ohwada, Y. Murakami, Y. Fujii, Y. Noda, M. Isobe, Y. Ueda, *J. Phys. Soc. J.*, **71**, 385 (2002)

[23] P. Horsch, M. Sofin, M. Mayr, M. Jansen, *Phys. Rev. Lett.*, **94**, 076403 (2005)

[24] N. Ikeda, H. Ohsumi, K. Ohwada, K. Ishii, T. Inami, K. Kakurai, Y. Murakami, K. Yoshii, S. Mori, Y. Horibe, H. Hito, *Nature*, **436**, 1136 (2005)

[25] P.Y. Zavalij, M.S. Whittingham, *Acta Cryst.*, **B55**, 627 (1999)

[26] J.B. Goodenough, *Ann. Rev. Mat. Sci.*, **1**, 101 (1971)

[27] C.N. Berglund, H.J. Guggenheim, *Phys. Rev.*, **185**, 1022 (1965)

[28] R.M. Moon, *Phys. Rev. Lett.*, **25**, 527 (1970)

[29] M.W. Haverkort, Z. Hu, A. Tanaka, W. Reichelt, S.V. Streltsov, M.A. Korotin, V.I. Ansimov, H.H. Hsieh, H.-J. Lin, C.T. Chen, D.I. Khomskii, L.H. Tjeng, *Phys. Rev. Lett.*, **95**, 196404 (2005)

[30] D.B. Mcwhan, J.P. Remeika, *Phys. Rev. B*, **2**, 3734 (1970)

[31] M. Isobe, Y. Ueda, *J. Phys. Soc. J*, **65**, 1178 (1996)

[32] Y. Fujii, H. Nakao, T. Yosihama, M. Nishi, K. Nakajima, K. Kakurai, M. Isobe, Y. Ueda, H. Sawa, *J. Phys. Soc. J*, **66**, 326 (1997)

[33] H. Seo, H. Fukuyama, *J. Phy. Soc. J*, **67**, 2602 (1998)

[34] J. Ludecke, A. Jobst, S. van Smaalen, E. Morre, C. Geibel, H.G. Krane, *Phys. Rev. Lett.*, **82**, 3633 (1999)

[35] S. Taniguchi, T. Nishikawa, Y. Yasui, Y. Kobayashi, M. Sato, T. Nishioka, M. Kontani, K. Sano, *J. Phys. Soc. J.*, **64**, 2758 (1995)

[36] N. Katoh, M. Imada, *J. Phys. Soc. J.*, **64**, 4105 (1995)

[37] S.R. White, *Phys. Rev. Lett.*, **77**, 3633 (1996)

[38] W.E. Pickett, *Phys. Rev. Lett.*, **79**, 1746 (1997)

[39] Y. Ueda, *Chem. Mat.*, **10**, 2653 (1998)

Chapter 2

Theory and Methods

2.1. Solid State Synthesis

Transition metal oxides are typically synthesised by the ceramic method. Common precursors include pure elemental powders, oxides and carbonates. Reagents are finely ground in a pestle and mortar then pelleted under moderate pressure. The reagents are then reacted at high temperature for long periods of time. The ceramic method requires such harsh conditions because of limited ionic diffusion in the solid state and the strong, continuous bonding in oxides. Consider the reaction to prepare spinel, typically performed at ca. 1500 °C:

$$MgO + Al_2O_3 \rightarrow MgAl_2O_4 \tag{2.1}$$

Reaction will initially occur via the interface between MgO and Al_2O_3, however, as soon as a layer of product is formed the reaction is limited by cation diffusion through $MgAl_2O_4$. In practice, defects play a key role in cation transport and give a characteristic parabolic increase in the thickness of the product layer with time [1]. The above example highlights the importance of reagent particle size and homogeneity, synthetic strategies have evolved to reduce particle size and to provide reagent mixtures mixed on an atomic scale [2]. Examples include the sol-gel method, where soluble precursors are dissolved in water with an excess of a chelating agent (e.g. citric acid) The resulting solution is reduced to a thick gel then calcined at low temperature to remove the organic chelating agent. The product of this process is then reacted by the ceramic method, often at considerably lower temperatures and for shorter periods. An excellent demonstration is the synthesis of $MgAl_2O_4$ from an aluminium magnesium n-butoxide in the presence of polyethylene glycol, this method provides a pure product using a reaction temperature of 700 °C [3].

By utilising high pressure techniques, compounds can be synthesised with transition metals in unusual oxidation states or coordinations [4]. Examples include Sr_2FeO_4 (Fe^{4+}), synthesised under high oxygen pressure [5] or $SrCrO_3$ (octahedral Cr^{4+}) synthesised at 6 GPa and 800 °C. [6]. A uniaxial press equipped with a Walker multianvil module was used with the aid of Dr J. Rogers (University of Edinburgh) to synthesise two of the compounds studied in this thesis, the experimental setup is shown below [7}:

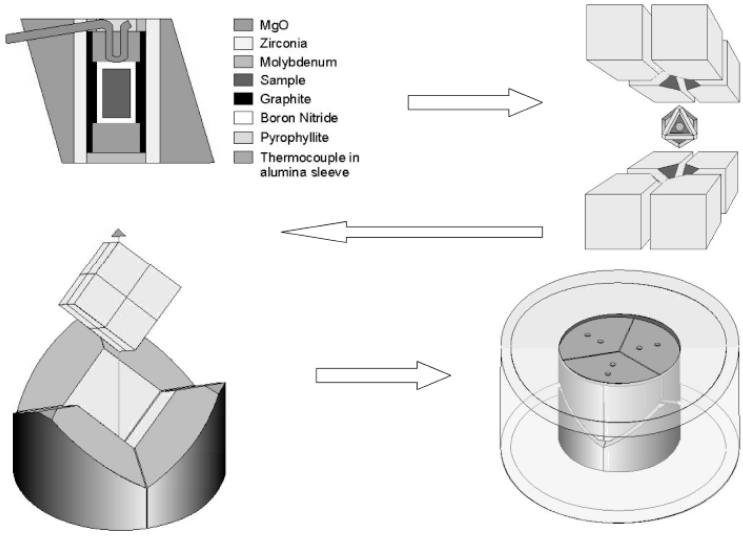

Figure 2.1: High pressure walker module setup.

The sample is placed in a BN capsule, which is placed in a graphite or $LaCrO_3$ resistive heater. This arrangement is insulated with zircona and placed in a drilled MgO octahedron. The octahedron is gasketed and placed between 8 truncated WC cubes. The resulting cube is then placed between 6 steel wedges and placed in the pressure containment ring. Application of a uniaxial stress yields quasi-hydrostatic conditions at the sample.

2.2. Transport Properties

2.2.1. The Hubbard Model

The electronic properties of simple metals such as sodium or magnesium are well described by the free electron model, which treats the electrons as fully delocalised in broad

bands made up of both *s* and *p* orbitals. For the transition metals, the *d*-orbitals are much less diffuse, more directional, and the bands are correspondingly narrower. Furthermore, in some compounds with partially filled valence shells, insulating behaviour is found. The reason for this discrepancy is that simple band theories ignore the correlations (repulsion) between electrons, which are important for the narrow bands in transition metal oxides. In the Hubbard model, the only correlation between electrons is assumed to be the repulsion between two electrons on the same atom. The energy cost of transferring an electron to a neighbouring atom is U = I – A, where I is the energy required to remove it from its original atom (ionisation energy) and A is the electron affinity of the host atom. When U is large, the electron repulsion renders the partially full band insulating. The variation of the so-called Mott-Hubbard splitting, U, as a function of the bandwidth, W, is shown in Fig. 2.2.

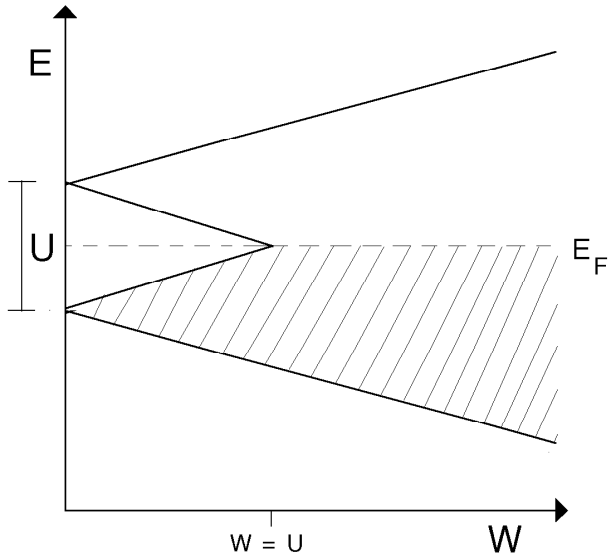

Figure 2.2: Variation of Mott-Hubbard splitting with bandwidth.

Three limiting cases are apparant, when W > > U, band theory applies, when W < < U, ligand theory is appropriate. Finally, W ≈ U, is the strongly correlated regime where many of the most interesting properties of transition metal oxides emerge [8].

2.1.2. Techniques for measuring transport properties

A Quantum Design PPMS system was used for measuring the resistivity of several compounds as a function of temperature. This multipurpose system consists of a superconducting magnet with a maximum field of 9 T and a cryostat/^{3}He cooling system with a base temperature of 0.35 K. The resistivity of samples made at ambient pressure was measured using the standard four probe method, which relies on having a regular, rectangular piece of sample. As this is obviously impossible for samples made at high pressure, the van der Pauw technique was used. This method can be used for a sample of arbitrary shape, as long as it is of constant thickness and four probes are attached to the edge of the sample with small contact sizes. It can be shown that the resistivity, ρ, is given by:

$$\rho = \frac{\pi d}{\ln(2)} . \frac{R_A + R_B}{2} . f(r) \tag{2.2}$$

where d is the sample thickness and R_A and R_B are the resistances of the two bridges. The function, f(r) → 1 when $R_A \approx R_B$ [9]

2.2. Magnetism

All materials respond to an applied magnetic field with induced magnetisation, M, proportional to the applied field, **H**, :

$$M = \chi H \tag{2.3}$$

The dimensionless quantity, χ, is the magnetic susceptibility and represents the magnetic moment induced by a magnetic field per unit volume. Two different classes of materials are found, those containing no unpaired electrons exhibit *diamagnetism*, χ is small and negative and the induced magnetisation repels the applied field. In materials with unpaired electrons (*paramagnets*) χ is positive and the induced magnetisation reinforces an applied field. All materials show diamagnetism, however its contribution to the measured susceptibility of transition metal oxides is generally very small (important exceptions are the contribution of

conduction electrons in metals and the perfect diamagnetism found in superconductors) and can be neglected for all compounds studied in this thesis.

2.2.1. Origin of the magnetic moment

When spin orbit coupling is weak, the energy levels of electrons in an isolated atom are principally influenced by the electrostatic interaction. In this scenario, which describes the lighter elements, Russell-Saunders coupling can be used to determine the overall angular momentum. In this scheme, the individual spin (**s**) and orbital (**l**) angular momentum of the unpaired electrons are summed to give **S** and **L**. The way in which **S** and **L** couple to give **J** is shown in Fig. 2.3. The ground state has degenerate levels between (**L** + **S**) and |**L** – **S**| and the ground state term symbol can be found by application of Hund's rules.

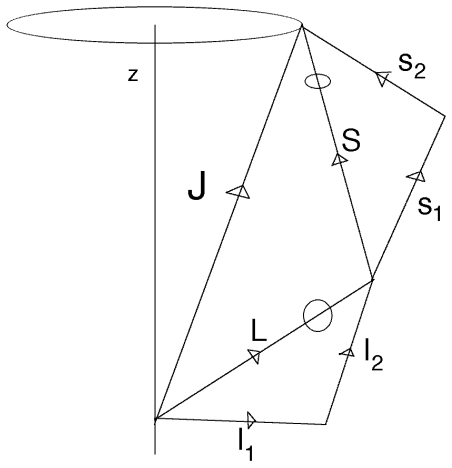

Figure 2.3: Russell-Saunders coupling.

The magnetic moment of an atom with total angular momentum **J** is:

$$\mu_J = g_j \mu_B \sqrt{J(J+1)} \tag{2.4}$$

where:

$$g_j = \frac{3J(J+1) + S(S+1) - L(L+1)}{2J(J+1)} \tag{2.5}$$

Russell-Saunders coupling becomes progressively less accurate as the atomic mass increases because spin orbit coupling increases as ~ Z^4. For the very heaviest elements, the individual spin and orbital angular momenta couple in a process known as jj-coupling.

When a non-interacting assembly of paramagnetic atoms is placed in a magnetic field, **B**, the degenerate ground states splits into (2**J**+1) states separated by $g\mu_B\mathbf{B}$. This is illustrated schematically in Fig. 2.4 for a system with **J** = 3/2.

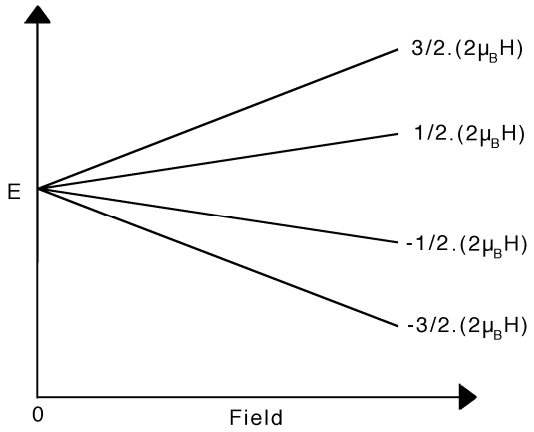

Figure 2.4: Zeeman splitting for atom with **J** = 3/2.

The molar magnetic moment for this system, μ_J, is then given by the a sum over all moments weighted by the Boltzmann factor, where N is Avogadro's number:

$$\langle \mu_J \rangle = N.\frac{\sum_{m=-J}^{+J} g_j \mu_B mB.\exp(-g_j \mu_B B/kT)}{\sum_{m=-J}^{+J} \exp(-g_j \mu_B B/kT)} \tag{2.6}$$

It can be shown [10] that, for modest fields and temperatures:

$$\langle \mu_J \rangle = \frac{{g_j}^2 \mu_B^2 J(J+1)B}{3kT} \tag{2.7}$$

and that the experimentally measured quantity, the magnetic susceptibility (χ) follows the Curie law:

$$\chi = \frac{C}{T} \tag{2.8}$$

where the Curie constant C is:

$$C = \frac{g_j{}^2 \mu_B^2 J(J+1) N_A}{3k} \tag{2.9}$$

2.2.2. Crystal field effects

As the d-orbitals of a transition metal atom are extended, the coordination environment has a pronounced effect on the orbital energy level scheme and by extension the magnetic properties. Consider again the case of a d^3 transition metal cation with term symbol $^4F_{3/2}$, the free ion has a ground state degeneracy of (2S+1) x (2L+1) = 24. The magnetic moment calculated from Eqn. 2.4 is 0.77 μ_B. When the cation is placed in an octahedral crystal field, the orbital degeneracy is partially lifted as the d-orbitals split into the t_{2g} (d_{xy}, $d_{xz,}$,d_{yz}) and e_g (d_{x2-y2}, d_{z2}) sets. The ground state term symbol is $^4A_{2g}$ with a degeneracy of 1. The measured magnetic moment (≈ 3.87 μ_B) is strongly enhanced from the free ion value. This difference in moment can be ascribed to orbital quenching. The rotational symmetry of the free ion allows an electron in any d-orbital to be taken into any other, contributing orbital angular momentum. In the case of an octahedrally coordinated cation, some of this rotational symmetry is lost. In the case of a d^3 ion, orbital angular momentum is further reduced to comply with the Pauli exclusion principle. Quantitative agreement with measured moments for first row transition metals is often found if **J** is replaced by **S** in Eqn. 2.4 and $g_j = g \approx 2$:

$$\mu_{s.o} = g\mu_B \sqrt{S(S+1)} \tag{2.10}$$

Octahedrally coordinated transition metals with E or T symmetry ground states are also often found to undergo structural (Jahn-Teller) distortions, which may be dynamic or static. Small distortions which remove orbital degeneracy are particularly favourable when they involve degenerate e_g orbitals because they point directly at the ligands [11].

2.2.3. Exchange interactions

The energy levels of a system of interacting moments can be expressed using the Heisenberg exchange Hamiltonian:

$$H = -2J_{ij}S_i.S_j \tag{2.11}$$

where **J** is the exchange constant and is positive for a ferromagnetic interaction. The interactions between magnetic moments in an insulating solid can take a number of forms. The simplest is the through space dipolar interaction, which is unimportant for the compounds discussed in this thesis. If orbital overlap between neighbouring magnetic atoms is possible, then direct exchange via t_{2g} orbitals may be significant. Structures that contain edge or face sharing chains of octahedrally coordinated transition metal cations fulfil this condition. The sign of the magnetic exchange and the likely electronic properties are related to the number of t_{2g} electrons (n_{2g}) and the distance between neighbouring cations. In the case of weak cation-cation interactions, materials are often found to be semiconducting with antiferromagnetic exchange if $n_{2g} \leq 3$ or display weak ferromagnetic exchange if $n_{2g} > 3$. Compounds with strong cation-cation interactions have a marked tendency to show metallic type conductivity [12].

Many materials are however found to have widely separated magnetic cations and yet show long range order at surprisingly high temperatures. When two magnetic cations are separated by a diamagnetic anion ligand (e.g. O^{2-}), exchange occurs which can be ascribed to the transfer of electrons between metal and anion orbitals. This process, termed superexchange, has several competing contributions. The first of these, *correlation exchange*, can be visualised as partial bond formation on both sides of the anion and stabilises an

antiferromagnetic groundstate. The second competing mechanism, *kinetic exchange*, is the transfer of an electron from one cation to the other and also favours an antiferromagnetic groundstate. The third major contributor to superexchange is the *polarisation* term, which is the transfer of an electron from a ligand orbital to an empty cation orbital resulting in ferromagnetic exchange.. The balance of these factors depends on the bond angle (Fig. 2.5). Close to 90 °, there is a crossover to dominant ferromagnetic exchange [13-15].

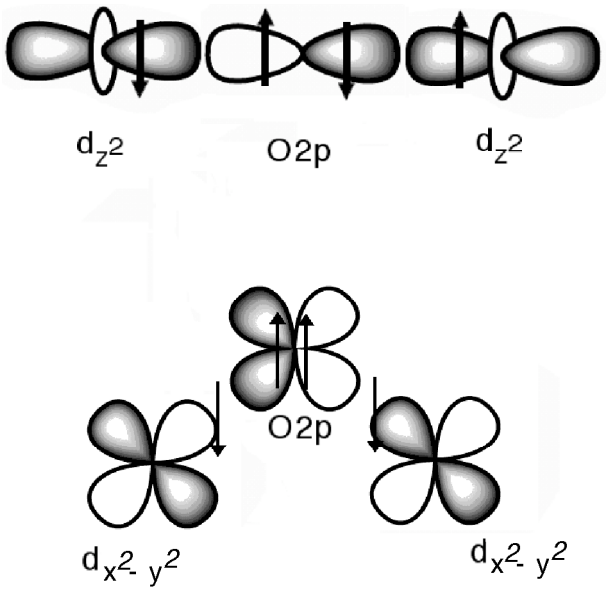

Figure 2.5: Correlation 180 ° superexchange pathway stabilising antiferromagnetic ground state (top) and 90 ° polarisation superexchange stabilising ferromagnetic groundstate (bottom).

The magnetic susceptibility of materials with an imbalance of exchange interactions is best fitted by a modified Curie law, the Curie-Weiss law:

$$\chi = \frac{C}{T - \Theta} \tag{2.12}$$

where θ is the Weiss constant and is directly related to the strength of the exchange interactions by [16]:

$$\theta = -S_i S_j \sum \frac{2J_{ij}}{3k_B} \tag{2.13}$$

The strength of superexchange is strongly influenced by the degree of covalency, indeed in the first row transition metal rock salt oxides, T_N increases from 122 K for MnO to 520 K for NiO [17].

2.2.4. Magnetic anisotropy

Anisotropy plays a key role in determining the properties of magnetic materials, several of the most important sources are detailed below. The first, spin anisotropy, is principally caused by spin orbit coupling. Rewriting the Heisenberg exchange Hamiltonian as:

$$H = -2J \sum [a(S_{ix}.S_{jx} + S_{iy}.S_{jy}) + bS_{iz}.S_{jz}] \tag{2.14}$$

allows the definition of three classes of spins. If **a** = 0 and **b** = 1, the Ising model is obtained and the spins are constrained to lie along one axis. If **a** = 1 and **b** = 0, the XY model results and the spins are constrained to lie in a plane. Finally, for unconstrained Heisenberg spins, **a** = **b** = 1 [18].

Reduced structural dimensionality, that is anisotropy of exchange interactions, also has a large influence on magnetic properties. Firstly, as the dimensionality of a system decreases, the ordering temperature is reduced, falling to 0 K for a perfect one dimensional chain. In practice, small interchain interactions always cause a transition to long range order at a finite temperature. Secondly, the ordered moment in low dimensional magnetic systems is often strongly reduced due to the low lying excited states (spin waves). The amount of spin reduction depends on the number of nearest neighbours, spin value and spin dimensionality and is maximum for an **S** = 1/2 Heisenberg chain. The experimental signatures of reduced magnetic dimensionality are a broad maximum in the magnetic

susceptibility well above the ordering temperature and strongly reduced magnetic entropy at the ordering temperature.

Orbital order can also produce low dimensional magnetic behaviour, even in Heisenberg systems with isotropic structures. The perovskite $KCuF_3$ is a classic example. The octahedrally coordinated Cu^{2+} cation is subject to a strong Jahn-Teller distortion, with the unpaired e_g electron residing in the d_{x2-y2} orbital. The elongation of the CuF_6 octahedra alternates along $\boldsymbol{a}$ and $\boldsymbol{b}$, forming a one dimensional chain of stronger superexchange interactions along $\boldsymbol{c}$. The magnetic susceptibility of $KCuF_3$ can be well modelled as an $\mathbf{S} = 1/2$ Heisenberg chain [19]. Orbital order in the pyrochlore material $Tl_2Ru_2O_7$ also produces chains of magnetically coupled cations in a three dimensional structural framework [20].

2.2.5. Frustration

The ground state of a system, magnetic or otherwise, can be destabilised if it is impossible to satisfy simultaneously all nearest neighbour interactions [21]. A trivial and oft-quoted example is that of Ising spins in a triangular arrangement with antiferromagnetic exchange. As shown in Fig. 2.6, only two moments can have definite orientations, the third is undetermined. The ground state of this system also has a large degeneracy, six distinct arrangements of the three spins are possible.

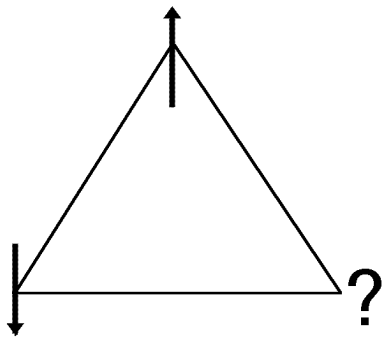

Figure 2.6: Frustrated Ising spins on a triangular lattice.

Geometric frustration in magnetic systems strongly depresses the ordering temperature with respect to the Weiss temperature. Especially when combined with low dimensionality and

small moments, frustration can induce a range of unusual magnetic ground states. Geometrically frustrated magnetic materials have been recently reviewed [22].

2.2.6. Techniques for measuring magnetic properties

A Quantum Design Magnetic Property Measurement System (MPMS) was used to measure the magnetic susceptibility as a function of temperature. The MPMS has a temperature range $1.8 < T < 320$ K and fields of up to 1 T can be applied with the aid of a superconducting magnet. The MPMS uses a superconducting detection coil connected to a Superconducting Quantum Interference Device (SQUID) to measure the change in sample magnetic moment. The sample is placed in a gelatine capsule, inserted in a drinking straw then suspended in the centre of the detection coil. The moment of the sample causes a change in the permanent current in the detection coil, it is this change that the SQUID measures. The SQUID relies on a pair of Josephson junctions (Fig. 2.7). If a constant current through the device is maintained, the measured voltage will oscillate with the phase changes at the two junctions. The phase changes are directly related to the magnetic flux that passes through the junction [23,24]. Magnetic moments and Weiss constants for all sample were obtained by least squares fitting the inverse susceptibilities to a typical accuracy of $\pm$ 0.05 μ_B and 0.1 K respectively.

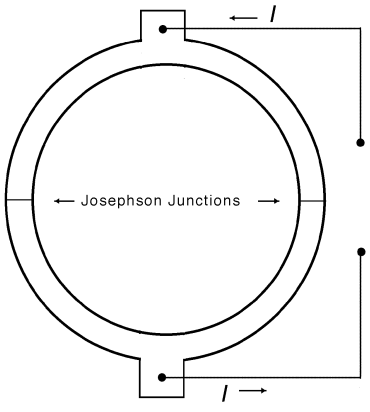

Figure 2.7: Schematic of Superconducting Quantum Interference Device (SQUID).

A Quantum Design Physical Property Measurement System (PPMS) was also used to measure several of the materials studied in this work. The AC susceptibility insert was used to measure M(H) isotherms at fixed temperatures, the heat capacities of several samples were also measured. Heat capacity measurements are a sensitive probe of magnetic materials as ordering transitions are second order and thus expected to give large anomalies in the heat capacity at constant volume, C_v, defined below:

$$C_v = \left(\frac{\partial U}{\partial T}\right)_V \tag{2.15}$$

For a non-magnetic insulator, it is assumed that the only contribution to U is from thermally excited phonons. If we further make the assumption[1] that the heat capacity at constant volume, C_v, is equal to the heat capacity at constant pressure, C_p, then at high temperature the heat capacity tends to the Dulong-Petit limit:

$$C_v = 3Nk_B = 3R \tag{2.16}$$

The Debye heat capacity shown in Eqn. 2.17 is a reasonable approximation to the heat capacity of real materials. At high temperature it tends toward the Dulong-Petit limit, at low T when the integral in Eqn. 2.17 is effectively constant the heat capacity is $\propto T^3$ [1].

$$C_v = 9Nk_B\left(\frac{T}{\theta_D}\right)^3 \int_0^{x_D} \frac{x^4 e^x dx}{(e^x - 1)^2}, x = \theta_D / T \tag{2.17}$$

Here Θ_D is the Debye temperature, the temperature of the highest energy normal mode. The Debye heat capacity is sometimes found to give unrealistic results for low dimensional materials and other approximations have been proposed [25].

[1] Equivalent to zero thermal expansion.

2.3. Symmetry in the Solid State

2.3.1. Point group symmetry

The symmetry of isolated objects, for example the ferrocene molecule shown in Fig. 2.8 can be described by point groups, which are collections of symmetry elements.

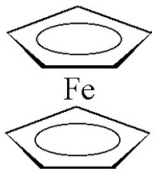

Figure 2.8: Structure of ferrocene in eclipsed conformation.

The point group for ferrocene in the eclipsed conformation is D_{5h} and contains the symmetry elements shown in Table I.

Table I: Symmetry elements of ferrocene molecule.

Symmetry element	Description
C_5	Five-fold rotation axis
5 x C_2	Two-fold rotation axis
σ_h	mirror plane
5 x σ_v	mirror planes
I	impoper rotation

2.3.2. The crystal lattice

Repeating arrangement of objects (lattice points) can be described by a crystal lattice. If the origin of the lattice is chosen to lie on one of the lattice points, then the positions of all lattice points may be specified by the set of lattice vectors **r**, where u, v, w are integers and $\boldsymbol{a}$, $\boldsymbol{b}$, $\boldsymbol{c}$ are the vectors connecting nearest neighbour lattice points:

$$r = ua + vb + wc \tag{2.18}$$

It can easily be verified, that regular polyhedra with five of seven fold symmetry cannot be packed into a continuous lattice. Therefore, in contrast to isolated objects like ferrocene, only 1-, 2-, 3-, 4- and 6-fold rotation axis can be found in crystalline lattices of up to three dimensions. It is conventional at this point to define the seven crystal classes by the relationships between their lattice vectors. However, these relationships are merely constraints imposed by the symmetry elements of each class. This is an important distinction as real systems may, for example, have orthorhombic symmetry but a metrically tetragonal cell. The relevant combinations of symmetry elements and the resulting constraints on the lattice parameters are shown in Table II. Also shown are the fourteen Bravais lattices generated by combining the seven crystal classes with the lattice centring operations.

Table II: The seven crystal classes and required symmetry elements.

Crystal class	Required symmetry	Lattice parameters	Bravais Lattices
Cubic	4 x 3-fold rotation axis	$a = b = c,\ \alpha = \beta = \gamma = 90\ °$	P, I, F
Tetragonal	1 x 4-fold rotation axis	$a = b \neq c,\ \alpha = \beta = \gamma = 90\ °$	P, I
Orthorhombic	3 x 2-fold rotation axis and/or mirrors	$a \neq b \neq c,\ \alpha = \beta = \gamma = 90\ °$	P, C, I, F
Monoclinic	1 x 2-fold rotation axis and/or mirror	$a \neq b \neq c,\ \alpha = \gamma = 90\ °,\ \beta \neq 90\ °$	P, C
Hexagonal	1 x 6-fold rotation axis	$a = b \neq c,\ \alpha = \beta = 90\ °,\ \gamma = 120\ °$	P
Rhombohedral	1 x 3-fold rotation axis	$a = b = c,\ \alpha = \beta = \gamma \neq 90\ °$	P
Triclinic	-	$a \neq b \neq c,\ \alpha \neq \beta \neq \gamma \neq 90\ °$	P

The crystal structure of a material may be generated by combining the Bravais lattice with the *basis* (the repeating group of atoms at each lattice point). The combination of the 32 point groups that are compatible with crystalline order and the Bravais lattices produces the 230 space groups. These are listed in the International Tables for Crystallography and describe all structures possible in three dimensions [26].

With the addition of an antisymmetry operation, i, many ordered magnetic structures may also be described using the same framework. Any symmetry element, g may be combined with i to give the new operation g'. The new operation has the same properties as g with the addition of a spin flip. It should also be noted that as a magnetic moment is an axial vector, symmetry operations act on the 'current loop', the direction of the moment is given by the right hand screw rule. The effect of an unprimed and primed mirror plane on a magnetic moment is shown in Fig. 2.9.

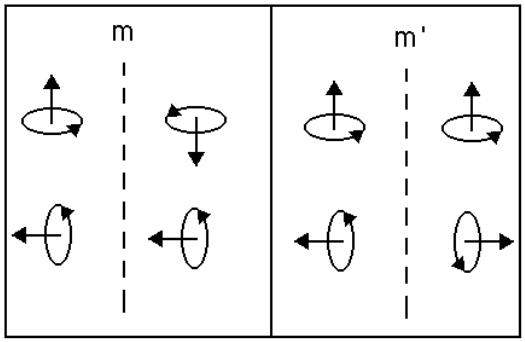

Figure 2.9: Effect of unprimed and primed mirror plane operations on magnetic moment.

The addition of the antisymmetry operation leads to 122 magnetic point groups and 1421 magnetic (Shubnikov) space groups [27]. An alternative approach, representational analysis, is also of considerable application, especially in the case of incommensurate magnetic structures [28].

2.3.3. The reciprocal lattice

In order to simplify crystallographic calculations, the reciprocal lattice is often employed. The reciprocal lattice is related to the real space lattice by:

$$\begin{aligned} a.a^* &= 1 \quad a.b^* = 0 \quad a.c^* = 0 \\ b.a^* &= 0 \quad b.b^* = 1 \quad b.c^* = 0 \\ c.a^* &= 0 \quad c.b^* = 0 \quad c.c^* = 1 \end{aligned} \tag{2.19}$$

The reciprocal lattice points can be generated from the primitive reciprocal lattice vectors in a similar fashion to the real space lattice,where h, k and l are integers:

$$G_{hkl} = ha^* + kb^* + lc^* \tag{2.20}$$

Reciprocal lattice vectors have units of inverse length and can also be defined as:

$$G_{hkl} = \hat{n}_{hkl} / d_{hkl} \tag{2.21}$$

where $\boldsymbol{d}_{\mathrm{hkl}}$ is the distance between neighbouring planes in the real lattice.

2.4. Diffraction

When radiation with a wavevector $\mathbf{k}_i$ (= $2\pi/\lambda$) is incident on an ordered array of scatterers, diffraction effects are observed when the Bragg relation is satisfied. A two dimensional picture of a reciprocal lattice is shown in Fig. 2.10.

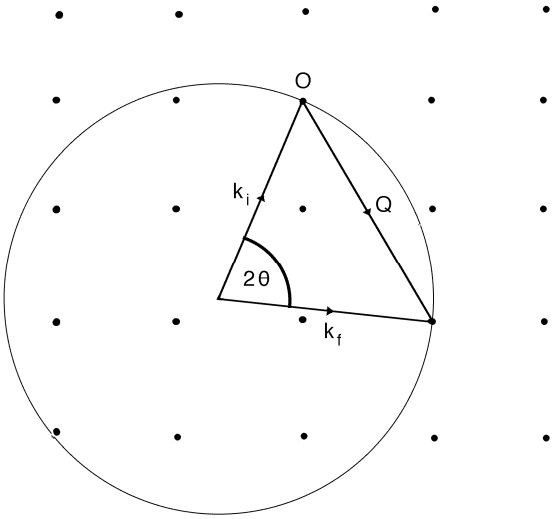

Figure 2.10: Schematic representation of Bragg scattering from two dimensional reciprocal lattice.

A circle with radius $\mathbf{k}_1$ (i.e. $\propto 1/\lambda$) is shown intersecting the origin, the condition for Bragg scattering is satisfied when the circle also intersects a reciprocal lattice point (i.e. **Q** = **G** is a reciprocal lattice vector). The condition for diffraction is therefore:

$$|Q| = 2|k_i|\sin\Theta \tag{2.22}$$

Or, as $\mathbf{Q} = 2\pi/d$ and $\mathbf{k}_i = 2\pi/\lambda$:

$$\lambda = 2d\sin\Theta \tag{2.23}$$

The intensity of a diffracted beam is related to the contents of the unit cell by the structure factor, $\mathbf{F}_{hkl}$:

$$F_{hkl} = \sum_j f_j \exp\left[2\pi i(hx_j + ky_j + ly_j)\right]\exp\left[-M_j\right] \tag{2.24}$$

The summation is over all atoms in the unit cell with coordinates x, y and z. The form factor, f_j, is the Fourier transform of the scattering density in real space. In the case of X-ray

diffraction, a marked fall off with scattering angle is observed. As the atomic nucleus is effectively point like when compared with the wavelength of thermal neutrons, the form factor for neutron diffraction is nearly independent of scattering angle. The effect of thermal motion (and positional disorder) is accounted for by the displacement factor exp[-$\mathbf{M}_j$]:

$$M_j = 8\pi^2 u_s^2 \sin^2\Theta/\lambda^2 \tag{2.25}$$

For magnetic neutron diffraction, the structure factor is modified by the inclusion of an X-ray like fom factor and the vector $\boldsymbol{M}_{hkl}$, which is determined by the relative orientation of the magnetic moment (**m**) and the unit vector normal to the scattering plane (**e**) (Fig. 2.11).

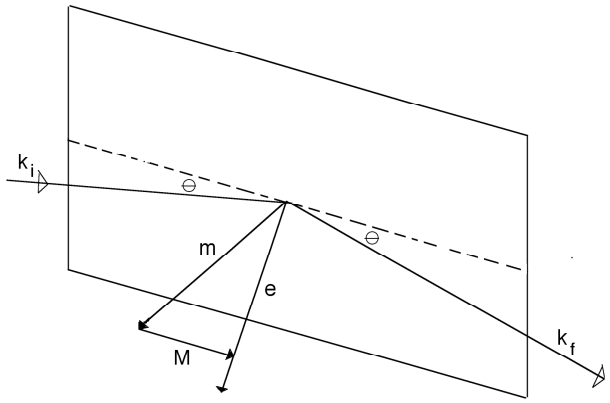

Figure 2.11: Vector relationship for magnetic diffraction.

For magnetic diffraction to occur, the magnetic moment must have some component parallel to the scattering plane [29]. In the case of collinear magnetic structures, $\mathbf{F}_{hkl}$ is as given below, the relative orientations of the magnetic moments are taken in to account by the sign of the magnetic form factor, $\mathbf{f}_m$.

$$F_{hkl} = M_{hkl} \sum_j \pm f_m \exp[2\pi i(hx_j + ky_j + ly_j) \tag{2.25}$$

As the magnetic orbitals are extended in space, the magnetic form factor $\mathbf{f}_m$ falls off rapidly with scattering angle. For unpolarised neutrons, the magnetic and nuclear structure factors have no phase relation and are additive, i.e.:

$$F_{hkl}^2 = F_{Mag}^2 + F_{Nuc}^2 \tag{2.26}$$

2.4.1. Rietveld refinement

In a single crystal diffraction experiment, the detector is scanned over a given reflection and the integrated intensity, I, is as given below.

$$I = A\frac{\lambda^3 |F_{hkl}|^2}{v_0^2 \sin 2\Theta} \tag{2.27}$$

Here A is a scale factor, related to the incident flux, illuminated volume and counting time etc. Only the modulus of $\mathbf{F}_N(hkl)$ is measured, which has serious consequences for structural determination. If a sufficient set of structure factors is available, as is typically found in a single crystal diffraction experiment, the structure of a material may be refined directly by least squares methods. In a powder diffraction experiment, the complete set of Bragg reflections is compressed into a simple plot of intensity versus scattering angle (or time of flight, energy etc). this leads to strong overlap between reflections. Furthermore, the diffraction profile also contains a background contribution from sample and instrument and is convoluted with the instrument profile. In all but the simplest systems, it is clearly impractical to refine the structure based on measurements of individual structure factors. Rietveld refinement is an elegant solution [30,31]. The diffraction profile is subdivided into a (large) number of steps and the intensity at each step compared with a model that includes the crystal structure, instrument constants and microstructural details. By a process of least squares, the model variables are refined against the *entire pattern* until the residual, $\mathbf{S}_y$, is minimised.

$$S_y = \sum_i w_i (y_i - y_c)^2 \tag{2.28}$$

where w_i is a weighting factor (usually $1/y_i$), y_i is the observed intensity at the *i*th step and y_c is the calculated intensity at the *i*th step. The calculated intensity is a function of the structure factors that contribute intensity over a given step and various instrumental contributions [32].

$$y_c = s\sum_K L_K |F_K|^2 \Phi(2\Theta_i - 2\Theta_K) A + y_{bi} \tag{2.29}$$

Here, **s** is the scale factor, $\mathbf{L}_K$ contains the Lorentz and polarisation terms and also the multiplicity factor, Φ is the profile function, **A** is the absorption factor and $\mathbf{y}_{bi}$ is the calculated background intensity.

The quality of a Rietveld fit is best judged by a plot of the observed, calculated and difference profiles. Nevertheless, several statistical fitting parameters are often quoted and are shown in Table III.

Table III: Statistical fitting parameters for Rietveld refinement.

$R_{wp} = \left\{ \frac{\sum_i w_i [y_i - y_c]^2}{\sum_i w_i [y_i]^2} \right\}^{1/2}$	R-weighted profile
$R_p = \frac{\sum \lvert y_i - y_c \rvert}{\sum y_i}$	R-pattern
$R_E = \left\{ \frac{(N-P)}{\sum w_i y_i^2} \right\}^{1/2}$	R-expected
$\chi^2 = \frac{{}_w R_p^2}{R_E^2}$	Chi-squared

The R-weighted profile factor is often regarded as the most significant as it contains the residual, $\mathbf{S}_y$. The R-expected factor is a measure of how good a value of R-weighted profile can be expected, based on the number of independent data points. It can be shown that $R_E \approx 1/\sqrt{(<y_i>)}$ and it is therefore highly dependent on the background in a diffraction pattern, with a high background giving an artificially small value [33]. The ratio of these two factors squared (χ^2) can be used as a measure of the progress of a fit.

2.4.2. Diffraction facilities

X-ray and neutron powder diffraction experiments were performed at three large scale central facilities. Table IV shows a summary of the various instruments used.

Table IV: Instruments used at central facilities.

Facility	Instrument	Purpose
ISIS, pulsed neutron source, Oxfordshire	OSIRIS	High resolution cold neutron diffractometer [34]
Institute Laue Langevin (ILL), continuous (reactor) neutron source, Grenoble	Super-D2B	High resolution diffractometer [35.36]
	D20	High flux diffractometer [37]
	D1B	High flux diffractometer
European Synchrotron Radiation Source (ESRF),synchrotron X-ray source, Grenoble	ID31	Very high resolution diffractometer [38]

The time of flight instrument OSIRIS views the cold (hydrogen) neutron moderator at ISIS and is hence optimised for long d-space diffraction, especially complex magnetic structures. The continous wavelength diffractometers, Super-D2B, D20 and D1B all view the thermal source at the ILL reactor and operate in Debye-Scherrer geometry. Super-D2B features a high monochromator takeoff angle (120 °) and post sample collimation leading to high resolution. The medium resolution instrument D20 is situated very near to the reactor face and hence enjoys perhaps the highest neutron flux of any such instrument worldwide. A very large (160 °) position sensitive detector means that experiments can be performed parametrically. D1B is a precursor to D20, with lower flux and an older, position sensitive detector which only covers 120 °, situated in the guide hall. The synchrotron X-ray instrument ID31 enjoys unparalled resolution and flux as it is situated at an insertion device at the ESRF. The detector is preceded by a bank of silicon analyser crystals which further increase the resolution. In addition, a Bruker D-8 Advance sealed tube diffractometer was used for checking phase purity and for preliminary structural investigations. Powder diffraction profiles were fitted using the GSAS suite of software [39,40].

References

[1] S. Elliot, *The Physics and Chemistry of Solids*, John Wiley & Sons (1998)

[2] C.N.R. Rao, *Pure & Appl. Chem.*, **66**, 1765 (1994)

[3] O. Varnier, N. Hovnanian, A. Larbot, P. Bergez, L. Cot, J. Charpin, *Mat. Res. Bull.*, **29**, 479 (1994)

[4] J.V. Badding, *Ann. Rev. Mater. Sci.*, **28**, 631 (1998)

[5] S.E. Dann, M.T. Weller, D.B. Currie, *J. Solid State Chem.*, **92**, 237 (1991)

[6] B.L. Chamberland, *Solid State Comm.*, **8**, 663 (1967)

[7] H. Huppertz, *Z. Kristallogr*, **219**, 330 (2004)

[8] P.A. Cox, *The Electronic Structure and Chemistry of Solids*, Oxford University Press, Oxford (1987)

[9] L.J. van der Pauw, *Philips Res. Repts.*, **13**, 1 (1958)

[10] R.L. Carlin, A.J. van Duyneveldt, *Magnetic Properties of Transition Metal Compounds*, Springer-Verlag, New York (1977)

[11] H.A. Jahn, E. Teller, *Proc. Roy. Soc. Lond.*, **161**, 220 (1937)

[12] J.B. Goodenough, *Phys. Rev.*, **117**, 1442 (1960)

[13] P.W. Anderson, *Phys. Rev.*, **79**, 350 (1950)

[14] P.W. Anderson, *Phys. Rev.*, **115**, 2 (1959)

[15] J. Kanamori, *J. Phys. Chem. Solids*, **10**, 87 (1959)

[16] R.L. Carlin, *Magnetochemistry*, Springer, New York (1986)

[17] J.B. Goodenough, *Magnetism and The Chemical Bond,* Interscience, New York (1963)

[18] *Magnetic Properties of Layered Transition Metal Compounds,* ed. L.J. de Jongh, Kluwer Academic, Dordrecht (1989)

[19] A.I. Liechtenstein, V.I. Anisimov, J. Zaanen, *Phys. Rev. B*, **52**, 5467 (1995)

[20] S. Lee, J.-G. Park, D.T. Adroja, D. Khomskii, S. Streltsov, K.A. McEwen, H. Sakai, K. Yoshimura, V.I. Anisimov, D. Mori ,R. Kanno, R. Ibberson, *Nature Material*, **5**, 471 (2006)

[21] A.P. Ramirez, in *Handbook of Magnetic Materials* (ed. Buschow, K.J.H.) 423-520 New Holland, New York (2001)

[22] J.E. Greedan, *J. Mat. Chem.*, **11**, 37 (2001)

[23] B.D. Josephson, *Physics Letters*, **1**, 251 (1962)

[24] B.D. Josephson, *Advances in Physics*, **14**, 419 (1965)

[25] K. Kopinga, R. van der Leeden, W.J.M. de Jonge, *Phys. Rev. B*, **14**, 1519 (1976)

[26] *International Tables for Crystallography, Volume A: Space group Symmetry*, Springer (2005)

[27] A.V. Shubnikov, *Symmetry and Antisymmetry of Asymetrical Finite Figures [Russian]*, Izd. Akad. Nauk SSSR (1951)

[28] E.F. Bertaut, *Acta Cryst. A*, **24**, 217 (1968)

[29] Y.A. Izyumov, R.P. Ozerov, *Magnetic Neutron Diffraction*, Plenum Press, New York (1970)

[30] H.M. Rietveld, *J. Appl. Cryst.*, **2**, 65 (1969)

[31] H.M. Rietveld, *Acta Cryst.*, **22**, 151 (1967)

[32] R.A. Young (ed), *The Rietveld Method*, Oxfor University Press, Oxford (1995)

[33] W.I.F. David, *J. Res. Nat. Inst. Stand. Tech.*, **109**, 107 (2004)

[34] D.M.Y. Marero, D. Engberg, K.H. Andersen, *Physica B*, **276**, 150 (2000)

[35] A.W. Hewat, S. Heathman, *Acta. Cryst. A*, **40**, 364 (1984)

[36] A.W. Hewat, *Physica B*, **385-86**, 979 (2006)

[37] T.C. Hansen, P. Convert, *Mat. Sci. Forum*, **378**, 294 (2001)

[38] A.N. Fitch, *Mat. Sci. Forum*, **228**, 219 (1996)

[39] A.C. Larson, R.B. Von Dreele, Los Alamos National Laboratory Report No. LAUR 86-748 (1994)

[40] B.H. Toby, EXPGUI, a graphical user interface for GSAS, *J. Appl. Cryst.*, ***34***, 210-213 (2001)

Chapter 3

Structure and Magnetic Properties of the Zig-Zag Chain Material In_2VO_5

3.1. Introduction

The properties of low dimensional quantum magnets have been studied extensively, in particular the one-dimensional antiferromagnetic (AF) **S** = 1/2 chain, for which the susceptibility has been calculated to very high accuracy [1]. The addition of a next nearest neighbour, frustrating, AF exchange interaction (J_2) produces an array of exotic instabilities and ground states; this model is realised by the zig-zag chain shown in Fig. 3.1.

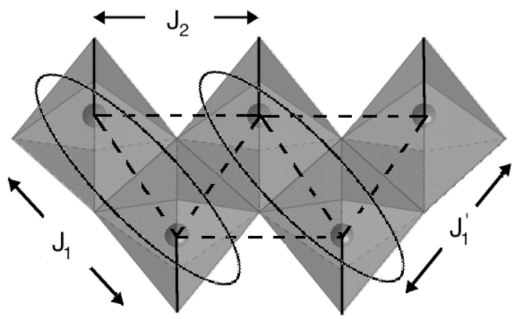

Figure 3.1: Zig-zag chain arrangement of VO_6 octahedra in In_2VO_5 showing the magnetic exchange interactions and the triplet dimers formed below 120 K. The short V-O bonds perpendicular to the chain direction are shown as solid lines.

The much studied case with J_1, $J_2 > 0$ (AF–AF) is unstable with respect to a singlet dimerised state with a spin gap when the ratio $\alpha = J_2/J_1 > 0.2411$ [2,3], as exemplified by the

spin-Peierls material $CuGeO_3$ [4]. The zig-zag chain with ferromagnetic J_1 and antiferromagnetic J_2 (F–AF) coupling has been less studied, however recent work has shed new light on the phase diagram and thermodynamics of this model. The ground state is reported to be ferromagnetic for $0 \leq \alpha \leq 1/4$ and an antiferromagnetic helix for $\alpha > 1/4$ [5-7], which has been realised in several materials containing $\mathbf{S} = 1/2$ Cu^{2+} [8-10]. Oxides containing V^{4+} are another source of quantum magnets and have been less studied than their cuprate counterparts. This chapter reports magnetic susceptibility, heat capacity and synchrotron powder X-ray diffraction measurements on a previously uncharacterised vanadate, In_2VO_5. This material crystallises in the orthorhombic space group *Pnma* with a structure consisting of isolated $\mathbf{S} = 1/2$ zig-zag chains of V^{4+} which run along $\boldsymbol{b}$, separated by sheets of edge sharing InO_6 octahedra (Fig. 3.2). Because there is only one equivalent V^{4+} site, the structure maps exactly onto the widely studied zig-zag chain models.

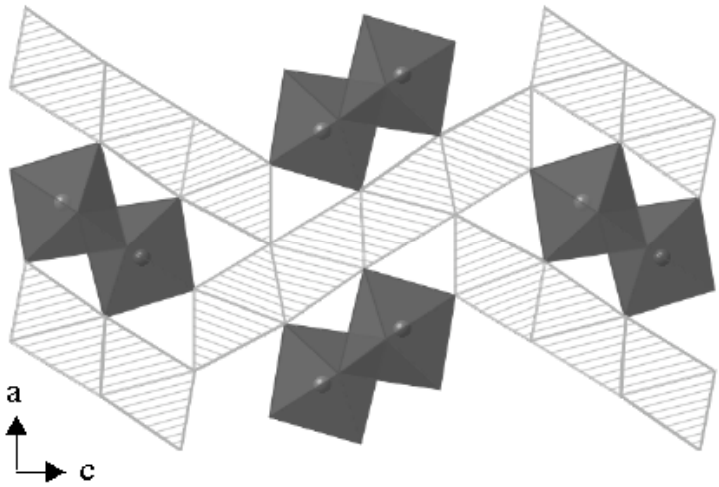

Figure 3.2: Structure of In_2VO_5 projected down [010]. Dark octahedra are VO_6, light octahedra are InO_6.

Our results reveal a novel, spin dimerisation instability in an F-AF S = 1/2 zig-zag chain. Below 120 K, In_2VO_5 behaves as an unfrustrated chain of antiferromagnetically coupled S =1 triplet dimers which show a further condensation into a global singlet ground state at 2.5 K Two recent theoretical papers have investigated magnetic exchange in In_2VO_5 and have reported contradictory results of frustrated antiferromagnetic [11] or ferromagnetic

exchange interactions [12]. After submission of this work for publication, two competing groups also made preprints available online [13,14].

3.2. Experimental

A high purity sample of In_2VO_5 was prepared by grinding small single crystals, grown by the previously reported method [15]. Stoichiometric quantities of VO_2 and In_2O_3 were sealed in a silica ampoule and heated slowly to 1000 °C. After three hours the temperature was raised to 1200 °C and maintained for 36 hours. The product was slow cooled over 24 hours and consisted of very small single crystals. Magnetic susceptibility measurements were performed using a Quantum Design SQUID magnetometer in zero and field (150 Oe) cooled conditions. A Quantum Design PPMS instrument with a ^{3}He insert was used for heat capacity measurements. High resolution synchrotron X-ray diffraction patterns with λ = 0.45621 Å were collected as a function of temperature using instrument ID31 at the ESRF. High resolution neutron powder diffraction data were recorded at 10 K using Super-D2B at the ILL and high flux neutron powder diffraction data were recorded using D20 at the ILL at a range of temperatures.

3.3. Magnetisation and Heat Capacity Measurements

The magnetic susceptibilities of In_2VO_5 are shown in Fig. 3.3. Two distinct linear regions are seen in the inverse susceptibility with a crossover at 120 K. A Curie-Weiss fit in the range 140 – 300 K, gives a Weiss temperature of Θ = 17(1) K, and a moment of 1.8(1) μ_B, consistent with an S = 1/2 system with g = 2.09. Below 120 K, the Weiss temperature changes sign (Θ = -70(1) K) and the paramagnetic moment increases to 2.2(1) μ_B. A broad maximum in both the field and zero field cooled susceptibilities is seen at 2.5 K (inset Fig. 3.3).

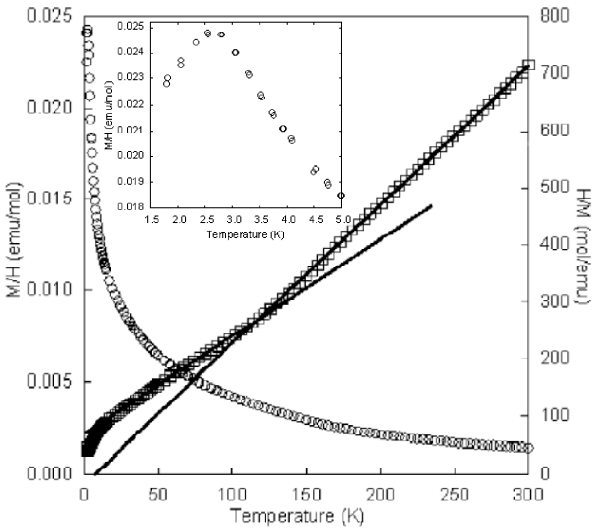

Figure 3.3: Magnetic susceptibility of In_2VO_5 measured in a 150 Oe field, and the inverse susceptibility with Curie-Weiss shown in the ranges 30 - 100 K and 150 – 300 K and extrapolated to low temperatures. The inset shows the low temperature susceptibility maximum.

A crossover between positive and negative Θ regimes is very unusual, and could signify a transition at which the structure and hence the exchange pathways are significantly altered, but this is ruled out by the diffraction results below.

Similar results are reported in the work of Singh *et al* [14] who measured the magnetic susceptibility of In_2VO_5 in a 100 Oe field. However, they report a large divergence between field and zero field cooled measurements at 2.5 K and strongly frequency dependant ac-susceptibility measurements. Based on these results, they conclude that In_2VO_5 is a spin glass. As a conventional spin glass state requires both frustration and disorder, this result may be an indication of varying sample quality between groups.

The heat capacities (C_p) of In_2VO_5 and the diamagnetic analogue In_2TiO_5 were measured at 0.42 – 200 K using a Quantum Design PPMS system and are plotted in Fig 3.4. The magnetic heat capacity of In_2VO_5 was estimated by subtracting the In_2TiO_5 data and the resulting $C_p(mag)/T$ and magnetic entropy, S_{mag}, are shown in Fig. 3.5.

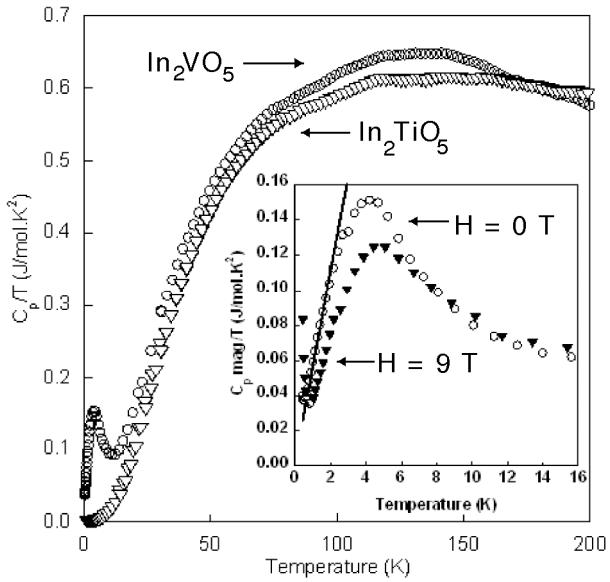

Figure 3.4: Heat capacities of In_2VO_5 and In_2TiO_5 plotted as C_p/T against temperature. The inset shows magnetic part of the heat capacity of In_2VO_5 measured in zero and 9 T fields with a power law fit to the zero field data below 2 K.

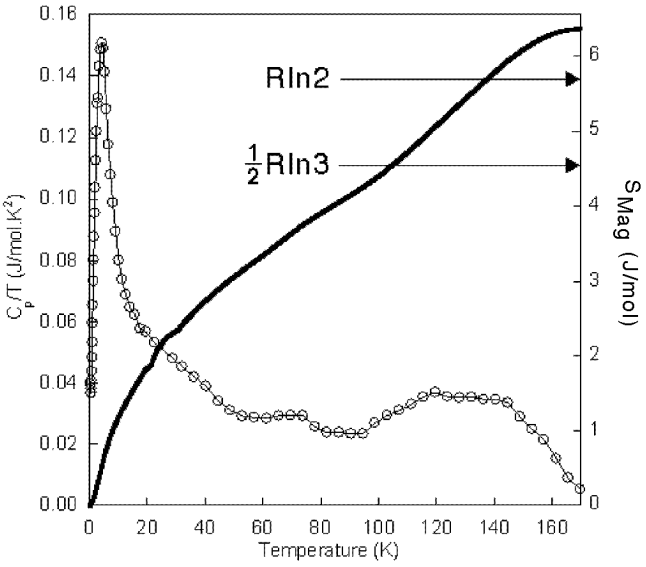

Figure 3.5: Magnetic heat capacity of In_2VO_5 (shown as C_p(mag)/T) and the integrated entropy versus temperature, showing the expected limits for triplet dimer (1/2Rln3) and S =1/2 monomer (Rln2) states.

A C_p/T peak is seen at 4 K for In_2VO_5 and a broad feature is also observed around 120 K The breadth of the 4 K peak and its robustness to a 9 T applied field (inset Fig. 3.4) shows that it does not signify a long range magnetic ordering transition. (For long range order, a field estimated as $k_B T_{peak}/g\mu_B \approx 4$ T would be sufficient to suppress the peak). Furthermore, the heat capacity shows a power law scaling, $C_p(mag) \sim T^{1.89(2)}$ below 2 K. Linear scaling is expected for a truly one-dimensional system, but similar values of 1.7-1.8 are reported in several quasi-1D systems (see footnote 21 in ref. 10). A small bump is seen in the magnetic heat capacity at ca. 2.5 K, which may correspond to the downturn in the magnetic susceptibility.

Singh *et al* also report similar heat capacity measurements [14]. However, the magnetic entropy that they calculate for In_2VO_5 is 10 J/mol, about 75 % higher than the theoretical value. They attribute the excess entropy to a possible structural phase transition at 120 K. Our extensive diffraction measurements rule out a phase change, and show only a subtle anomaly in the lattice parameters at 120 K.

3.4. Powder Diffraction Experiments

To determine whether In_2VO_5 undergoes a structural transition at 120 K, synchrotron powder X-ray diffraction data were collected in the range 10 – 280 K at 30 K steps. The data were fitted well by the previously reported *Pnma* structure, using the GSAS suite of programs [15,16], and no gross structural transition (e.g. V-V dimerisation) or superstructure was seen down to 10 K. However, the lattice parameters (Figs 3.6- 9) show a small anomaly at 120 K, with a minimum in the ***b*** (chain) axis length and subtle discontinuity in the ***a*** and ***c*** axis. This evidences a coupling of the local spin correlations to the lattice. However, no significant change to the atomic coordinates, and hence to the bond angles that influence the exchange pathways, are observed around the 120 K crossover. The temperature evolution of the V atomic coordinates and the interchain V – V distance are shown in Figures 3.10 and 3.11[1].

[1] The intrachain V –V distance is the ***b*** axis

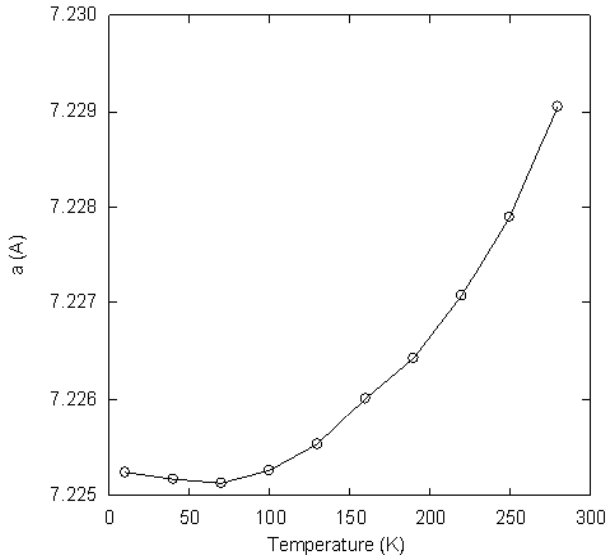

Figure 3.6: Temperature dependence of In_2VO_5 ***a*** axis from synchrotron powder X-ray diffraction. Error bars are smaller than symbols.

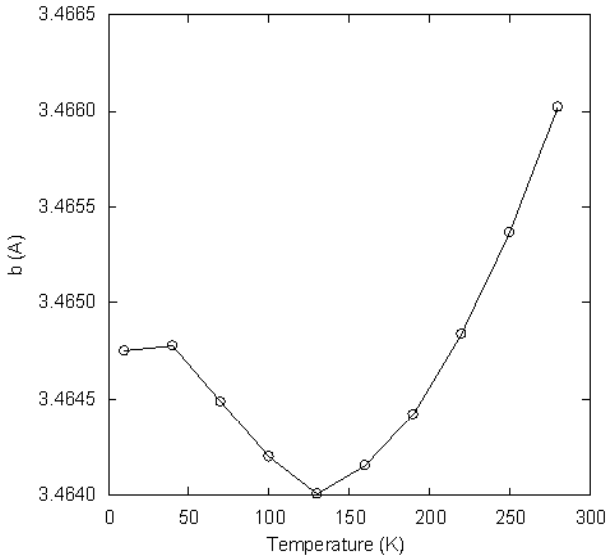

Figure 3.7: Temperature dependence of In_2VO_5 ***b*** axis from synchrotron powder X-ray diffraction. Error bars are smaller than symbols.

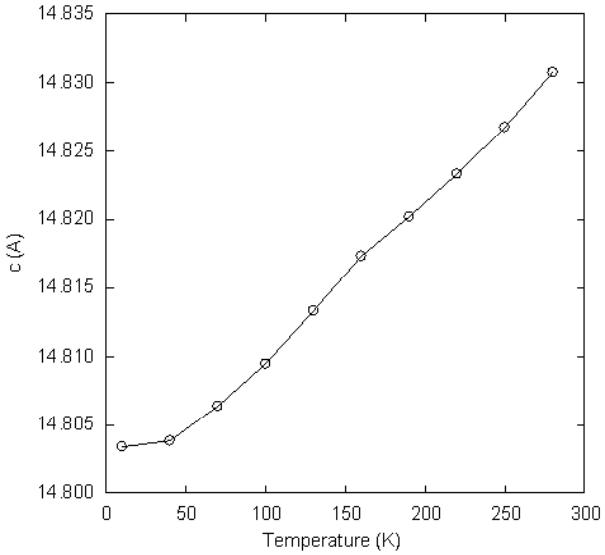

Figure 3.8: Temperature dependence of In_2VO_5 ***c*** axis from synchrotron powder X-ray diffraction. Error bars are smaller than symbols.

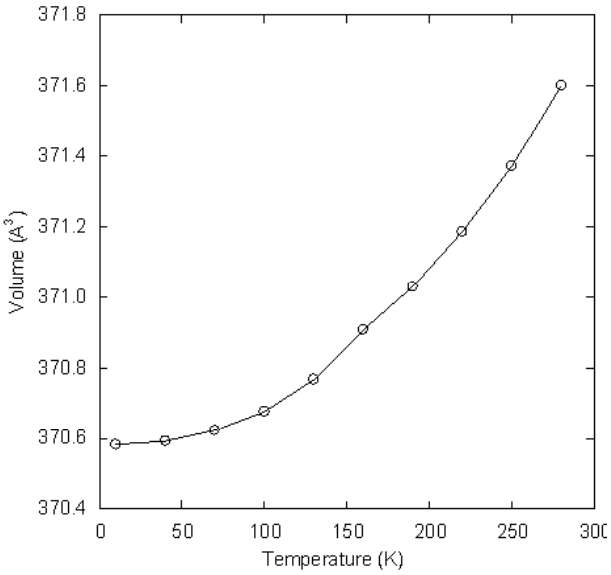

Figure 3.9: Temperature dependence of In_2VO_5 cell volume from synchrotron powder X-ray diffraction. Error bars are smaller than symbols.

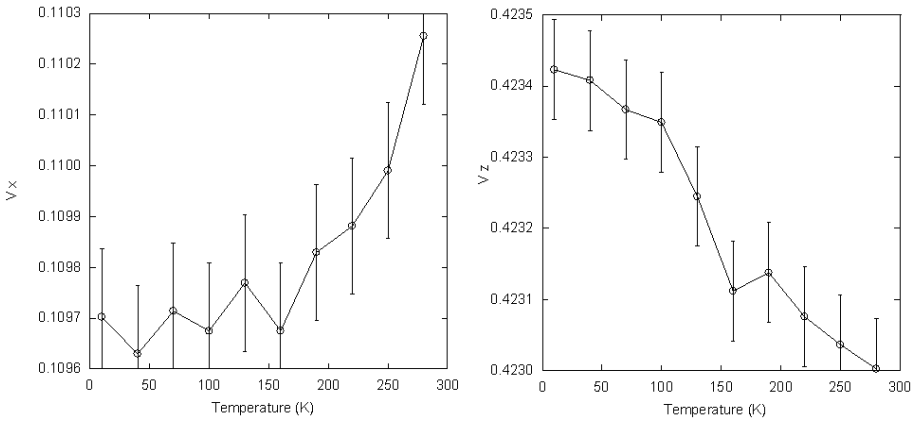

Figure 3.10: Temperature dependence of V atomic coordinates in In_2VO_5 refined from synchrotron powder X-ray diffraction.

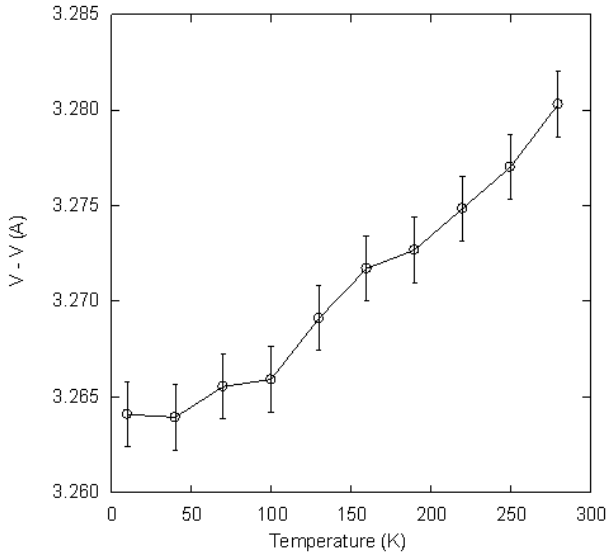

Figure 3.11: Temperature dependence of interchain V – V distance in In_2VO_5 refined from synchrotron powder X-ray diffraction.

The best fit to the synchrotron powder X-ray diffraction profiles was obtained when an anisotropic strain model was used. The lattice microstrain (root mean-squared variations in lattice strain) were found by fitting the full-widths at half maxima Γ_{hkl} of the Lorentzian X-

ray diffraction peaks as Γ_{hkl} (rad.) = $[s_{\perp}[010] + (s_{||}[010] - s_{\perp}[010])\cos\Phi + s_i]\tan\Theta$, , where$\Phi$ is the angle between [010] and the normal to the (hkl) diffraction plane. The instrumental broadening contribution, s_i = 0.036% was found by fitting peaks from a standard silicon powder. The lattice strain component parallel to *b*, $s_{||}[010]$, which quantifies local variations in the axis length, is larger than the perpendicular component and increases on cooling from 300 K but then decreases at low temperatures (Fig. 3.12). This is consistent with lattice strains originating in the VO_6 edge sharing chains.

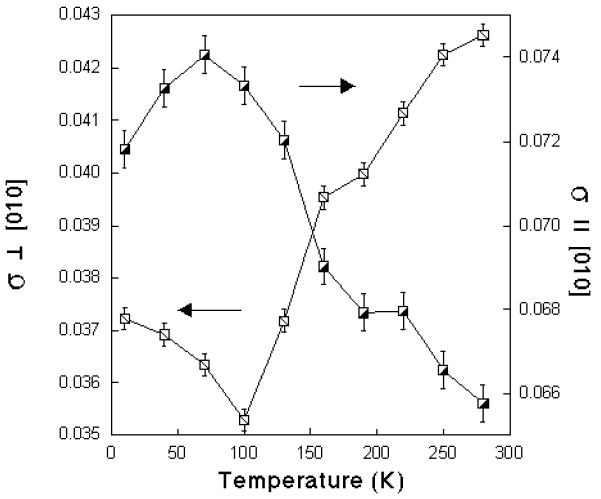

Figure 3.12: Temperature dependence of lattice microstrain in In_2VO_5 parallel and perpendicular to [010].

The results from Rietveld fits to all the synchrotron X-ray diffraction profiles are summarised in Tables I – III. Wyckoff positions are In1 (4*c*), In2 (4*c*), V1 (4*c*), O1 (4*c*), O2 (4*c*), O3 (4*c*), O4 (4*c*), O5 (4*c*).

Table 1: Indium atomic coordinates and displacement parameter for In_2VO_5 from Rietveld refinement of synchrotron powder X-ray diffraction data. In(1) site is (*x*, 1/4, *z*), In(2) site is (*x*, 3/4, *z*)

T (K)	In(1): *x*	In(1): *z*	In(2): *x*	In(2):*z*	In:Uiso (x10^2Å^2)
10	0.0979(1)	0.0839(3)	0.3299(1)	0.2376(3)	0.17(5)
40	0.0980(1)	0.0839(3)	0.3300(1)	0.2376(3)	0.20(5)
70	0.0980(1)	0.0839(3)	0.3302(1)	0.2376(3)	0.20(5)
100	0.0980(1)	0.0840(3)	0.3303(1)	0.2377(3)	0.26(5)
130	0.0981(1)	0.0839(3)	0.3304(1)	0.2379(3)	0.28(5)
160	0.0983(1)	0.0840(3)	0.3305(1)	0.2378(3)	0.34(5)
190	0.0983(1)	0.0840(3)	0.3306(1)	0.2379(3)	0.34(5)
220	0.0983(1)	0.0840(3)	0.3306(1)	0.2378(3)	0.42(5)
250	0.0982(1)	0.0840(3)	0.3309(1)	0.23780(3)	0.49(5)
280	0.0982(1)	0.0840(3)	0.3311(1)	0.2378(3)	0.55(5)

Table II: Vanadium atomic coordinates and displacement parameter for In_2VO_5 from Rietveld refinement of synchrotron powder X-ray diffraction data. V site is (*x*, 1/4, *z*)

T (K)	V: *x*	V: *z*	V:Uiso (x10^2 Å^2)
10	0.1097(1)	0.4234(1)	0.25(2)
40	0.1096(1)	0.4234(1)	0.27(2)
70	0.1097(1)	0.4234(1)	0.28(2)
100	0.1097(1)	0.4233(1)	0.34(2)
130	0.1098(1)	0.4232(1)	0.35(2)
160	0.1097(1)	0.4231(1)	0.41(2)
190	0.1098(1)	0.4231(1)	0.38(2)
220	0.1099(1)	0.4231(1)	0.47(2)
250	0.1099(1)	0.4230(1)	0.50(2)
280	0.1103(1)	0.4230(1)	0.54(2)

Table III: Oxygen atomic coordinates and displacement parameters for In_2VO_5 from Rietveld refinement of synchrotron powder X-ray diffraction data. O(1-3) site is (*x*, 1/4, *z*), O(4,5) site is (*x*, 3/4, *z*)

T (K)	O(1):*x*	O(1):*z*	O(2):*x*	O(2):*z*	O(3):*x*	O(3):*z*	O(4):*x*	O(4):*z*	O(5):*x*	O(5):*z*	O: Uiso (x10^{2}Å^2)
10	0.240(1)	0.3227(2)	0.346(4)	0.4961(2)	0.3695(4)	0.1506(2)	0.0609(4)	0.1769(2)	0.0682(4)	0.4516(2)	0.24(3)
40	0.241(1)	0.3229(2)	0.347(4)	0.4959(2)	0.368(4)	0.1502(2)	0.0611(4)	0.1769(2)	0.0675(4)	0.4514(2)	0.29(3)
70	0.242(1)	0.3227(2)	0.346(4)	0.4962(2)	0.3692(4)	0.1502(2)	0.0610(4)	0.1766(2)	0.0689(4)	0.4508(2)	0.29(3)
100	0.242(1)	0.3228(2)	0.347(4)	0.4961(2)	0.3698(4)	0.1502(2)	0.0615(4)	0.1768(2)	0.0683(4)	0.4513(2)	0.38(3)
130	0.242(1)	0.3226(2)	0.347(4)	0.4960(2)	0.3700(4)	0.1503(2)	0.0618(4)	0.1770(2)	0.0682(4)	0.4507(2)	0.43(3)
160	0.243(1)	0.3220(2)	0.346(4)	0.4966(2)	0.3703(4)	0.1504(2)	0.0617(4)	0.1766(2)	0.0694(4)	0.4510(2)	0.47(3)
190	0.242(1)	0.3223(2)	0.347(4)	0.4962(2)	0.3703(4)	0.1503(2)	0.0635(4)	0.1762(2)	0.0690(4)	0.4513(2)	0.42(3)
220	0.242(1)	0.3222(2)	0.346(4)	0.4963(2)	0.3701(4)	0.1502(2)	0.0624(4)	0.1768(2)	0.0689(4)	0.4512(2)	0.51(3)
250	0.242(1)	0.3222(2)	0.347(4)	0.4962(2)	0.3702(4)	0.1506(2)	0.0633(4)	0.1765(2)	0.0688(4)	0.4512(2)	0.53(3)
280	0.243(1)	0.3222(2)	0.347(4)	0.4964(2)	0.3710(4)	0.1506(2)	0.0633(4)	0.1768(2)	0.0695(4)	0.4514(2)	0.59(3)

As vanadium has a low scattering length for neutrons and oxygen displacements can be hard to identify in the presence of heavy atoms, a combined Rietveld refinement was perfomed using the Super-D2B and ID31 data at 10 K. The peak shapes were described by a pseudo-voigt function with a correction for axial divergence. Anisotropic strain along [010] was refined as above. Anisotropic displacement parameters were refined individually for all atoms. The zero point shift was refined separately for both histograms. No significant departure from the room temperature structure was found. The occupancies of all sites refined to within one standard deviation of full occupancy. The refinement converged with residuals R_{wp} = 0.1186, R_p = 0.0949, $R(F^2)$ = 0.0333 (X-rays) and R_{wp} = 0.0801, R_p = 0.0622, $R(F^2)$ = 0.0736 (neutrons). The powder totals were R_{wp} = 0.1170, R_p = 0.0947 and χ^2 = 11.04. The observed, calculated and difference profiles are shown in Fig. 3.13 and 3.14. The thermal displacement ellipsoids for the VO_6 edge sharing chains are shown in Fig 3.15. The refined atomic coordinates and selected bond distances and angles are shown in Tables IV and V.

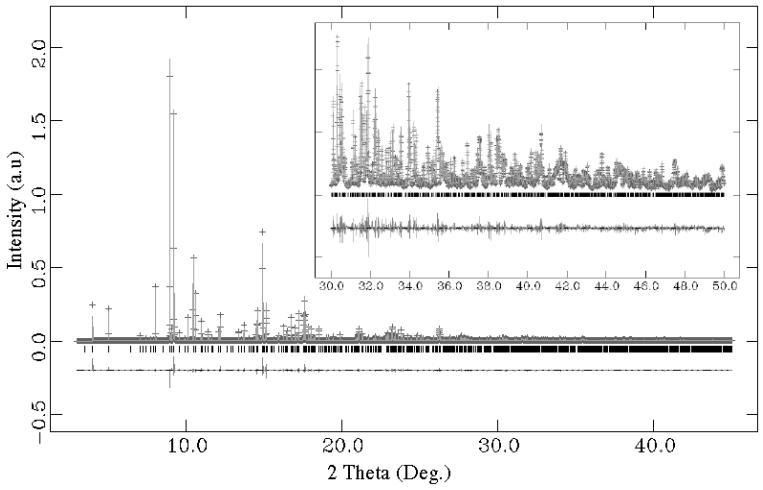

Figure 3.13: Observed, calculated and difference plots for combined Rietveld fit to X-ray diffraction profile of In_2VO_5 at 10K

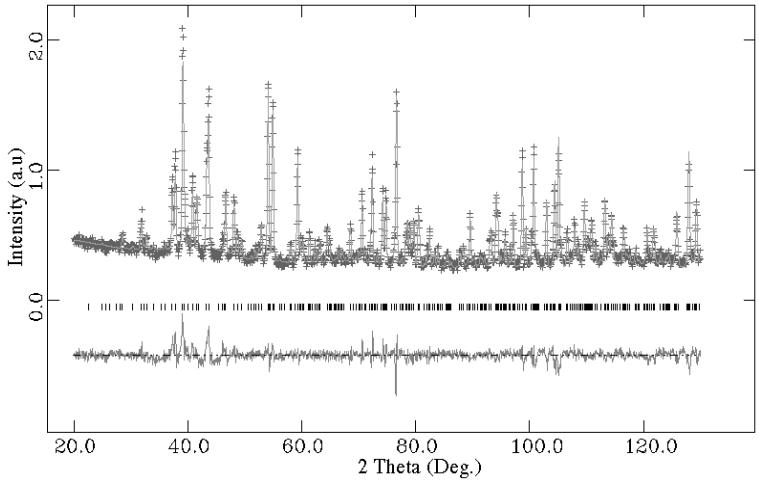

Figure 3.14: Observed, calculated and difference plots for combined Rietveld fit to neutron diffraction profile of In_2VO_5 at 10K

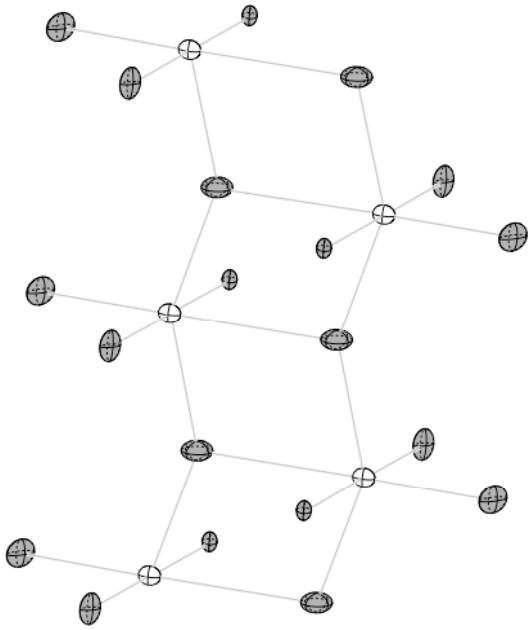

Figure 3.15 Thermal ellipsoids (100 % probability) for VO_6 chains in In_2VO_5 at 10 K.

Table IV: Refined atomic coordinates and anisotropic displacement factors (x 10^2 $Å^2$) for In_2VO_5 at 10 K from combined X-ray and neutron Rietveld refinement.

Atom	*x*	*z*	U_{11}	U_{22}	U_{33}	U_{13}
In(1)	0.0979(5)	0.08391(2)	0.24(2)	0.06(2)	0.09(1)	-0.15(1)
In(2)	0.32998(5)	0.23758(2)	0.28(1)	0.20(2)	0.25(1)	-0.19(1)
V	0.1096(1)	0.42345(6)	0.23(3)	0.26(4)	0.27(3)	-0.10(3)
O(1)	0.2406(4)	0.3224(2)	0.8(1)	0.6(2)	0.1(1)	0.0(1)
O(2)	0.3457(4)	0.4959(1)	0.4(1)	0.7(2)	0.1(1)	0.0(1)
O(3)	0.3699(3)	0.1504(2)	0.2(1)	0.3(2)	0.3(1)	-0.1(1)
O(4)	0.0602(3)	0.1770(2)	0.2(1)	0.3(2)	0.2(1)	0.0(1)
O(5)	0.0687(4)	0.4515(2)	0.8(2)	0.3(2)	0.6(1)	0.0(1)

Table V: Selected V – O bond distances and angles from combined X-ray and neutron refinement at 10 K

Bond/Angle	Distance (Å)/ Angle (°)
V – O(1)	1.770(3)
V – O(2)	2.016(3)
V – O(3)	2.048(3)
V – O(5) x 2	1.806(1)
V – O(5)	2.255(3)
V – O(5) - V	147.2(2)

In order to confirm the absence of long range magnetic order at low temperatures, high flux neutron powder diffraction data were collected at 1.7, 10 and 30 K using instrument D20 at the ILL (Fig. 3.16). All three patterns were well fitted by the crystal

structure refined at 10 K. No evidence for coherent or diffuse magnetic scattering was visible in any of the patterns, or by subtracting high temperature data sets. The downturn in the susceptibilities at 2.5 K and the peak in C_p/T at 4 K do not therefore correspond to a long range ordering transition. Furthermore, the absence of diffuse scattering, which would be expected for a conventional spin glass transition, shows that the moments may still be dynamic below the maximum in $\chi(T)$ [16].

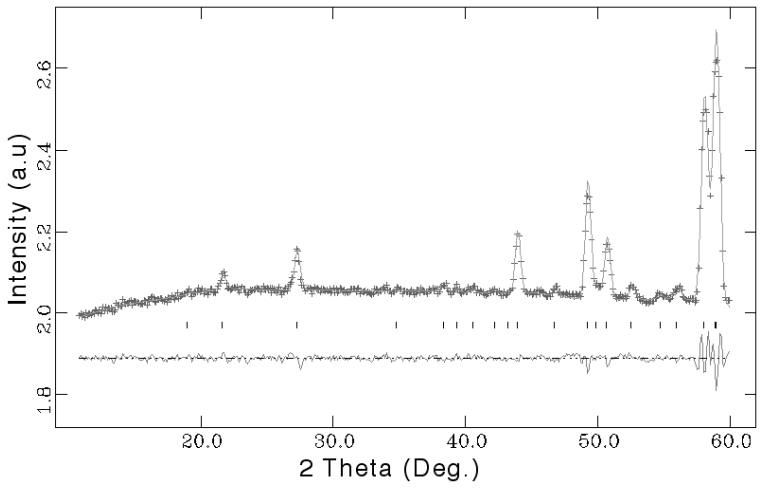

Figure 3.16: Low angle region of Rietveld fit to powder neutron diffraction profile of In_2VO_5 at 1.7 K

3.5. Discussion

The susceptibility, heat capacity and diffraction results reported above show that In_2VO_5 undergoes two magnetic transitions at ca. 120 K and 2.5 K. Furthermore, strong coupling between magnetic and structural degrees is observed at the 120 K crossover. We propose that the zig-zag **S** = 1/2 chains in In_2VO_5 undergo a crossover into a chain of triplet dimers at 120 K, as shown in Fig. 3.1. The paramagnetic moment of 2.1 μ_B calculated for the triplet (**S** = 1) dimerized state, with g = 2.09, is in good agreement with the observed value of 2.2 μ_B below the 120 K crossover. This picture is supported by the heat capacity measurements shown in Fig. 3.5. Two magnetic entropy releases are observed. On warming up to ~100 K, the entropy tends towards the 1/2Rln3 ≈ 4.5 J/mol.K value expected for 1/2

mole of **S** = 1 dimers. Above 120 K, an additional contribution increases the total magnetic entropy to approximately the Rln2 ≈ 5.8 J/mol.K value for the monomeric **S** = 1/2 state. Hence the magnetic heat capacity variation for In_2VO_5 confirms the triplet dimerisation model proposed above. A separate magnetic freezing transition below 5 K is evidenced in the low temperature magnetic susceptibility and heat capacity measurements. The broad magnetic susceptibility maximum at 2.5 K (Fig. 3.3, inset) shows that the global magnetic ground state of In_2VO_5 is a spin singlet, as expected for an antiferromagnetic **S** = 1 chain.

Spontaneous triplet dimerisation has not been reported in frustrated zig-zag chains, however, the **S** = 1 dimer chain is one of the ground states predicted by the F–AF alternating Heisenberg **S** = 1/2 chain model. The ground state of this model varies smoothly from the dimerized (triplet) **S** = 1 Haldane chain to the dimerized (singlet) **S** = 0 chain as the ratio of exchange interactions changes [17,18]. There are few experimental realisations of the triplet chain, but $IPACuCl_3$ is a notable example, showing a susceptibility and excitations characteristic of an **S** = 1 chain with a Haldane gap, and field induced Bose-Einstein condensation [19-21].

We propose that the novel ground state found in In_2VO_5 evidences a high sensitivity of the J_1 interaction to small fluctuating lattice distortions. A weak spin-lattice coupling accompanying the dimer formation in Fig. 3.1 leads to inequivalent J_1 (intradimer) and J_1' (interdimer) interactions. Displacements that give $J_1/J_1' > 1$ reduce magnetic frustration and so the spin dimer fluctuations will couple to these modes. The small anomalies observed in the ***b***-axis parameter and microstrain around the 120 K dimerisation crossover are consistent with changes of longitudinal [010] phonon modes. The sensitivity of the J_1 exchange interactions to local distortion lies in the orientation of the magnetic orbitals in In_2VO_5. The unpaired electrons are localised in d_{xy} type orbitals, perpendicular to the short V-O bonds (marked on Fig. 3.1), which are effectively orthogonal within the J_1 pathways in a symmetric zig-zag chain, leading to ferromagnetic superexchange. A small distortion such as displacement of oxygen atoms parallel to the chain direction removes the orthogonality and introduces a kinetic exchange component that rapidly decreases the strength of one of the now-inequivalent ferromagnetic interactions (J_1'). Hence, longitudinal oxygen vibrations can couple to variations in J_1/J_1' and the corresponding triplet dimer fluctuations. The freezing of the **S** = 1 dimers below 5 K may be accompanied by the ordering of local

displacements, and further studies of the low temperature properties of In_2VO_5 will be worthwhile to discover whether a Haldane gap or lattice distortions are observed. High field investigation of possible Bose Einstein condensation, similar to that in $IPACuCl_3$ [21] also merits investigation.

3.6. Conclusions

In summary, In_2VO_5 shows a novel crossover between $\mathbf{S} = 1/2$ and $\mathbf{S} = 1$ dimer phases at 120 K. This instability reveals a new ground state for the frustrated zig-zag chain. Spin-lattice coupling is evidenced by subtle changes in the cell parameters and strains around the crossover, and this is ascribed to coupling between triplet dimer spin fluctuations and longitudinal oxygen vibrations within the zig-zag chains. The spin dimers freeze into a global singlet state below 5 K without apparent long range magnetic order.

3.7. Future work

There is considerable scope for further measurements on In_2VO_5. A muon spin rotation experiment is scheduled for 2008. This technique has a much higher sensitivity than neutron diffraction for spin freezing transitions and will help distinguish between spin glass and other groundstates. In addition, an application for XYZ polarised neutron diffraction using D7 at the ILL has been submitted. Polarised neutron diffraction will give information on the extent and sign of any static magnetic correlations. Finally, an application for an inelastic neutron scattering experiment using IN4 at the ILL has been made. This experiment will track changes in the dynamic response of In_2VO_5.

References

[1] S. Eggert, I. Affleck, M. Takahashi, *Phys. Rev. Lett.*, **73**, 332 (1994)

[2] F.D.M Haldane, *Phys. Rev. B*, **25**, 4925 (1982)

[3] S.R. White, I. Affleck, *Phys. Rev. B*, **54**, 9862 (1996)

[4] M. Hase, I. Terasaki, K. Uchinokura, *Phys. Rev. Lett.*, **70**, 3651 (1993)

[5] F. Heidrich-Meisner, A. Honecker, T. Vekua, *Phys. Rev. B*, **74**, 020403 (2006)

[6] H.T. Lu, Y.J. Wang, S.J. Qin, T. Xiang, *Phys. Rev. B*, **74**, 134425 (2006)

[7] R. Jafari, A. Langari, *Phys. Rev. B*, **76**, 014412 (2007)

[8] T. Masuda, A. Zheludev, A. Bush, M. Markina, A. Vasiliev, *Phys. Rev. Lett.*, **92**, 177201 (2004)

[9] L. Capogna, M. Mayr, P. Horsch, M. Raichle, R.K. Kremer, M. Sofin, A. Maljuk, M. Jansen, B. Keimer, *Phys. Rev. B*, **71**, 140402 (2005)

[10] S.-L. Drechsler, O. Volkova, A.N. Vasiliev, N. Tristan, J. Richter, M. Schmitt, H. Rosner, J. Málek, R. Klingeler, A.A. Zvyagin, B. Büchner, *Phys. Rev. Lett.*, **98** (2007)

[11] L.M. Volkova, *J. Phys. Condens. Matter*, **19**, 176208 (2007)

[12] U. Schwingenschlögl, *Phys. Rev. B.*, **75**, 212408 (2007)

[13] A. Moller, T. Taetz, N. Hollman, J.A. Mydosh, V. Kataev, M. Yehia, E. Vavilova, B. Buchner, arXiv:0708:2088

[14] Y. Singh, R.W. McCallum, D.C. Johnstone, arXiv:0708.3651

[15] P.J. Senegas, J-P. Manaud, J. Galy, *Acta Cryst.*, **B31**, 1614 (1975)

[16] H. Mutka, *Private Communication*

[17] K. Hida, *Phys. Rev. B*, **45**, 2207(1992)

[18] K. Hida, *Phys. Rev. B*, **46**, 8268 (1992)

[19] H. Manaka, I. Yamada, K. Yamaguchi, *J. Phys. Soc. J*, **66** ,564 (1997)

[20] T. Masuda, A. Zheludev, H. Manaka, L.-P. Regnault, J.-H. Chung, Y. Qiu, *Phys. Rev. Lett.*, **96**, 047210 (2006)

[21] V.O. Garlea, A. Zheludev, T. Masuda, H. Manaka, L.-P. Regnault, E. Ressouche, B. Grenier, J.-H. Chung, Y. Qiu, K. Habicht, K. Kiefer, M. Boehm, *Phys. Rev. Lett.*, **98**, 167202 (2007)

Chapter 4

Magnetism and Polymorphism of MV_2O_6 (M= Mn, Co, Ni) Brannerites

4.1. Introduction

Mixed oxides containing a magnetic and a non-magnetic group V transition metal are a good source of low-dimensional crystal structures as d^0 V^{5+} in particular can adopt a range of coordinations [1]. The magnetic properties of several structural families have been investigated to date, examples include the kagomé staircase compounds $M_3V_2O_8$ (M=Ni, Co) [2-4], and the one-dimensional columbite type MNb_2O_6 materials [5-7]. The quasi-one dimensional Ising ferromagnet $CoNb_2O_6$, in particular, has been the subject of numerous studies after powder neutron diffraction studies showed two successive magnetic transitions on cooling. A transition to an incommensurately modulated phase occurs at 2.9 K followed by a transition to a non-collinear antiferromagnetic phase at 1.9 K [8]. Magnetisation measurements on powder samples at 1.4 K show metamagnetic behaviour and a plateau at 1/3 of the saturation magnetisation [9]. The heat capacity of $CoNb_2O_6$ is characteristic of a system with Ising anisotropy [10] and single crystal neutron diffraction show strongly (*hkl*) dependent coherence lengths [11]. Numerous neutron diffraction studies in applied fields have reported a wealth of distinct field induced magnetic structures and the presence of a Lifshitz point (three phase co-existence) in the field/temperature field diagram [12-17]. One dimensional structures are also found for the MV_2O_6 (M = Mn, Co, Ni, Cu) series. These structures, (monoclinic for M= Mn, triclinic for M = Co, Ni, Cu) are closely related to that of Brannerite (UTi_2O_6) [18-20] and consist of chains of edge-sharing MO_6 octahedra parallel to the b-axis connected by chains of corner and edge sharing VO_5 polyhedra (Fig. 4.1). The magnetic properties of CuV_2O_6 have been widely investigated. Magnetisation measurements

showed a broad maximum at 44 K attributed to one-dimensional spin correlations in the CuO_6 chains, and long range antiferromagnetic order was confirmed at T_N= 24 K by ESR, a metamagnetic transition was also identified with a critical field of 2.7 T at 5 K [21,22]. The intrachain and interchain exchange interactions were estimated to be J_1/k= 34 K and J_2/k= 16.5 K respectively, by fitting an antiferromagnetic spin 1/2 Heisenberg chain and CuV_2O_6 was also studied by powder neutron diffraction and ^{51}V and Cu NMR [23]. The exchange interactions were further examined by spin dimer analysis using the extended Hückel method [24]. Heat capacity measurements [25] confirmed the onset of long range order in CuV_2O_6 to be 22.5 K and Zn doping experiments have shown rapid depression of long range antiferromagnetic order [26] By contrast, the magnetic properties of other MV_2O_6 Brannerites have not been determined.

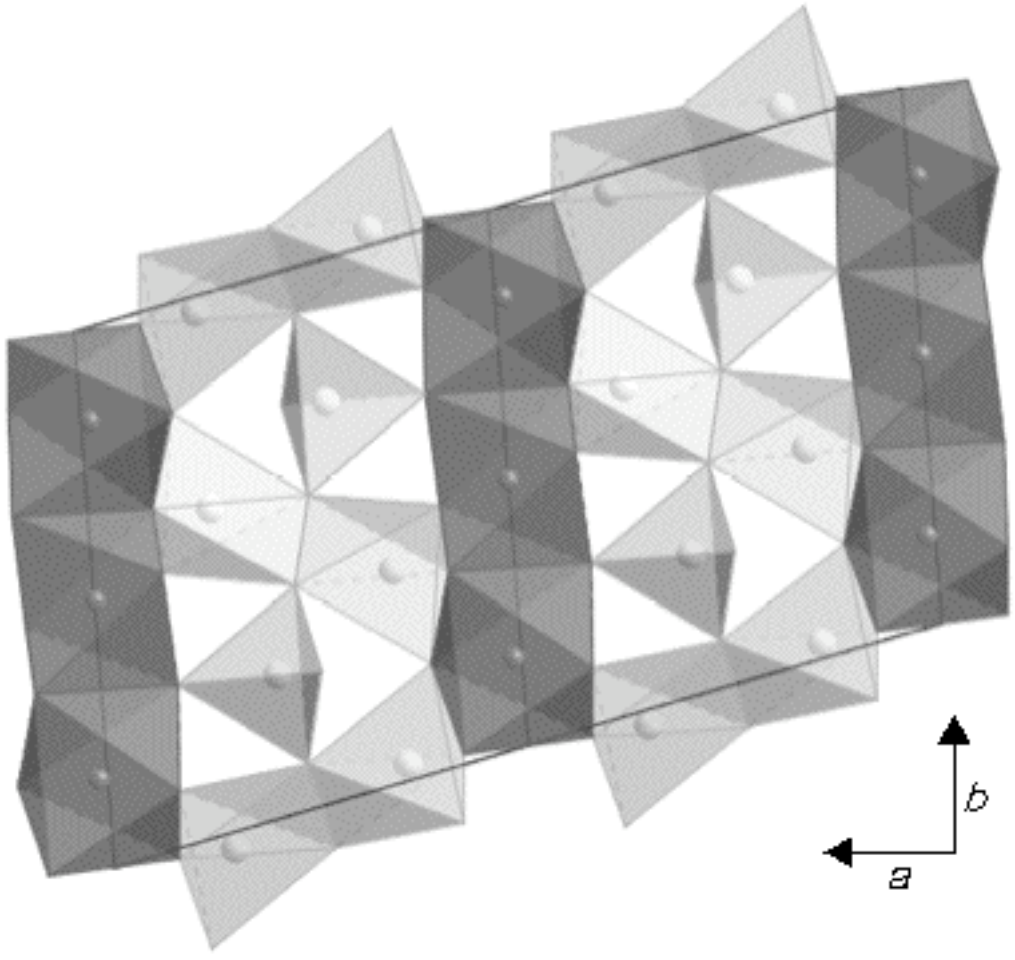

Figure 4.1: Triclinic structure of M= Co, NI, Cu Brannerites projected down [001] showing two unit cells. Dark octahedra are chains of MO_6 octahedra running down [010], light square based pyramids are VO_5.

MV_2O_6 Brannerites have been reported to show polymorphism, CoV_2O_6 can be quenched from high temperature into the monoclinic structure shown by MnV_2O_6 and the whole series has been shown to transform under high pressure and temperatures into the columbite structure reported for the MNb_2O_6 series [27,28]. This chapter is devoted to a systematic investigation of the structural and magnetic properties of these materials.

4.2. Experimental

Polycrystalline MnV_2O_6, CoV_2O_6 and NiV_2O_6 were synthesised by a citrate gel decomposition technique. Stoichiometric quantities of Manganese(II) Acetate Tetrahydrate (Aldrich, 99%+), Cobalt(II) Acetate Tetrahydrate (Aldrich, 99%+), or Nickel(II) Acetate Tetrahydrate (Aldrich, 99%+) and V_2O_5 (Aldrich, 99.99%) were dissolved in distilled water together with a three fold molar excess of acetic acid. The mixture was heated and stirred until a blue gel formed. The gel was allowed to solidify then decomposed at 300° C for three hours. The resulting solid was ground, pelleted and heated at 600, 630 and 650° C for 12, 12 and 72 hours respectively. Magnetic susceptibility measurements were performed using a Quantum Design SQUID magnetometer in zero and field cooled conditions. A Quantum Design PPMS instrument was used to record magnetisation-field isotherms at fixed temperatures in fields up to 90,000 Oe and for heat capacity measurements.

High resolution neutron diffraction patterns were recorded using the instrument Super-D2B at the ILL, Grenoble with a wavelength of λ = 1.594 Å. The medium resolution instrument D1B with λ = 2.52 Å, also at the ILL, was used to follow the temperature dependence of the magnetic structures. Room temperature X-ray diffraction patterns were also recorded using a Bruker D8-Advance diffractometer. The General Structure Analysis System (GSAS) was used to analyse the diffraction data by the Rietveld method.

4.3. Effect of Antisite Disorder on Magnetism in MnV_2O_6

4.3.1. Magnetisation measurements

The susceptibilities for MnV_2O_6 measured in a 1000 Oe field (Fig. 4.2) show a sharp transition to an antiferromagnetically ordered state below T_N = 20 K, with no substantial low-dimensional correlations at higher temperatures. Above 50 K, the inverse susceptibility is well fitted by a Curie-Weiss law with a calculated moment of 5.96(5) μ_B, in good agreement with the expected spin only value for Mn^{2+} (5.92 μ_B). No divergence between zero field and field cooled measurements was seen showing that no ferromagnetism or spin glass behaviour occurs above 1.8 K. However, the Weiss temperature is positive (5.8(1) K), suggesting that significant ferromagnetic exchange interactions are present above T_N. A M(H) isotherm recorded at 2 K (Figure 4.3) showed a linear dependence of moment with field, as expected for a simple isotropic antiferromagnet.

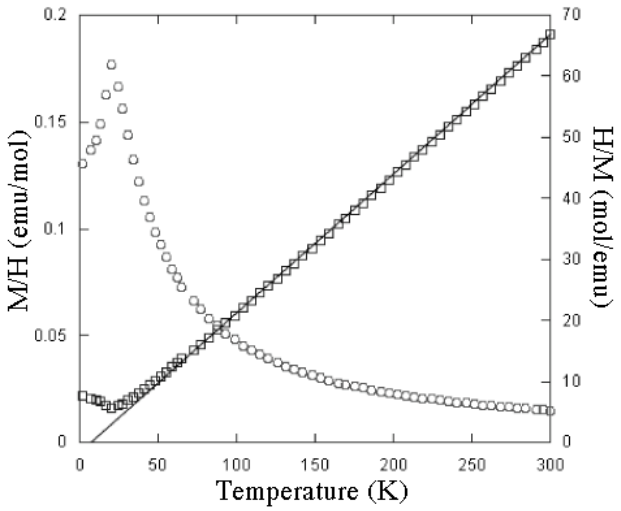

Figure 4.2: Magnetic susceptibility of MnV_2O_6 and inverse susceptibility plotted as a function of temperature. Line shows Curie-Weiss fit to range 50-300 K.

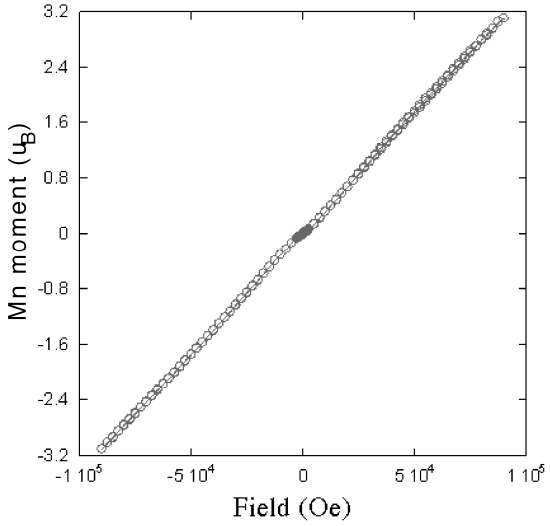

Figure 4.3: M(H) isotherm of MnV_2O_6 measured at 2K.

4.3.2. Neutron powder diffraction results

Powder neutron diffraction patterns were collected using Super-D2B at 5 and 30 K. No structural transitions are observed on cooling to 5 K. The 30 K neutron diffraction profile (Fig. 4.4) was therefore fitted by refining the previously published room temperature structural model for MnV_2O_6 in space group *C*2/*m* [20]. The peak shape was described by a pseudo-Voigt function with a correction for axial divergence [29] and the background was modelled with a linear interpolation function. As Mn and V are both in similar coordination in the Brannerite structure, the possibility of Mn/V antisite disorder was considered. The contrast between the neutron scattering lengths of Mn and V enabled their site occupancies to be refined precisely, under the constraint of preserving stoichiometry, and a small occupancy of 2.9(6)% V at the Mn sites was found. The refinement converged with residuals $_wR_p$= 4.36%, R_p = 3.36% and a goodness-of-fit χ^2 = 2.10. The 30 K structure is similar to that reported previously at 300 K, with tetragonally compressed Mn^{2+} and distorted V^{5+} octahedra.

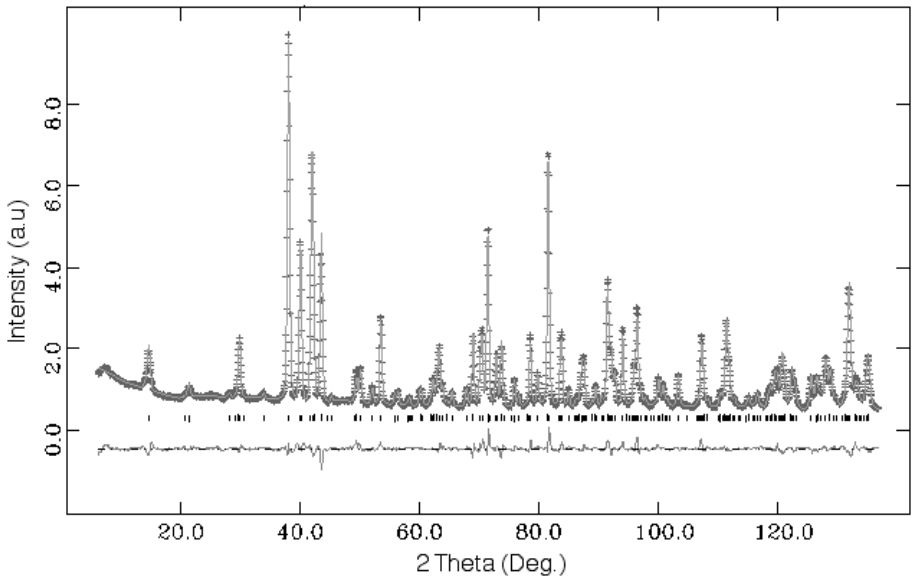

Figure 4.4: Observed, calculated and difference plots for the Rietveld fit to neutron diffraction profile of MnV_2O_6 at 30 K.

The neutron diffraction profile at 5 K (Fig. 4.5) showed additional magnetic scattering peaks at low angles. These peaks belong to the class (h 0 l/2) with odd values of h and l, showing that the magnetic propagation vector is (0,0,1/2). The magnetic intensities were fitted by an antiferromagnetic model in Shubnikov group P_c2/m, in which the Mn spins on (0,0,0) are antiparallel to the spins on (0.5,0.5,0) and (0.5,0.5,0.5) and are aligned in the b-direction. The refined magnitude of the Mn moment is 4.77(7) μ_B.

The 5 K magnetic diffraction peaks from MnV_2O_6 were observed to be significantly broader than the nuclear peaks, and so the Lorentzian peak-broadening coefficients Γ for the two sets of reflections were varied independently. The mean correlation length for the magnetic order ξ was estimated as $\xi = K\lambda/\Delta\Gamma$, where K is the Scherrer constant (0.9). The excess Lorentzian broadening ΔΓ was calculated as the difference between the Γ's for the magnetic (3.09(4) rad.) and nuclear (1.45(5) rad.) reflections, assuming the latter to be limited by instrumental resolution. The estimated magnetic coherence length is thus $\xi \approx 900$ Å for MnV_2O_6 at 5 K. The fit of the magnetic model and the $C2/m$ nuclear structure to the 5 K neutron diffraction data is shown in Fig. 4.5. The residuals are ${}_wR_p = 5.25$ %, $R_p = 4.03$% and $\chi^2 = 3.11$. Results of the 5 and 30 K refinements are summarised in Tables I and II.

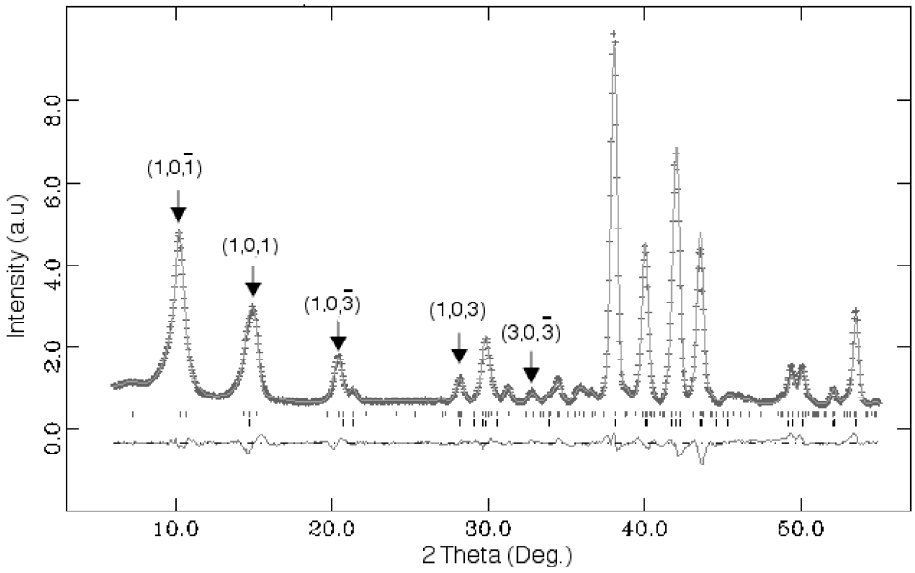

Figure 4.5: Observed, calculated and difference plots for the Rietveld fit to neutron diffraction profile of MnV_2O_6 at 5 K, prominent magnetic peaks are labelled.

Table I: Refined lattice parameters, atomic coordinates and thermal displacement parameters ($Å^2$ x 10^2) for MnV_2O_6 at 5 K and 30 K. Atomic positions are Mn (0,0,0), V (x,0.5,z), O(1) (x,0.5,z), O(2) (x,0.5,z), O(3) (x,0.5,z). Metal site occupancies at 30 K are; Mn site 0.971(6) Mn /0.029(3) V, V site 0.015(3) Mn/0.985(3) V. Wyckoff sites are: Mn1 (*2a*), V1 (*4i*), O1 (*4i*), O2 (*4i*), O3 (*4i*).

	5 K	30 K
a (Å)	9.289(1)	9.289(1)
b (Å)	3.5343(5)	3.5344(4)
c (Å)	6.737(1)	6.738(1)
β (°)	113.00(1)	112.96(1)
Volume ($Å^3$)	203.61(4)	203.71(3)
Mn: Uiso	2.9(6)	1.1(5)
V: *x*	0.309(2)	0.316(2)
V: *z*	0.365(2)	0.359(2)
V: Uiso	2.9(6)	1.1(5)
O(1): *x*	0.1563(2)	0.1566(1)
O(1): *z*	0.1137(3)	0.1147(2)
O(1): Uiso	4.9(3)	5.4(3)
O(2): *x*	0.4684(1)	0.4683(1)
O(2): *z*	0.2902(2)	0.2894(2)
O(2): Uiso	4.8(3)	3.9(3)
O(3): *x*	0.1940(1)	0.1937(2)
O(3): *z*	0.5653(2)	0.5643(2)
O(3): Uiso	6.5(4)	4.4(4)
M_x	0	-
M_y	4.77(7)	-
M_z	0	-

Table II: Selected interatomic distances (Å) and angles (˚) for MnV_2O_6 at 5 K and 30 K.

	5 K	30 K
Mn-O(1) x 4	2.225(5)	2.227(1)
Mn-O(2) x 2	2.088(2)	2.083(1)
<Mn-O>	2.179(2)	2.179(2)
Mn-O(1)-Mn	105.2(1)	105.0(1)
V-O(1) x 1	1.74(2)	1.73(2)
V-O(2) x 1	1.74(2)	1.66(2)
V-O(2) x 1	2.43(2)	2.43(2)
V-O(3) x 2	1.831(4)	1.853(4)
V-O(3) x 1	2.02(2)	2.10(2)
<V-O>	1.93(2)	1.94(2)
Mn-Mn: $\perp b$	4.9695(1)	4.96969(6)
	6.737(1)	6.738(1)
Mn-Mn: $\parallel b$	3.53430(5)	3.53448(5)

The temperature dependence of the magnetic structure was studied over the temperature range 2.3 < T < 25 K using the instrument D1B at the ILL. The observed diffraction profiles are shown in Fig. 4.6 as a function of temperature, the cryostat was set to warm at a rate of 4 $Kmin^{-1}$ and patterns were collected every 2.5 minutes. Prominent magnetic reflections are marked with arrows. The magnetic and structural values obtained from the fit to the high resolution Super-D2B data were used and only the magnetic moment, lattice parameters, background and scale factor were refined. As the monoclinic angle does not change within error from 5 – 30 K in the D2B refinements and taking the low number of observations into account, it was fixed as 113 °. A simple Gaussian model was used to describe the peak shape and the background was modelled by a linear interpolation

method. The Rietveld fit to the observed diffraction profile at 2.3 K is shown in Fig. 4.7, the refinement converged with residuals $_wR_p = 0.1080$, $R_p = 0.0724$.

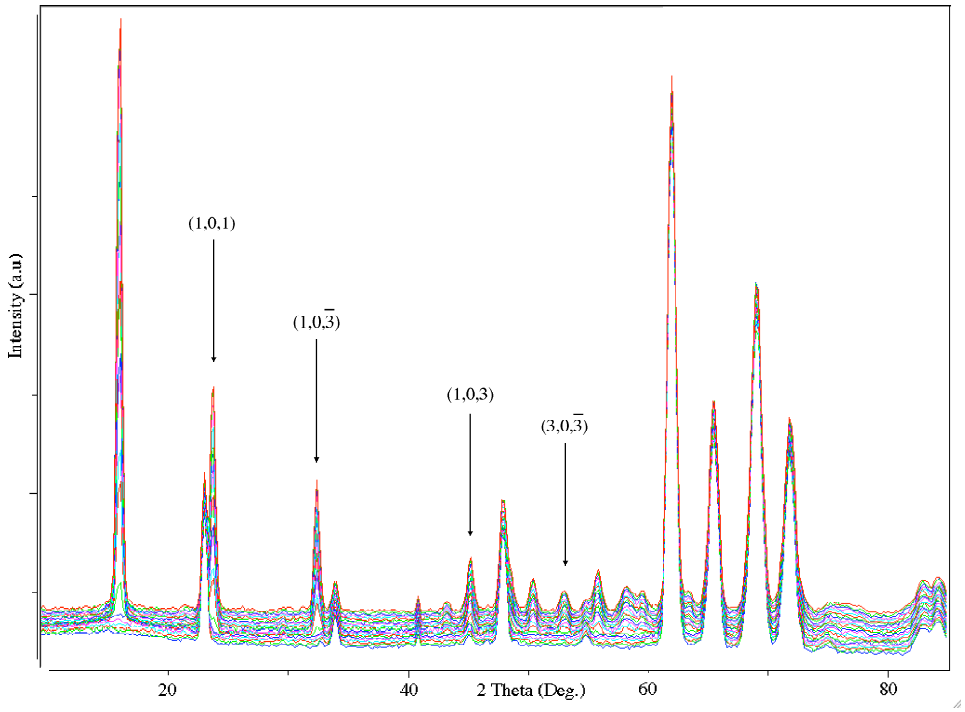

Figure 4.6: Temperature dependence of diffraction profile of MnV_2O_6, patterns were recorded at intervals of 1 K from 2.3 K (top) to 25 K (bottom).

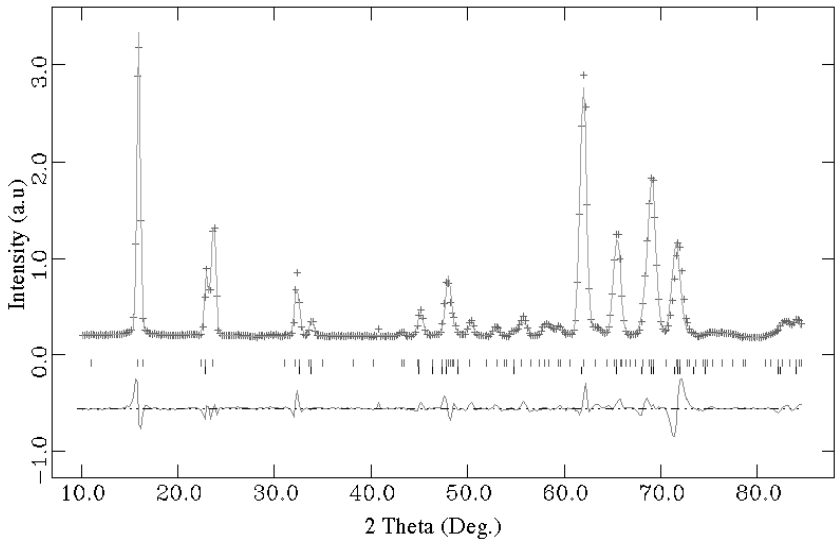

Figure 4.7: Observed, calculated and difference plots for Rietveld fit to neutron diffraction profile of MnV_2O_6 at 2.3 K. Tick markers show position of structural phase (bottom) and magnetic phase (top).

The temperature variation of the refined moments shown in Fig. 4.8 were fitted to a critical law (equation 1), the fit gave a critical exponent, β = 0.349, in close agreement with the value expected for a three dimensional Heisenberg antiferromagnet (0.345 [30].

$$\mu(T) = \mu_0\left[1-\left(\frac{T}{T_N}\right)\right]^{\beta} \tag{4.1}$$

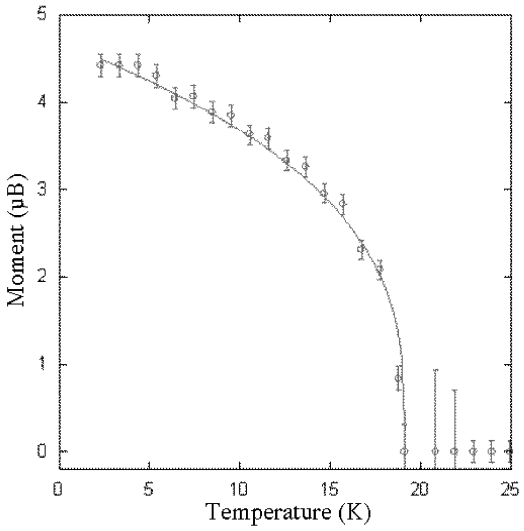

Figure 4.8: Temperature variation of refined magnetic moment of MnV_2O_6, the solid line is a fit to equation 4.1.

4.3.3. Discussion

The above results have shown that MnV_2O_6 undergoes a sharp three dimensional Neel transition at T_N = 20 K with no evidence for low-dimensional magnetism above this temperature. This is surprising in view of the crystal structure and the previously reported antiferromagnetic spin-chain behaviour of the CuV_2O_6 analogue. The refined moment, 4.77(7) μ_B, is close to the expected value of 5 μ_B for Mn^{2+}, with a slight decrease due to covalency as is typical in insulating oxides, but without a large reduction that would indicate significant magnetic frustration.

The observed spin structure of MnV_2O_6 consists of ferromagnetic chains parallel to ***b***, with antiferromagnetic couplings to the nearest chains in the ***a*** and ***c*** directions, as shown in Fig.4.9. Two possible magnetic structures were identified from a previous neutron diffraction study of CuV_2O_6 [23]. Both models have ferromagnetic spin chains but they differ in the couplings between chains. Model A has antiferromagnetic coupling between chains along ***a*** only leading to a propagation vector of (0,0,0), whereas the model B has antiferromagnetic couplings along ***a*** and ***c***, giving a (0,0,1/2) vector. Extended Hückel calculations proposed that the strongest antiferromagnetic interaction is along **c**, which favours model B for CuV_2O_6 [24] . The spin arrangement we have determined for MnV_2O_6 is the same as the model B for CuV_2O_6, suggesting that the differences between their short range orderings do not reflect different long range spin ordered ground states.

Although the long range order in MnV_2O_6 is antiferromagnetic, the positive Weiss temperature shows that significant ferromagnetic interactions are present. This is consistent with the observed parallel alignment of Mn^{2+} spins within the chains of edge-sharing MnO_6 octahedra. Ferromagnetism within such chains is unusual, although $YCa_3(MnO)_3(BO_3)_4$, which also contains chains of edge-sharing $Mn^{2+}O_6$ octahedra, has a positive Weiss temperature of $\theta = 27$ K [31]. Dominant antiferromagnetic direct exchange from e_g-e_g orbital interactions would be expected [32], but this may be outweighed by ferromagnetic t_{2g}-t_{2g} superexchange through the Mn-O-Mn bridges [33]. In contrast, the intrachain exchange interaction in CuV_2O_6 is unexpectedly weak due to orbital ordering as the unpaired electron resides in the d_{x2-y2} type orbital so there is little interaction between nearest neighbour Cu^{2+} spins. A schematic representation of the interchain exchange interactions in MnV_2O_6 is shown in Fig. 4.9. Each chain is coupled antiferromagnetically to the two nearest neighbours via the J[001] and J[100] interactions through the VO_6 octahedra, with only the weaker J[201] and J[20-1] interactions frustrated.

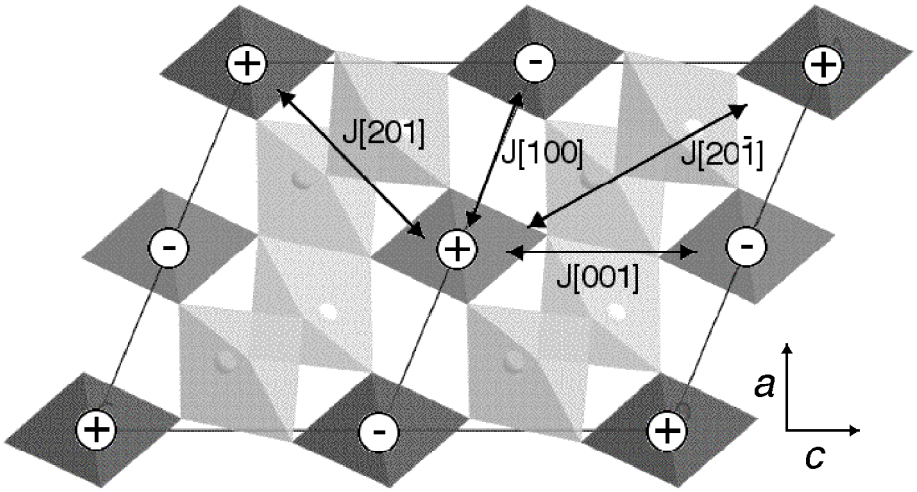

Figure 4.9: Crystal and magnetic structure of MnV_2O_6 projected down [010], dark octahedra are MnO_6 chains, light octahedra are VO_6, + and – symbols represent up and down spins respectively, schematic magnetic interaction pathways are also shown.

Although the magnetic order in MnV_2O_6 appears almost unfrustrated in the ideal structure, the Scherrer broadening of the magnetic diffraction peaks shows that the long range order is frequently disrupted as it is coherent only over ~900 Å (~150 mean lattice repeats) at 5 K. The related material $CoNb_2O_6$, which has a similar structure type, has strongly anisotropic magnetic coherence lengths because of competition between the interchain exchange interactions and single ion anisotropy [34]. No *(hkl)* dependence of the broadening is evident for MnV_2O_6 and we speculate that the origin of the reduced correlation length in MnV_2O_6 is the 3 % Mn/V antisite disorder.

In summary, MnV_2O_6 is found to behave as a 3-dimensional antiferromagnet with a Neel transition at 20 K. The observed ordered magnetic moment is consistent with unfrustrated order of Mn^{2+} S = 5/2 spins. The magnetic structure has a (0 0 1/2) propagation vector, and corresponds to one of the two models previously proposed for CuV_2O_6. No evidence for substantial short range correlations is observed in MnV_2O_6, in contrast to CuV_2O_6, which shows low-dimensional antiferromagnetic correlations. This is likely due to the different balance of exchange interactions because of orbital ordering of Cu^{2+} or the greater contribution of quantum effects for S = 1/2 spins. The coherence length for spin order in MnV_2O_6 is only ~900 Å because of intrinsic Mn/V antisite disorder within this stoichiometric material.

4.4. Metamagnetism and 1/3 Magnetisation Plateau in CoV_2O_6

4.4.1. Physical property measurements

The susceptibilities for CoV_2O_6 shown in Fig. 4.10 show a sharp transition to an antiferromagnetically ordered state below T_N = 7 K. No divergence between field and zero field cooled measurements was seen, showing that there is no ferromagnetism or spin glass behaviour in the temperature range and field studied. The inverse susceptibility of CoV_2O_6 is well fitted by the Curie-Weiss law in the range 125 – 300 K. The calculated moment (5.1(1) μ_B) shows a substantial increase due to spin orbit coupling from the spin only value for S = 3/2 (3.87 μ_B) as is often found for high spin Co(II) in octahedral coordination with a $^4T_{1g}$ ground state[35]. The Weiss temperature is small (0.5(1) K), implying a balance of ferromagnetic and antiferromagnetic exchange interactions in this material.

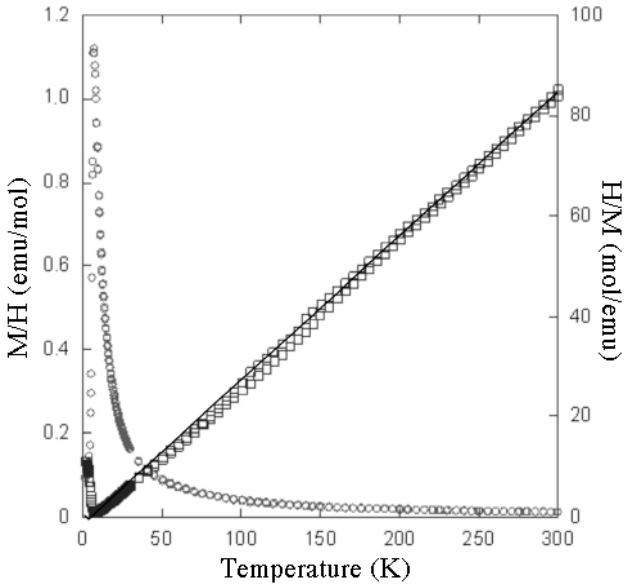

Figure 4.10: Magnetic susceptibilities of CoV_2O_6 measured in zero and field (500 Oe) cooled conditions, line shows Curie-Weiss fit extrapolated to low temperature.

When the magnetic susceptibility was measured using a larger field (10000 Oe), behaviour characteristic of a soft ferromagnet was seen, Fig. 4.11 shows the low temperature region of the susceptibility measurements in 500 (squares) and 10000 Oe (circles) measuring fields.

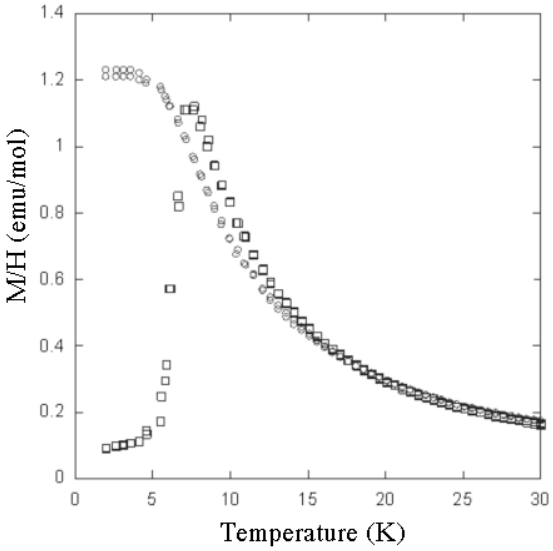

Figure 4.11: Low temperature region of magnetic susceptibility (FC/ZFC) measurements on CoV_2O_6 employing 500 Oe (squares) and 10000 Oe (circles) measuring fields.

The zero field heat capacity measurement for CoV_2O_6 shown in Fig. 4.12 shows a sharp peak corresponding to a long range ordering transition at T_N = 6.3 K. The lattice contribution to the heat capacity was estimated by fitting the high temperature (T > 30 K) heat capacity to a function [36] of the form $AT + BT^3 + CT^5$ and is shown as a solid line in Fig. 4.12. The magnetic entropy was obtained by subtracting the lattice contribution and integrating analytically the resultant magnetic heat capacity and is shown as a dashed line in Fig. 3. The magnetic entropy reached at T_N is only 31 % of the expected value for an effective S = 1/2 spin (Rln2 = 5.76 J/Mol.K), showing that significant low dimensional correlations persist to higher temperatures. The total magnetic entropy we obtain at 25 K (4 J/Mol.K) is similar to results obtained for other Co^{2+} containing materials [37]. The heat capacity of CoV_2O_6 measured in a 1 T field is also shown in Fig. 4.12. The sharp maximum seen in the zero field measurement is significantly suppressed, with an increase in short range order above T_N, and the entropy acquired at T_N is reduced to 0.27Rln2. The heat capacity also no longer diverges at T_N in 1 T applied field.

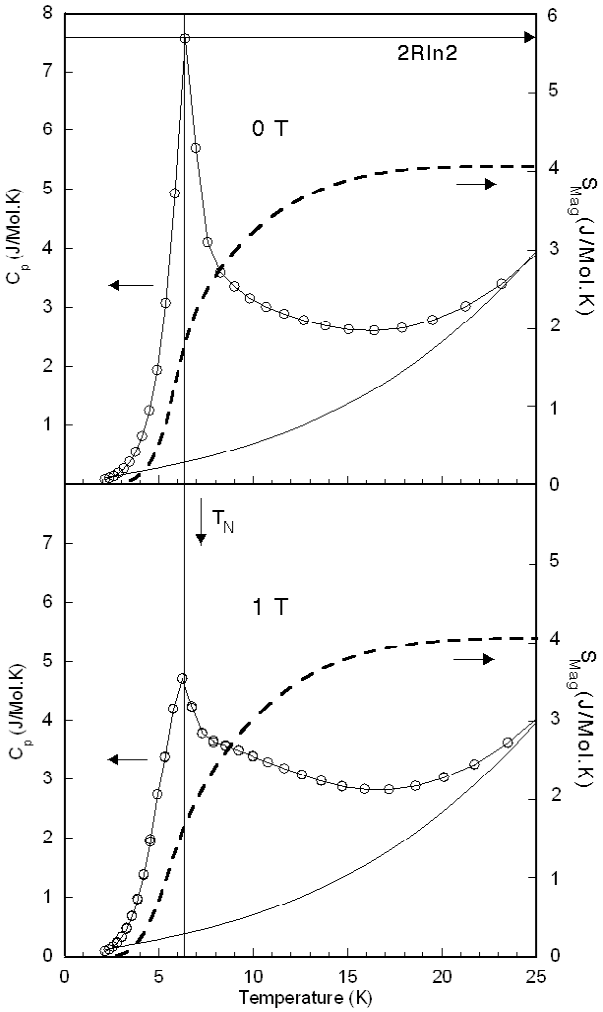

Figure 4.12: Heat capacity of polycrystalline pellet of CoV_2O_6 in the temperature range 2 < T < 25 K measured in zero (top) and 1 T (bottom) applied field. Solid lines show estimated lattice contribution, dashed line shows integrated magnetic entropy. Also shown is theoretical entropy for 1 mole of S = 1/2 spins.

In order to probe the field dependent magnetism in this material, M(H) isotherms were recorded spanning T_N in steps of 1 K from 2 – 10 K and from 10 – 35 K in steps of 5 K in fields up to 9 T. The M(H) isotherm measured at 2 K is shown in Fig. 4.13. Two field induced transitions are seen, the critical field was taken as the maximum in dM/dH (inset Fig. 4.13). The first transition corresponds to a plateau at almost exactly one third of the saturation magnetisation (0.95 μ_B), the second transition is a metamagnetic type transition to a plateau that shows the full saturation magnetisation, 2.9 μ_B at 9 T (μ_{sat} = 2.S = 3μ_B). M(H)

isotherms at temperatures in the range $2 < T < T_N$ show that the 1/3 plateau becomes non-hysteretic at 4 K and disappears between 4.5 and 5 K (Fig. 4.13) whilst the metamagnetic transition persists up to the Neél temperature. Unusually, above T_N, M(H) isotherms characteristic of a soft ferromagnet are observed, isotherms recorded in 5 K steps from 10 – 35 K are shown in Fig. 4.14.

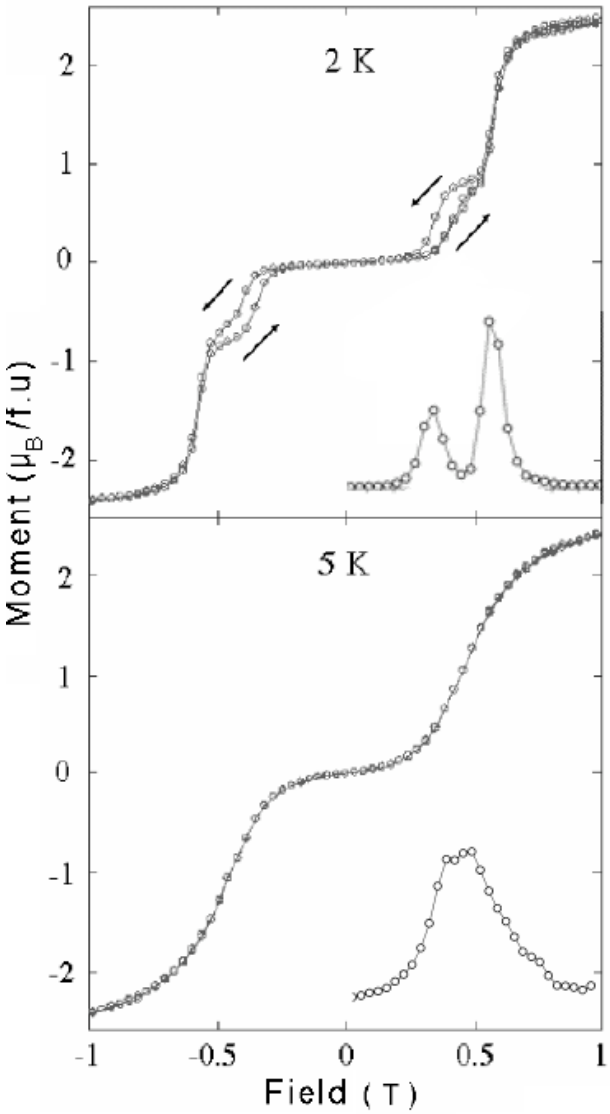

Figure 4.13: M(H) isotherms measured for CoV_2O_6 at 2 (top) and 5 K (bottom). Insets show dM/dH used to estimate critical fields.

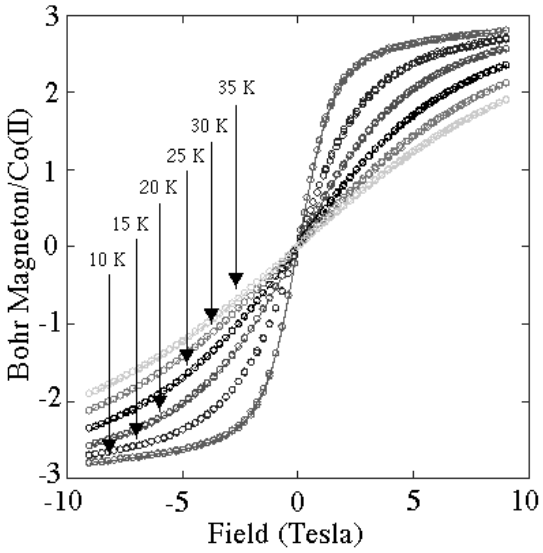

Figure 4.14: M(H) isotherms recorded for CoV_2O_6 at 5 K intervals from 10 < T < 35 K.

According to mean field theory, a plot of M^2 vs. H/M (Arrot plot) for a system with a spontaneous magnetisation should show a series of parallel lines at high field near T_c, with the line at $T = T_c$ passing through the origin [38]. The Arrot plot of the M(H) isotherms at 10 < T < 35 K for CoV_2O_6 is shown in Fig. 4.15. Below 15 K, a spontaneous magnetisation is observed.

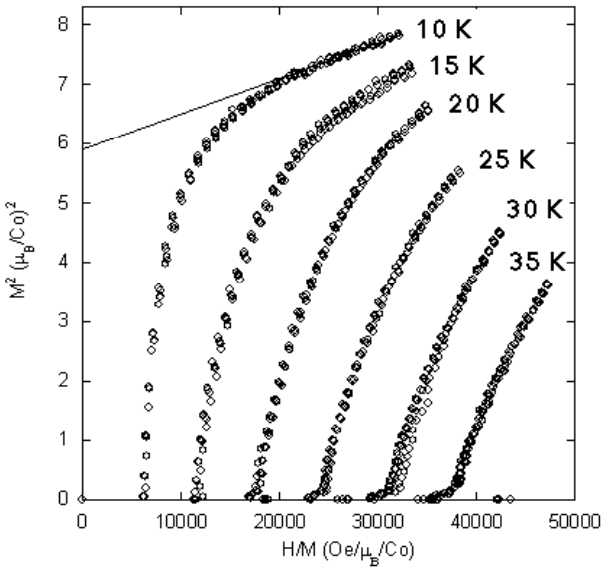

Figure 4.15: Arrot plot of M(H) isotherms recorded between 10 and 35 K for CoV_2O_6.

4.4.2. Neutron powder diffraction results

The crystal structure of CoV_2O_6 was refined from high resolution neutron diffraction data collected at 5 K using Super-D2B, additionally, the diffraction profile showed the emergence of additional peaks at low angles that were attributed to long range magnetic order. The previously published room temperature structure [19] was chosen as a structural starting model and possible propagation vectors for the magnetic structure were tested. The peak shape was described by a pseudo-voigt function and the background was described by a linear interpolation function. The isotropic displacement parameters of V(1), V(2) and V(3) were constrained to those of Co(1) and Co(2) as the neutron scattering length of vanadium is low. All of the reflections that were not predicted by the crystallographic model could be indexed using a propagation vector $\mathbf{k} = (1/2,0,0)$, an antiferromagnetic model consisting of ferromagnetic edge sharing chains coupled antiferromagnetically along ***a*** was refined and gave the fit shown in Fig. 4.16. The Lorentzian peak shape parameters for the structural and magnetic phase were refined independently and agreed within error, showing that the coherence length for the magnetic structure is comparable to that of the crystal structure. In contrast to the related material MnV_2O_6, no evidence for antisite disorder was detected [39]. The refinement converged with $\chi^2 = 3.07$, ${}_wR_p = 0.0548$, $R_p = 0.0426$, and gave the results in Tables III and IV. The refined moment was 4.14(2) μ_B.

When the long wavelength diffractometer D1B was used to examine the temperature dependence of the magnetic structure of CoV_2O_6, an additional magnetic satellite at low angle (d = 15.8 Å) was seen (arrowed in Fig. 4.17). In the Super-D2B data set, this reflection is masked by low angle asymmetry. The satellite shows the same temperature dependence as the principle magnetic reflections and is therefore magnetic in origin. As attempts to index this reflection were unsuccessful, it may be an indication of a long period incommensurate modulation of the simple collinear structure determined from the Super-D2B data. Despite this, the D1B data were used to extract a critical exponent for the magnetic ordering transition in CoV_2O_6. The intensity of the largest magnetic reflection is plotted as a function of temperature in the inset to Fig. 4.16. The line is a fit to the expression $\mu(T) = \mu_0[1-(T/T_N)]^{2\beta}$, the fitted value of $\beta = 0.2$.

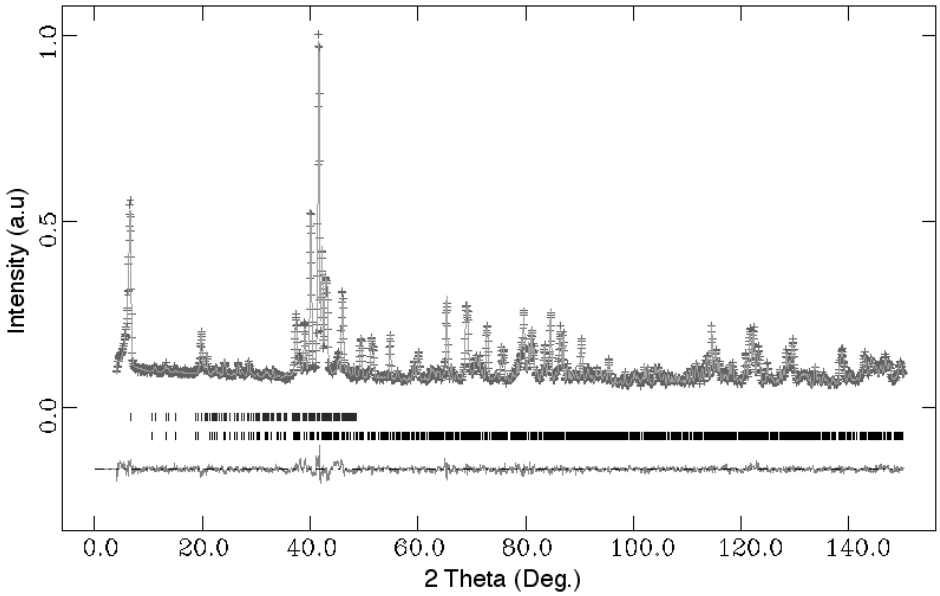

Figure 4.16: Observed, calculated and difference plots for Rietveld fit to neutron diffraction profile of CoV_2O_6 at 5 K from Super-D2B.

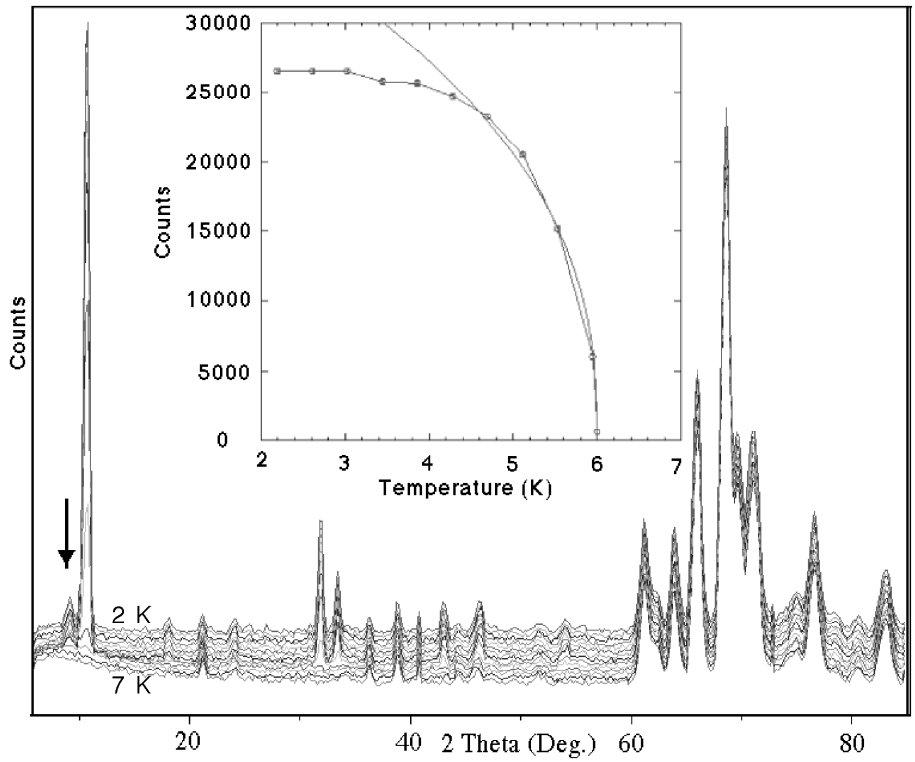

Figure 4.17:. Temperature dependence of neutron diffraction profile of CoV_2O_6 (D1B) from 2 K (top) to 7 K (bottom). Arrow marks satellite reflection referred to in text. Inset shows temperature evolution of strongest magnetic reflection and fit to critical law.

Table III: Refined atomic coordinates and displacement parameters for CoV_2O_6 at 5 K. Lattice parameters *a* = 7.172(1), *b* = 8.875(1), *c* = 4.8088(8) Å, α = 90.288(2), β = 93.931(2), γ = 102.160(1) °.

Atom	Site	x	y	z	Uiso ($Å^2x10^2$)
Co(1)	*1c*	0	0.5	0	0.2(1)
Co(2)	*2i*	0.0145(20)	0.1699(16)	0.0236(25)	0.2(1)
V(1)	*2i*	0.69(1)	0.98(1)	0.45(2)	0.2(1)
V(2)	*2i*	0.72(1)	0.61(1)	0.49(2)	0.2(1)
V(3)	*2i*	0.56(1)	0.25(1)	0.1(2)	0.2(1)
O(1)	*2i*	0.1627(10)	0.4901(7)	0.3468(13)	0.73(3)
O(2)	*2i*	0.8403(10)	0.6377(8)	0.1673(13)	0.73(3)
O(3)	*2i*	0.1786(9)	0.6981(8)	0.8863(13)	0.73(3)
O(4)	*2i*	0.1526(9)	0.0226(8)	0.8237(12)	0.73(3)
O(5)	*2i*	0.1637(10)	0.8882(7)	0.3472(15)	0.73(3)
O(6)	*2i*	0.7831(8)	0.7980(9)	0.6312(13)	0.73(3)
O(7)	*2i*	0.4734(9)	0.9140(8)	0.7069(13)	0.73(3)
O(8)	*2i*	0.4784(11)	0.5757(8)	0.7082(13)	0.73(3)
O(9)	*2i*	0.5242(9)	0.7521(8)	0.2079(13)	0.73(3)

Table IV: Selected interatomic distances (Å) and angles (°) for CoV_2O_6 at 5 K

Bond	Distance (Å) / Angle(°)
Co(1) – O(1) x 2	1.982(6)
Co(1) – O(2) x 2	2.039(7)
Co(1) – O(3) x 2	2.046(6)
Co(2) – O(2)	2.059(16)
Co(2) – O(3)	2.057(16)
Co(2) – O(5)	2.116(14)
Co(2) – O(6)	2.105(14)
Co(2) – O(4) x 2	2.068(15), 2.041(16)
Co(1) – O(2) – Co(2)	92.3(5)
Co(1) – O(3) – Co(2)	92.1(5)
Co(2) – O(4) – Co(2) x 2	93.2(6)
Co(1) – Co(2) || *b*	2.955(14),
Co(2) – Co(2) || *b*	2.986(28)

4.4.3. Discussion

The above susceptibility, heat capacity and powder neutron diffraction results show that, on cooling to 2 K in zero field, CoV_2O_6 undergoes a single magnetic transition at T_N = 6.3 K. The magnetic structure of CoV_2O_6 is complex, but can be approximated by a simple model of ferromagnetic planes coupled antiferromagnetically along ***a***. The refined distances and angles shown in Tables I and II show that the structure of CoV_2O_6 approximates to a rectangular lattice. Schematic exchange pathways are shown in Fig. 4.18. The mean Co – Co distances in the ***bc*** plane are 2.97(2) Å along [010] and 4.81(3) Å along [001]. Neighbouring planes are separated by 7.17(3) Å along [100]. As the Co – O – Co bond angles along the edge sharing chains lie in the range 92.1(5) – 93.2(6) °, we expect J[010] to be dominated by ferromagnetic superexchange. The weaker interchain interactions are therefore antiferromagnetic with $|J[100]+J[001]| \approx J[010]$. Intra-sublattice antiferromagnetic exchange is necessary for an intermediate plateau in the magnetisation of simple metamagnets [40,41].

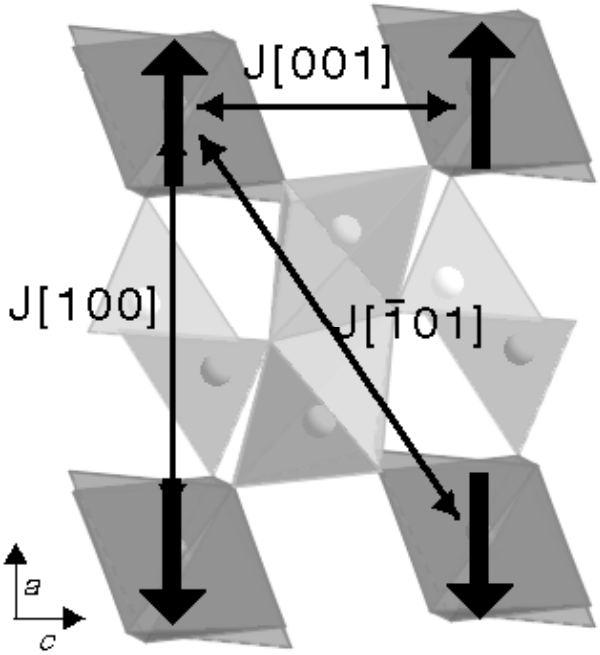

Figure 4.18: Crystal structure of CoV_2O_6 projected down [010], dark octahedra are CoO_6, light polyhedra are VO_5/VO_6, schematic magnetic exchange pathways are also shown.

The heat capacity of an S = 1/2 Ising two dimensional lattice is known exactly and shows a λ anomaly even for very large ratios of interplane exchange interactions [42]. In the case of CoV_2O_6, the magnetic entropy acquired at T_N (0.31Rln2) is close to that expected at T_N for a two dimensional Ising magnet (0.44Rln2) and significantly less than that predicted for a three dimensional Ising magnet (0.81Rln2) [43]. The fitted critical exponent (β = 0.2) is intermediate between the values expected for a quadratic two dimensional Ising model (0.125) and a three dimensional Ising model (0.313) [44]. Together, these results imply that CoV_2O_6 has considerable two-dimensional character. The M(H) isotherms shown in Fig. 4.14 and 4.15 show that the short range order at $T > T_N$ is ferromagnetic, and a field of a few Tesla is sufficient to completely saturate the moments at 10 K.

The schematic phase diagram we have determined from our measurements (Fig. 4.19) is similar to that determined for the model metamagnetic materials $MCl_2.2H_2O$ (M = Fe, Co) with a triple point where the phase lines for the paramagnetic, 1/3 plateau and antiferromagnetic regions meet [45-49]. The $MCl_2.2H_2O$ materials also shown similarly low Weiss constants (1±1 K for M = Co) [50]. However, the zero field magnetic structures of this

family of materials are simple collinear arrangements [51] and heat capacity measurements show that the entropy acquired at T_N for $CoCl_2.2H_20$ is significantly higher (0.6Rln2) than we have determined for CoV_2O_6 [52]. In addition, the critical exponent we have determined for CoV_2O_6 (0.2) is also significantly lower than that observed for $FeCl_2.2H_2O$ and $CoCl_2.2H_2O$ (0.3 and 0.32 respectively) [53]. These differences between CoV_2O_6 and simple metamagnetic systems suggest that further experiments on single crystals in high fields at low temperatures may uncover complicated behaviour similar to that seen in the related material $CoNb_2O_6$.

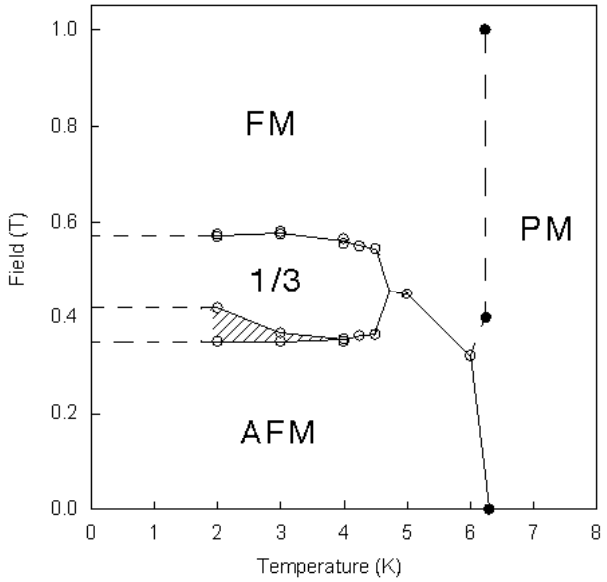

Figure 4.19: Schematic temperature/field phase diagram for CoV_2O_6 based on results from magnetisation (o) and heat capacity (•) measurements. Hatched region shows extent of hysteresis.

4.5. Polymorphism in NiV_2O_6

4.5.1. Ambient pressure structure and properties

A powder X-ray diffraction pattern of α-NiV_2O_6 was collected at room temperature using a Bruker D8 Advance. the diffraction profile (Fig. 4.20) was fitted using the reported room temperature structure [18]. The peak shape was modelled with a pseudo-voigt function and the background was modelled using a linear interpolation function. Due to the

low symmetry (P-1), only the scale factor, lattice parameters, zero shift, displacement parameters and peak shape coefficients were refined. The refinement converged with χ^2 = 9.06, $_wR_p$ = 0.0421, R_p = 0.0255 with the lattice parameters a = 7.1242(1), b = 8.8236(1), c = 4.7906(1) Å, α = 90.016(3), β = 94.227(1), γ = 101.954(2) ° V = 293.79(1) Å^3. Some regions of anisotropic broadening were apparant (e.g. 25 – 30 °), several simple broadening models were tried although none produced significant improvement in the fit.

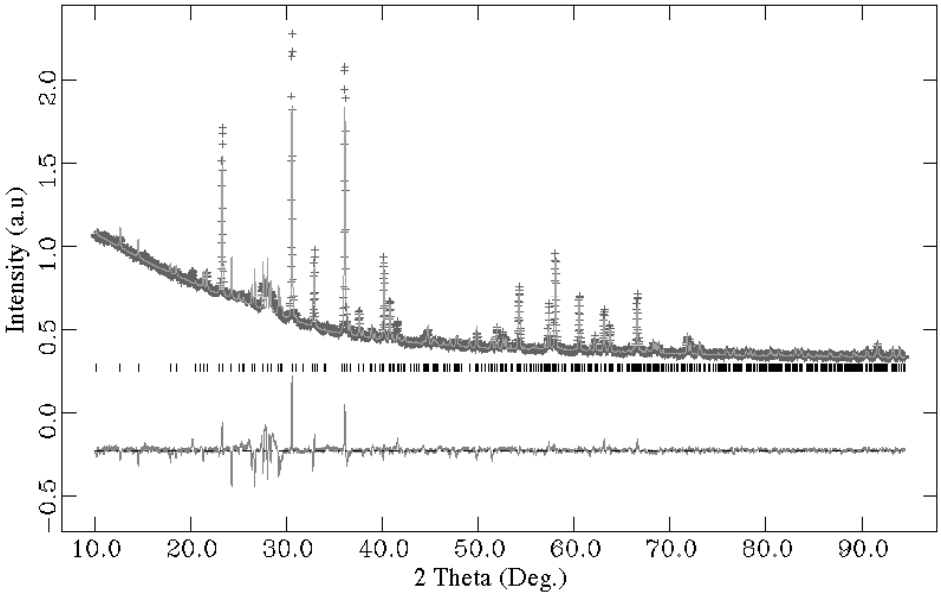

Figure 4.20: Observed, calculated and difference plots for Rietveld fit to X-ray diffraction profile of NiV_2O_6 at room temperature.

The magnetic susceptibilities for NiV_2O_6 measured in a 500 Oe field are shown in Fig. 4.21, an antiferromagnetic transition is seen at T_N = 14 K. The inverse susceptibility was fitted to a Curie-Weiss law in the temperature region 200 < T < 300 K and yielded a paramagnetic moment of 3.1(2) μ_B and a Weiss constant, Θ = -14(2) K. In contrast to MnV_2O_6 and the isostructural material CoV_2O_6, the dominant exchange interactions appear to be antiferromagnetic in this material. However, the inverse susceptibility shows curvature over the entire temperature range, perhaps due to magnetic impurities. The inverse susceptibility also diverges below about 150K, which may be an indication of ferromagnetic correlations. There was no divergence between field and zero field cooled measurements.

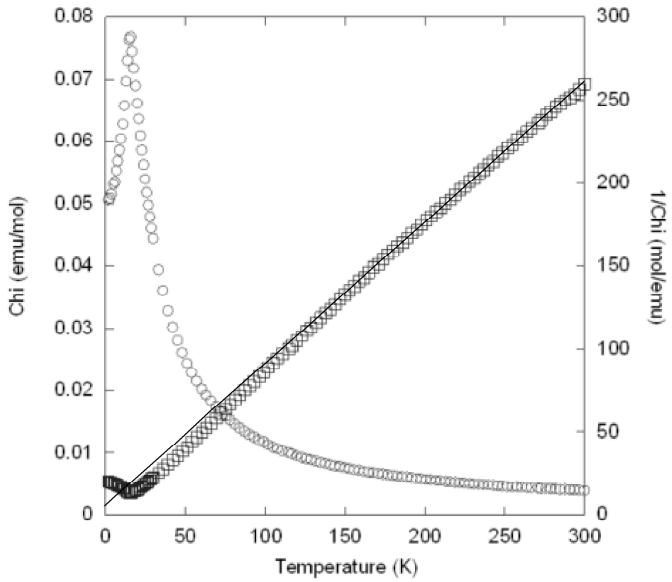

Figure 4.21: Magnetic susceptibility of NiV_2O_6 and inverse susceptibility plotted as a function of temperature. Line shows Curie-Weiss fit to range 200-300 K.

Magnetisation/field isotherms were recorded at 2, 5, 10 and 15 K, a metamagnetic transition, similar to that seen in CoV_2O_6 and CuV_2O_6 was seen with a critical field, H_c = 1.6 T at 2 K , but with no evidence for a 1/3 plateau. These measurements are shown in Fig. 4.22.

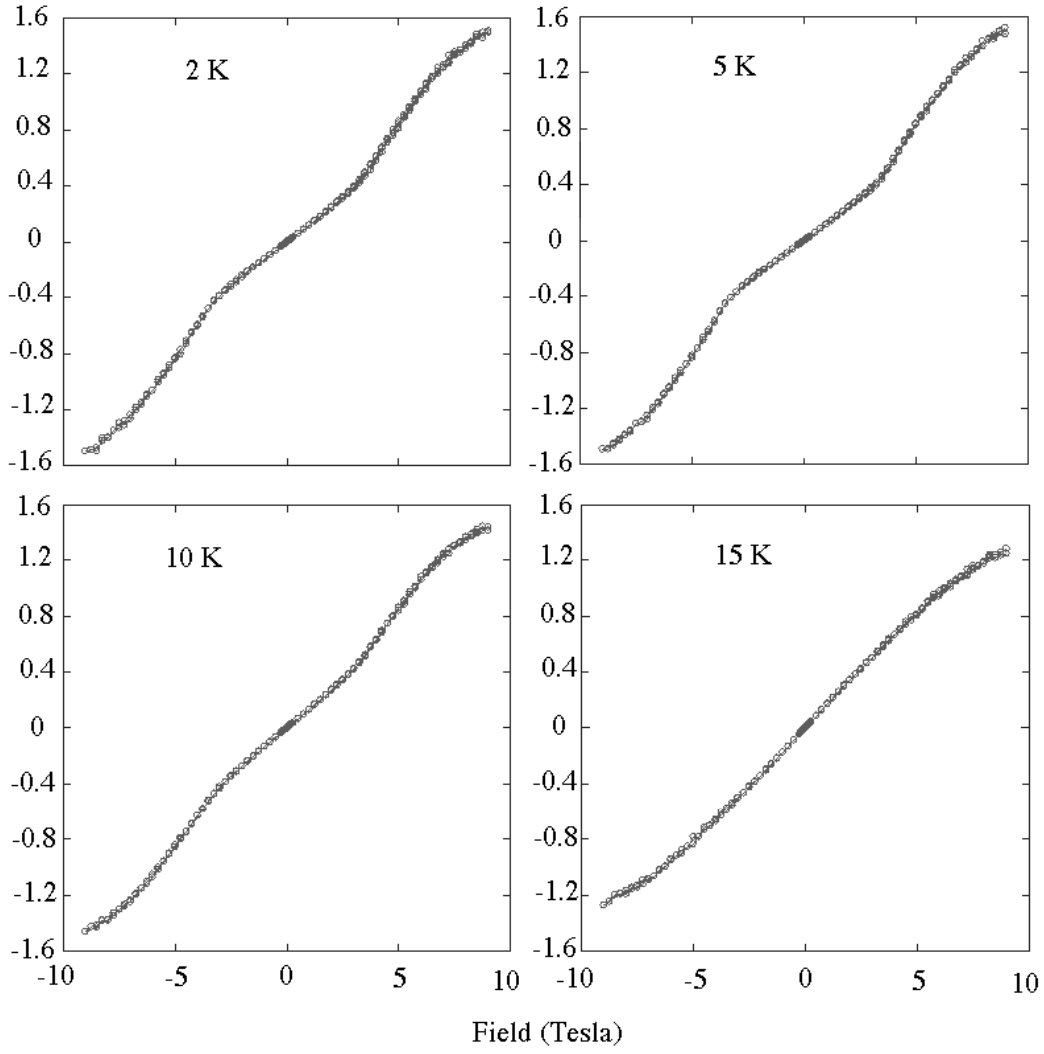

Figure 4.22: M(H) isotherms recorded at various temperatures for NiV_2O_6

4.5.2. High pressure structure and properties

A sample of NiV_2O_6 was treated at 6 GPa and 900 ° C for 15 min in a multianvil press. The product gave a powder X-ray diffraction profile that could be indexed by an orthorhombic cell with a = 13.3632(2), b = 5.5283(1), c = 4.81111(5) Å. The columbite structure (Fig. 4.23) is a $\sqrt{2}a$ x b x c superstructure of α-PbO_2, the calculated cell volume of NiV_2O_6 is 355.426(3) Å^3 for the columbite cell and 251.319 Å^3 for the disordered α-PbO_2 sub cell. A Rietveld refinement was performed using the *Pbcn* columbite structure of $NiNb_2O_6$ as a starting model. The refinement converged with ${}_wR_p$ = 0.0183, R_p = 0.0141 and χ^2 = 1.157, the

observed, calculated and difference plots are shown in Fig. 4.24 and the refined atomic positions and displacement parameters shown in Table VI.

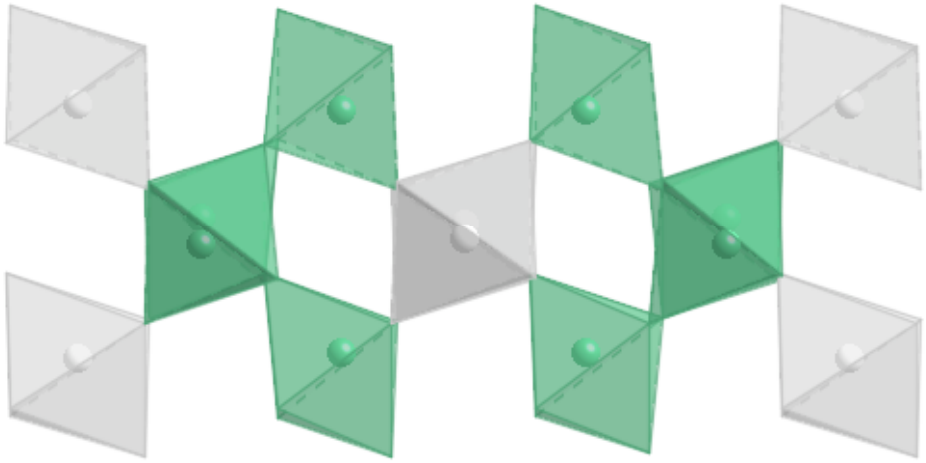

Figure 4.23: NiV_2O_6 Columbite structure projected down edge sharing zig-zag chains, dark octahedra are VO_6, light octahedra are NiO_6.

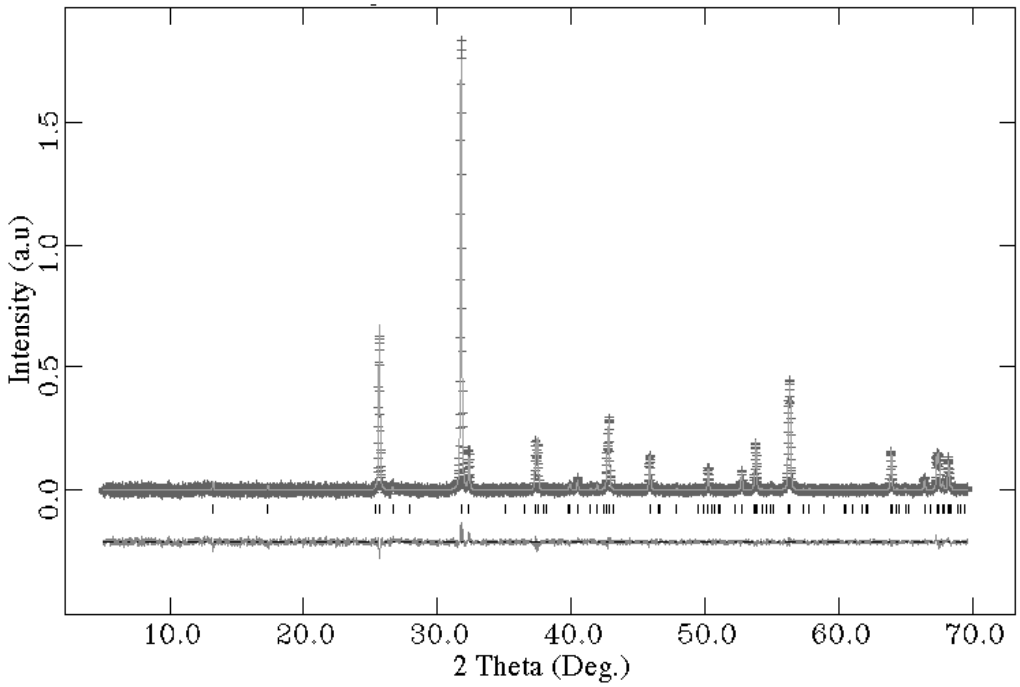

Figure 4.24: Observed, calculated and difference profile for Rietveld fit to room temperature X-ray diffraction profile of β-NiV_2O_6 columbite.

Table VI: Refined atomic positions and displacement parameters for β-NiV_2O_6 at room temperature.

Atom	Site	x	y	z	Uiso ($Å^2x10^2$)
NI(1)	*4*	0	0.3374(9)	0.25	2.39(4)
V(1)	*8*	0.1634(3)	0.1798(5)	0.7590(12)	2.39(4)
O(1)	*8*	0.0966(8)	0.1077(24)	0.0593(24)	1.27(9)
O(2)	*8*	0.4127(9)	0.1317(26)	0.0896(23)	1.27(9)
O(3)	*8*	0.7592(11)	0.1219(37)	0.0989(25)	1.27(9)

The magnetic susceptibilities of β-NiV_2O_6 measured in a 500 Oe field are shown in Fig. 4.25, an antiferromagnetic transition was seen at 2.5 K. A Curie-Weiss fit to the inverse susceptibility in the range 200 < T < 300 K gave a moment of 3.6(3) μ_B and a Weiss constant of –17(2) K. Again, significant curvature of the inverse susceptibility is seen.

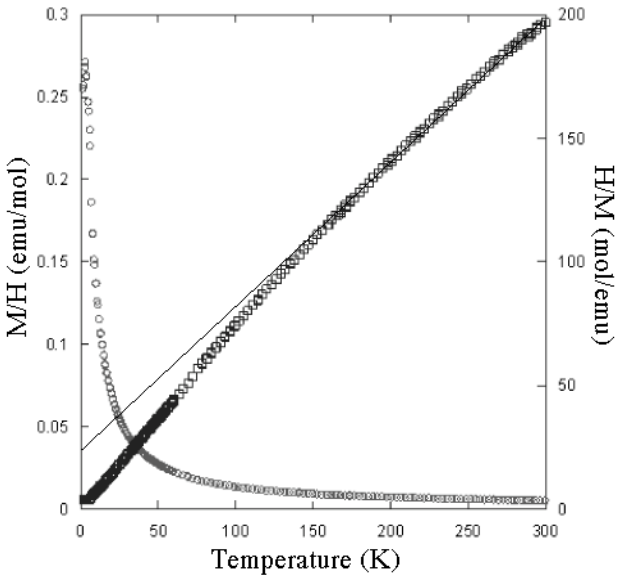

Figure 4.25: Magnetic susceptibilities of β-NiV_2O_6 and inverse susceptibility plotted as a function of temperature. Line shows Curie-Weiss fit to range 200 – 300 K.

4.5.3. Discussion

In common with other MV_2O_6 Brannerites, α-NiV_2O_6 shows a single antiferromagnetic transition at T_N = 14 K. Metamagnetism, similar to that observed in other

triclinic Brannerites is also seen. The high pressure polymorph, β-NiV_2O_6 is also antiferromagnetic with a lower Neel temperature T_N = 2.5 K. This phase transformation is driven by an increase in V^{5+} coordination from 5 to 6 and by a large volume decrease of 14.45 %.

4.6. Overall Conclusions

The magnetic properties of the MV_2O_6 Brannerite family are summarised in Table VII. These materials can be grouped into two classes, the monoclinic compound MnV_2O_6 which is a typical isotropic Heisenberg antiferromagnet, and the triclinic M = Co, Ni and Cu materials which show more anisotropic behaviour.

The unusual metamagnetic properties of CoV_2O_6 and the complex magnetic structure observed can be ascribed to the strong Ising type anisotropy of Co^{2+}. Likewise, by comparison with our results, the low dimensional correlations in CuV_2O_6 are caused by anisotropic exchange enforced by orbital order of Jahn-Teller distorted Cu^{2+}.

Table VII: Magnetic properties of MV_2O_6 phases[1]

Compound	Neél Temperature (K)	Weiss Constant (K)	H_C (T)
MnV_2O_6	20	5.8	-
CoV_2O_6	6.3	0.5	0.32, 0.5
NiV_2O_6	14	-14	1.6
CuV_2O_6	22.5	-34	2.7

The trend from dominant ferromagnetic exchange in MnV_2O_6 to antiferromagnetic exchange in CuV_2O_6 may simply be a size effect, the size of transition metal M^{2+} cations decreases across the first row, the smaller resulting metal-metal distances may allow antiferromagnetic e_g - e_g direct exchange to dominate over ferromagnetic t_{2g} - t_{2g} superexchange. Similar correlations have been reported for various series of chalcogenide

[1] Parameters for CuV_2O_6 taken from references 21,23

spinels, for example in the series $CdCr_2X_4$ and $ZnCr_2X_4$ (x = O, S, Se), the Weiss constant varies linearly with the cubic lattice parameter [54]. The trend towards antiferromagnetic exchange from Co – Cu is also reflected by the increasing critical field at the metamagnetic transition.

4.7. Future Work

The Brannerite materials show great potential for future work, in particular, further investigation of the complex magnetic behaviour exhibited by CoV_2O_6. Single crystal neutron diffraction in zero and applied fields would be ideal to clarify details of the various magnetic structures. As the magnetic structure in zero field is incommenusurate, measuring the dielectric properties of this materials may also be worthwhile. It would also be interesting to quench the monoclinic polymorph of CoV_2O_6 from high temperature and compare its magnetic properties to the triclinic phase studied above. Further work is also clearly merited to synthesise and characterise the remaining β-MV_2O_6 phases.

References:

[1] P.Y. Zavalij, M.S. Whittingham, *Acta. Cryst. B*, **55**, 627 (1999)

{2] R. Szymczak, M. Baran, R. Diduszko, J. Fink-Finowicki, M. Gutowska, A. Szewczyk, H. Szymczak, *Phys. Rev. B*, **73**, 094425 (2006)

[3] Y. Chen, J.W Lynn, Q. Huang, F.M. Woodward, T. Yildirim, G. Lawes, A.P. Ramirez, N. Rogado, R.J. Cava, A. Aharony, O. Entin-Wohlman, A.B. Harris, *Phys. B,* **74**, 014430 (2006)

[4] N. Rogado, G. Lawes, D.A. Huse, A.P. Ramirez,, R.J. Cava, *Solid State Comm.*, **124**, 229 (2002)

[5] O.V. Nielsen, B. Lebech, F. Krebs Larsen, L.M. Holmes, A.A. Ballman, *J. Phys. C.*, **9**, 2401 (1976)

[6] I. Yaeger, A.H. Morrish, B.M. Wanklyn, B.J. Garrard, *Phys. Rev. B*, **16**, 2289 (1977)

[7] I. Yaeger, A.H. Morrish, B.M. Wanklyn, *Phys. Rev. B*, **15**, 1465 (1977)

[8] W. Sharf, H. Weitzel, I. Yaeger, I. Maartense, B.M. Wanklyn, *J. Mag. Mag. Mat.*, **13**, 121 (1979)

[9] I. Maartense, I. Yaeger, B.M. Wanklyn, *Solid State Comm.*, **21**, 93 (1977)

[10] T. Hanawa, K. Shinkawa, M. Ishikawa,K. Miyatani, K. Saito, K. Kohn, *J. Phys. Soc. J.*, **63**, 2706 (1994)

[11] S. Mitsuda, K. Hosoya, T. Wada, H. Yoshizawa, T. Kanawa, M. Ishikawa, K. Miyatani, K. Saito, K. Kohn, *J. Phys. Soc. J.*, **63**, 3568 (1994)

[12] C. Heid, H. Weitzel, P. Burlet, M. Bonnet, W. Gonschorek, T. Vogt, J. Norwig, H. Fuess, *J. Mag. Mag. Mat.*, **151**, 123 (1995)

[13] C. Heid, H. Weitzel, P. Burlet, M. Winkelmann, H. Ehrenberg, H. Fuess, *Physica B*, **234**, 547 (1997)

[14] S. Kobayashi, S. Mitsuda, M. Ishikawa, K. Miyatani, K. Kohn, *Phys. Rev. B,* **60**, 3331 (1999)

[15] S. Kobayashi, S. Mitsuda, T. Jogetsu, J. Miyamoto, H. Katagiri, K. Kohn, *Phys. Rev. B,* **60**, R9908 (1999)

[16] H. Weitzel, H. Ehrenberg, C. Heid, H. Fuess, P. Burlet, *Phys. Rev. B,* **62**, 12146 (2000)

[17] S. Kobayashi, S. Mitsuda, K. Prokes, *Phys. Rev. B*, **63**, 024415 (2000)

[18] H.K. Müeller-Buschbaum, M. Kobel, *Zeit. A. A. Chem.*, **596**, 23 (1991)

[19] B. Jaspertonnies, H.K. Müeller-Buschbaum, *Zeit. A. A. Chem.*, **508**, 7 (1984)

[20] H.K. Müeller-Buschbaum, M. Kobel, *J. Alloy. Compounds*, **176**, 39 (1991)

[21] A.N. Vasil'ev, L.A. Ponomarenko, A.I. Smirnov, E.V. Antipov, Y.A. Velikodny, M. Isobe, Y. Ueda, *Phys. Rev. B*, **60**, 3021, (1999)

[22] A.N. Vasil'ev, L.A. Ponomarenko, E.V. Antipov, Y.A. Velikodny, A.I. Smirnov, M. Isobe, Y. Ueda, *Physica B,* **284**, 1615, (2000)

[23] J. Kikuchi, K. Ishiguchi, K. Motoya, M. Itoh, K. Inari, N. Eguchi, J. Akimitsu, *J. Phys. Soc. Japan*, **69**, 2660, (2000)

[24] H.-J. Koo, M.-H. Whangbo, *J. Solid State Chem.*, **156**, 110, (2001)

[25] A.V. Prokofiev, R.K. Kremer, W. Assmus, *J. Cryst. Growth*, **231**, 498, (2001)

[26] M. Belaïche, M. Bakhache, M. Drillon, A. Derory, *Chem. Phys. Lett*, **394**, 147, (2004)

[27] K. Mocala J. Ziolkowski, *J. Solid State CHem.*, **69**, 299 (1987)

[28] M. Gondrand, A. Collomb, J.C. Joubert, R.D. Shannon, *J. Solid State Chem.*, **11**, 1 (1974)

[29] L.W. Finger, D.E. Cox, A.P. Jephcoat, *J. Appl. Crys*, **27**, 892, (1994)

[30] H. Stanley, *Introduction to Phase Transitions and Critical Phenomena*, OUP, Oxford (1971)

[31] R.K. Li, C. Greaves, *Phys. Rev. B,* **68**, 172403, (2003)

[32] J. B. Goodenough, *Phys. Rev, **117**, 1442, (1960)*

[33] J. B. Goodenough, *Magnetism and the Chemical Bond* (Interscience, New York, 1963)

[34] S. Kobayashi, S. Mitsuda, K. Hosoya, H. Yoshizawa, T. Hanawa, M. Ishikawa, K. Miyatani, K. Saito, K. Kohn, *Physica B,* **213**, 176, (1995)

[35] F. A. Cotton, G. WIlkinson, *Advanced Inorganic Chemistry*, 6th Edition, John Wiley & Sons, New York (1999)

[36] A.S. Erickson, S. Misra, G.J. Miller, R.R. Gupta, Z. Schlesinger, W.A. Harrison, J.M. Kim, I.R. Fisher, *Phys. Rev. Lett.*, **99**, 016404 (2007)

[37] Luis Ortega-San Martin, Jon P. Chapman, Luis Lezama, Jorge Sánchez-Marcos, Jesús Rodríguez-Fernández, Maria Isabel Arriortua and Teófilo Rojo, *J. Mat. Chem.*, **15**, 183 (2005)

[38] A. Arrot, J.E. Noakes, *Phys. Rev. Lett.*, **19**, 786 (1967)

[39] S.A.J. Kimber, J.P. Attfield, *Phys. Rev. B,* **75**, 064406 (2007)

[40] A. Narath, *Phys. Lett.*, **13**, 12 (1964)

[41] A. Narath, *Phys. Rev.,* **139**, A1221 (1965)

[42] L. Onsager, *Phys. Rev.,* **65**, 117 (1944)

[43] L.J. de Jongh, A.R. Miedema, *Advances in Physics*, **23**, 1 (1974)

[44] L.J. de Jongh (ed), *Magnetic Properties of Layered Transition Metal Compounds*, 1st Edition, Kluwer Academic Publishers, Dordrecht (1990)

[45] K. Yamada, J. Kanamori, *Prog. Theor. Phys. Osaka*, **38**, 541 (1967)

[46] W. Schneider, H. Weitzel, *S. State Comm.*, **13**, 303 (1973)

[47] H. Weitzel, W. Schneider, *S. State Comm.*, **14**, 1025 (1974)

[48] W. Schneider, H. Weitzel, *Acta Cryst. A*, **32**, 32 (1976)

[49] E. Stryjewski, N. Giordano, *Advances in Physics*, **26**, 487 (1977)

[50] A. Narath, *Phys. Rev.*, **136**, A766 (1964)

[51] D.E. Cox, B.C. Frazer, G. Shirane, *Phys. Lett.*, **17**, 103 (1965)

[52] K. Takeda, S-I. Matsukawa, T. Haseda, *J. Phys. Soc. J.*, **30**, 1330 (1971)

[53] J. Hirte, H. Weitzel, N. Lehner, *Phys. Rev. B.*, **30**, 6707 (1984)

[54] P.K. Baltzer, P.J. Wojtowicz, M. Robbins, E. Lopatin, *Phys. Rev.*, **151**, 367 (1966)

Chapter 5

Orbital Order Induced Metal-Insulator Transition in $PbRuO_3$

5.1. Introduction

On moving from the first row transition row metals to the second or third row, the spatial extent of the valence d-orbitals increases dramatically. This increase has well known consequences for oxide materials. For example, second or third row transition metal cations are nearly always low spin. In addition, spin orbit interactions are also much more important for the heavier transition metals, which typically shows a highly reduced moment. In the first row transition metal oxides, some of the most interesting and important phenomena occur in compounds of cations with orbital degrees of freedom, as exemplified by the CMR manganite, in which Jahn-Teller effects are important. Unfortunately, in the 4 or 5d metals, orbital degeneracy is rarely lifted by distortions, perhaps because hardly any 4 or 5d cations with degenerate e_g levels, where the Jahn-Teller effect is strongest, are found. Any examples of 4 or 5d cations with active orbital degrees of freedom are therefore of considerable interest.

The best characterised displays of orbital order in the 4 or 5d block are the non-perovskite oxides, $La_4Ru_2O_{10}$ [1] and $Tl_2Ru_2O_7$ [2]. In both these materials, resistive transitions and lattice distortions occur, accompanied by changes in the Ru – O bond lengths of ca. 5 %. Unfortunately, from the point of view of model orbital ordered systems, the magnetic properties of these materials are complex. In $Tl_2Ru_2O_7$, orbitally ordered zig-zag chains are claimed to form a gapped Haldane chain, $La_4Ru_2O_{10}$ also has a spin gap, probably due to a complex dimerisation mechanism [3]. Orbital order in the layered perovskite Ca_2RuO_4 has also been predicted theoretically [4,5] and observed by resonant X-ray diffraction[6]. However, no symmetry breaking transition occurs and only partial orbital

ordering occurs. Given the scarcity of suitable 4 or 5d materials and the complexities inherent in the known examples, orbital ordering in a simple 4 or 5d perovskite is very attractive. The magnetic and transport properties of the ruthenate perovskites $SrRuO_3$ and $CaRuO_3$ have been well known for decades, both are metallic and $SrRuO_3$ is a rare example of a ferromagnetic perovskite [7]. A single synthesis at high pressures and temperatures of the orthorhombic perovskite $PbRuO_3$ was also reported in 1970, but no structural details or physical properties have subsequently been published [8].

We have prepared $PbRuO_3$ by high pressure/temperature synthesis and characterised this material by magnetisation, transport and synchrotron powder X-ray diffraction measurements. Our measurements show strong evidence for full orbital ordering and an associated metal-insulator transition.

5.2. Experimental

As reported previously in ref. [8], the oxygen deficient pyrochlore $Pb_2Ru_2O_{6.5}$ was used as the precursor for the high pressure reaction. The precursor was prepared by heating PbO and RuO_2 in air at 900 °C for two days with one intermediate regrind. The purity of the precursor was checked by powder X-ray diffraction using a Bruker D8-Advance. The powder diffraction profile of the precursor was well fitted by the published structural model[9] (Fig. 5.1) with $\boldsymbol{a}$ = 10.2521(1) ρ = 8.883(2) g/cm^3.

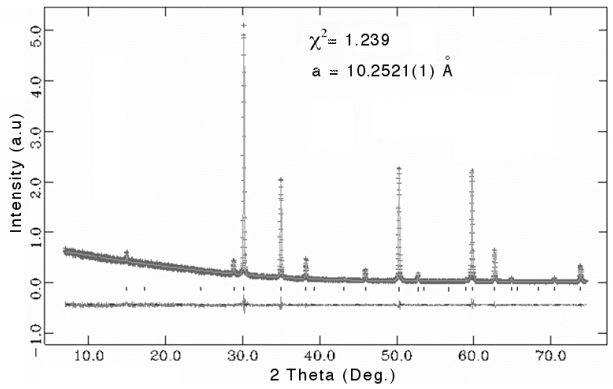

Figure 5.1: Observed, calculated and difference plots for Rietveld fit to laboratory X-ray diffraction profile of $Pb_2Ru_2O_{6.5}$

A large number of attempts were made to synthesise $PbRuO_3$ at high pressure/temperature using the conditions described in Ref [8] and the Walker module described in the introduction. Two samples were ultimately prepared. 'sample 1' was synthesised at 10 GPa and 1000 °C, 'sample 2' was synthesised at 11 GPa and 1000 °C. Both were shown to contain a perovskite like phase by laboratory X-ray powder diffraction. Magnetisation measurements were performed using a Quantum Design SQUID magnetometer in zero and field (200 Oe) conditions. A Quantum Design PPMS system was used for transport measurements. Synchrotron powder X-ray diffraction profiles were recorded for both samples as a function of temperature using instrument ID31 at the ESRF.

5.3. Results

5.3.1. Physical Properties

As high pressure samples are generally not produced in shapes amenable to four probe resistance measurements, the van der Pauw method was used. The resistance of a small disc of sample 1 was measured on cooling. The low resistivity at 230 K (0.35 Ωcm^{-1}) and the almost flat temperature dependence at high temperature (Fig. 5.2) suggest metallic type conductivity. A small increase in the resistivity is seen at 120 K, and at ~85 K the resistance jumps by 4 orders of magnitude, and becomes immeasurably large below 60 K.

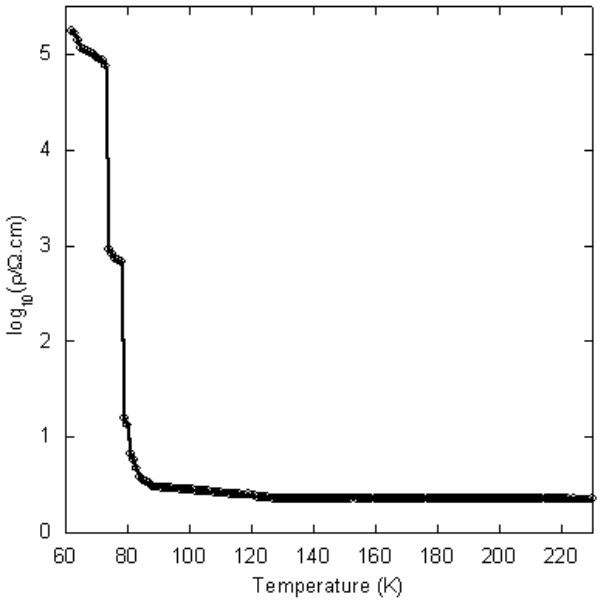

Figure 5.2: Log resistivity vs. Temperature for $PbRuO_3$ (sample 1).

The measured magnetic susceptibility of $PbRuO_3$ is shown in Fig. 5.3. A divergence between the field and zero field cooled susceptiblities is seen below ~ 90 K. A small Curie-Weiss term plus a constant were fitted to the susceptibility at high temperature and subtracted, giving the data shown in the inset to Fig. 5.3 which confirm a magnetic transition at ~ 90 K.

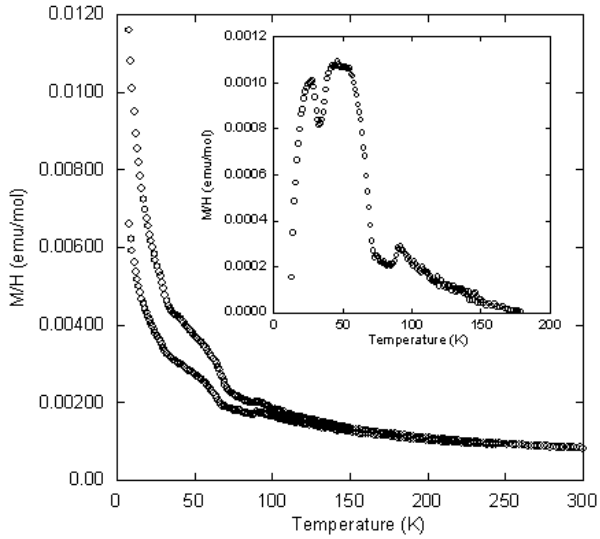

Figure 5.3: Magnetic susceptibilities of $PbRuO_3$ measured in a 200 Oe field.

5.3.2. Synchrotron X-ray diffraction: Sample 1

Synchrotron powder X-ray diffraction data were collected using a capillary sample over the range $2 < 2\Theta < 45$ ° with $\lambda = 0.45621$ Å. Data were collected at 10 K for 3 hours and 1 hour data sets were also collected at 25, 50, 75, 100, 125, 150, 200 and 300 K. The room temperature X-ray diffraction profile of $PbRuO_3$ showed peak splittings characteristic of an orthorhombic perovskite with a $\sqrt{2}a$ x $2a$ x $\sqrt{2}a$ superstructure. Superlattice reflections corresponding to both in and out of phase octahedral tilting ($a^- b^+ a^-$ in Glazer notation [10]) were observed and a Rietveld refinement in space group *Pnma* quickly converged. The peak shape was fitted with a pseudo-Voigt function with a correction for axial divergence and the background was fitted with a linear interpolation function. The diffraction profile is shown in Fig. 5.4, the refinement converged with ${}_wR_p = 0.1586$, $R_p = 0.1251$ and $R(F^2) = 0.0514$ and $\boldsymbol{a} = 5.5628(1)$, $\boldsymbol{b} = 7.86425(1)$ and $\boldsymbol{c} = 5.61403(1)$. The calculated density is $\rho = 9.635(1)$ g/cm^3 (i.e. a ~8.5 % increase).

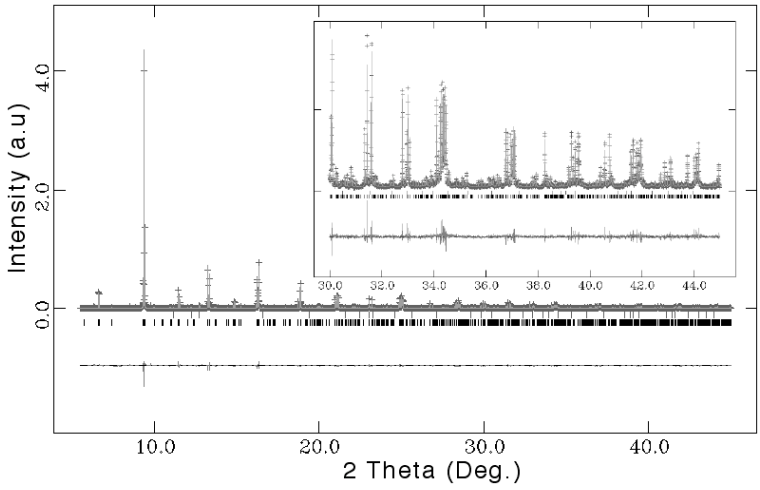

Figure 5.4: Observed, calculated and difference plots for Rietveld fit to 300 K synchrotron powder X-ray diffraction profile of Pnma $PbRuO_3$

Examination of all the data sets showed that a first order structural phase transition occurs at 75 K. Discontinuous changes in peak positions and phase coexistence were observed (Fig. 5.5).

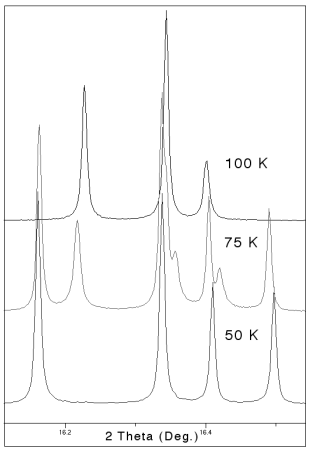

Figure 5.5 Selected area of synchrotron powder diffraction profile of $PbRuO_3$ showing phase transition from Pnma (top) to Imma (bottom) and phase coexistence (middle)

Unusually, the superlattice peaks corresponding to out of phase tilting disappear below 75 K. The systematic absence (h + k + l = 2n) implies a centred cell and the diffraction profile of $PbRuO_3$ could be well fitted by a model in space group *Imma* ($a^0\ b^-\ b^-$). At 75 K, phase co-existence was observed with 55 % *Pnma* and 45 % *Imma* phases by weight. The observed, calculated and difference profiles for the Rietveld fit to the 10 K data set are shown in Fig. 5.6. Details of refined lattice parameters, goodness of fit factors and atomic coordinates for all the refinements are shown in Tables I-IV.

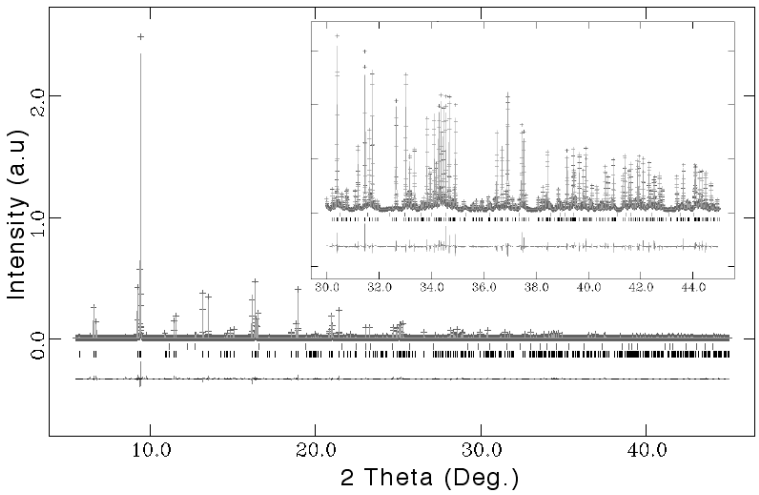

Figure 5.6: Observed, calculated and difference plots for Rietveld fit to 10 K synchrotron powder X-ray diffraction profile of Imma $PbRuO_3$

Table I: Refined lattice parameters and goodness of fit factors for Rietveld fits in *Pnma* phase of $PbRuO_3$

	75 K	100 K	125 K	150 K	200 K	300 K
a (Å)	5.56138(2)	5.55952(1)	5.55897(1)	5.55893(1)	5.55963(1)	5.56284(1)
b (Å)	7.80733(2)	7.82254(1)	7.83168(1)	7.83884(1)	7.84977(1)	7.86425(1)
c (Å)	5.62647(1)	5.61936(1)	5.61624(1)	5.61454(1)	5.61313(1)	5.61403(1)
V (Å^3)	244.299(1)	244.384(1)	244.509(1)	244.657(1)	244.967(1)	245.600(1)
χ^2	5.34	2.78	2.436	3.13	3.058	9.2
$_wR_p$	0.1394	0.1551	0.1496	0.1287	0.1443	0.1586
R_p	0.1046	0.1160	0.1104	0.1119	0.1137	0.1251
$R(F^2)$	0.0445	0.0444	0.0404	0.0360	0.0443	0.0514

Table II: Refined lattice parameters and goodness of fit factors for Rietveld fits in *Imma* phase of $PbRuO_3$

	10 K	25 K	50 K	75 K
a (Å)	5.569737(5)	5.569817(5)	5.569877(6)	5.56972(1)
b (Å)	7.745090(6)	7.745763(7)	7.74823(1)	7.75300(1)
c (Å)	5.662438(5)	5.662266(6)	5.66149(1)	5.65999(1)
V (Å^3)	244.267(1)	244.284(1)	244.331(1)	244.410(1)
χ^2	13.11	2.91	4.116	5.34
$_wR_p$	0.1257	0.1483	0.1470	0.1394
R_p	0.0953	0.1080	0.1112	0.1046
$R(F^2)$	0.0371	0.0389	0.0418	0.0445

Table III: Refined atomic coordinates and displacement parameters ($Å^2$ x 10^2) for $PbRuO_3$ in *Pnma* phase. Atomic positions are Pb:*x*, 1/4, *z*; Ru 0, 0, 1/2; O(1) *x*, 1/4, *z*; O(2) *x*, *y*, *z*. Wyckoff sites are: Pb (*4c*), Ru (*4b*), O1 (*4c*), O2 (*8d*).

	75 K	100 K	125 K	150 K	200 K	300 K
Pb: *x*	0.0137(1)	0.0144(1)	0.0146(1)	0.0145(1)	0.0139(1)	0.0125(1)
Pb: *z*	0.9918(1)	0.9927(1)	0.9932(1)	0.9938(1)	0.9945(1)	0.996(1)
Pb: Uiso	0.09(1)	0.32(1)	0.39(1)	0.46(1)	0.62(1)	0.94(1)
Ru: Uiso	0.0(1)	0.1(1)	0.13(1)	0.15(1)	0.20(1)	0.35(1)
O(1): *x*	0.500(3)	0.500(1)	0.500(1)	0.50(1)	0.50(1)	0.50(1)
O(1): *z*	0.073(2)	0.068(1)	0.067(1)	0.068(1)	0.065(1)	0.063(1)
O(2): *x*	0.267(3)	0.273(1)	0.275(1)	0.276(1)	0.279(1)	0.275(1)
O(2): *y*	0.042(1)	0.039(1)	0.039(1)	0.039(1)	0.036(1)	0.036(1)
O(2): *z*	0.729(2)	0.728(1)	0.726(1)	0.724(1)	0.72(1)	0.722(1)
O: Uiso	0.17(16)	0.5(1)	0.6(1)	0.7(1)	0.7(1)	1.0(1)

Table III: Refined atomic coordinates and displacement parameters ($Å^2$ x 10^2) for $PbRuO_3$ in *Imma* phase. Atomic positions are Pb:0, 1/4, *z*; Ru 0, 0, 1/2; O(1) 1/2, 1/4, *z*; O(2) 1/4, *y*, 3/4. Wyckoff sites are: Pb (*4e*), Ru (*4a*), O1 (*4e*), O2 (*8g*).

	10 K	25 K	50 K	75 K
Pb: *z*	0.01332(4)	0.01331(5)	0.0132(1)	0.0128(1)
Pb: Uiso	0.095(5)	0.113(5)	0.16(1)	0.28(1)
Ru: Uiso	0.02(1)	0.03(1)	0.03(1)	0.13(1)
O(1): *z*	-0.069(1)	-0.070(1)	-0.070(1)	-0.070(1)
O(2): *y*	-0.0462(4)	-0.0457(5)	-0.045(1)	-0.045(1)
O: Uiso	0.30(5)	0.4(1)	0.5(1)	0.7(1)

The temperature evolution of the normalised lattice parameters is shown in Fig. 5.7. A clear expansion along ***c*** and contraction of ***b*** are seen on cooling through 75 K. The refined cell volume, Fig. 5.8, shows an anomaly at 75 K, but overall normal thermal contraction.

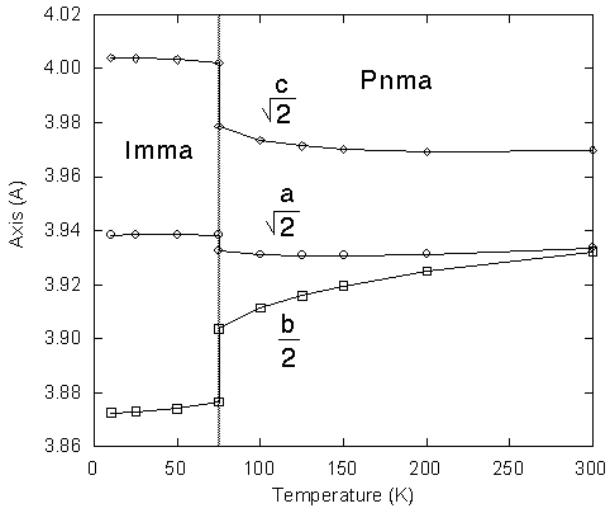

Figure 5.7: Temperature evolution of refined lattice parameters of $PbRuO_3$ (sample 1)

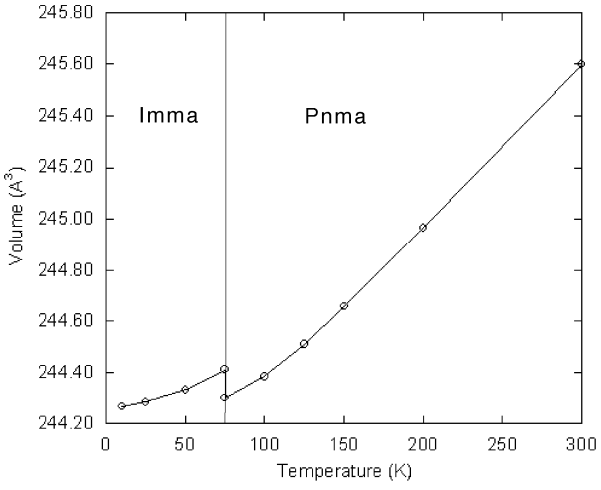

Figure 5.8: Temperature evolution of refined cell volume of $PbRuO_3$ (sample 1)

The refined Ru – O bond distances and Ru – O - Ru angles shown in Figures 5.9 and 5.10 are also strongly discontinous at the 75 K transition. Below 75 K the bond distances split into four long bonds in the *xz* plane and two short bonds along *z*. The Ru – O (1) – Ru bond angle, which lies along *z* also becomes more distorted, while the Ru- O(2) – Ru bond angle (*xz* plane) becomes more regular. These changes are strongly indicative of an orbital ordering with preferential occupation of the Ru^{4+} d_{xz} orbital.

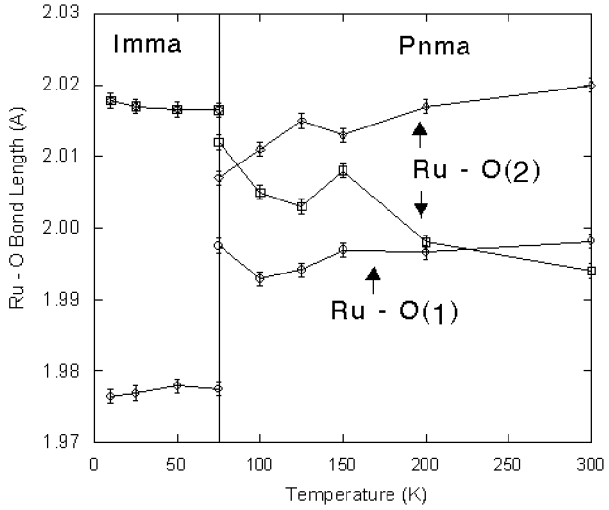

Figure 5.9: Temperature evolution of refined Ru – O bond lengths in $PbRuO_3$ (sample 1).

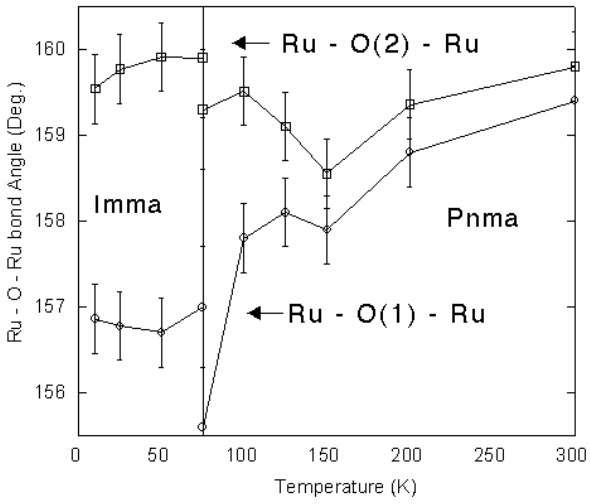

Figure 5.10: Temperature evolution of refined Ru – O - Ru bond angles in $PbRuO_3$ (sample 1).

The distortion of the RuO_6 octahedra may be further expressed (Fig. 5.11) using the distortion parameter[11] Δd, where d_n is the average bond length:

$$\Delta d = \frac{1}{6}\sum[(d_n - d)d^2] \tag{5.1}$$

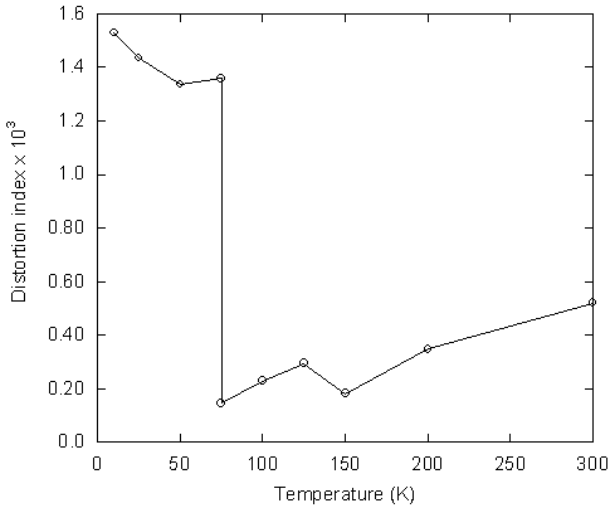

Figure 5.11: Temperature dependence of octahedral distortion parameter in $PbRuO_3$

At 300 K, the distortion parameter is small, 5.2 x 10^{-4}, and similar to that calculated for $SrRuO_3$ at room temperature (1.8 x 10^{-4}) [14]. However at 10 K, the RuO_6 octahedra are strongly tetragonally distorted and Δd = 15.3 x 10^{-4}.

The structural change at 75 K is also accompanied by a subtle change in the direction of the Pb^{2+} displacements. At room temperature, the Pb^{2+} cation is displaced from the centre of the coordinating oxygens by 0.069 Å along ***a*** and 0.024 Å along ***c***. This corresponds to a [101] displacement in the cubic perovskite cell. On cooling through 75 K, the displacement along ***a*** disappears and at 10 K the Pb^{2+} cation is displaced 0.075 Å along ***c*** (a [001] displacement in the cubic cell). The overall Pb^{2+} displacement shows a peak at ~ 125 K (Fig. 5.12), and hence may induce the structural transition at 75 K.

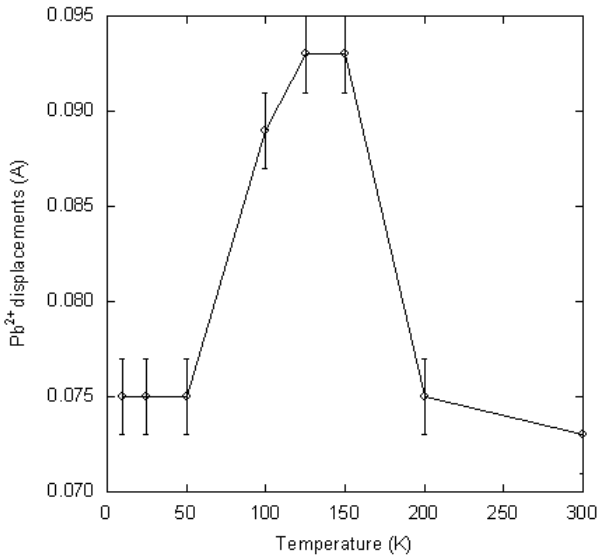

Figure 5.12: Displacements of Pb^{2+} from centre of coordinating oxygens in $PbRuO_3$ as a function of temperature.

5.3.3. Time Evolution of Phase Transformation at 75 K

When data were collected for sample 1 at 75 K, it was noticed that the diffraction profile was changing as a function of time as the phase transition from *Imma* to *Pnma* progressed. Therefore, data were collected at 75 K using 20 min scans until no further changes in the diffraction pattern occurred. The time evolution of the refined phase fraction at 75 K is shown in Fig. 5.13. After 2 hours, the phase fraction of *Pnma* $PbRuO_3$ saturates at just over 50 %. The time evolution of the normalised phase fraction could be fitted to an Avrami kinetics law[12]:

$$f(x) = 1 - \exp[-kt^n] \tag{5.2}$$

where k is the rate of transformation and n is the Avrami exponent. The fit gave k = 0.02(1) min^{-1} and n = 1.1(1).

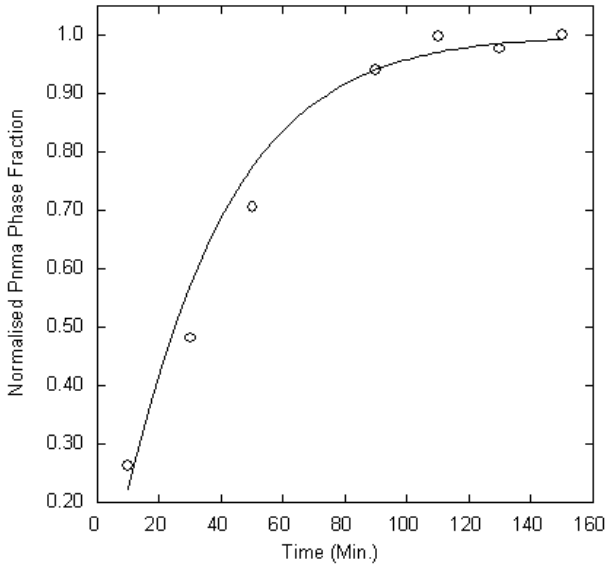

Figure 5.13: Time evolution of Pnma phase fraction at 75 K. Line is fit to Eqn. (5.2)

As the phase transition in $PbRuO_3$ is discontinuous, significant structural changes are expected to occur as a function of time. The time evolution of the normalised lattice parameters of the *Imma* fraction is shown in Figures 5.14 – 5.16 The largest change is seen in the ***b*** axis, which expands, as expected from the lattice parameters plotted in Fig. 5.15.

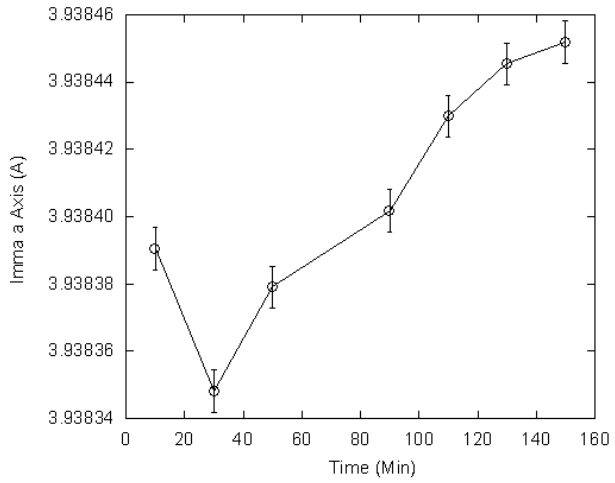

Figure 5.14: Time evolution of normalised (a/√2) Imma ***a*** axis at 75 K

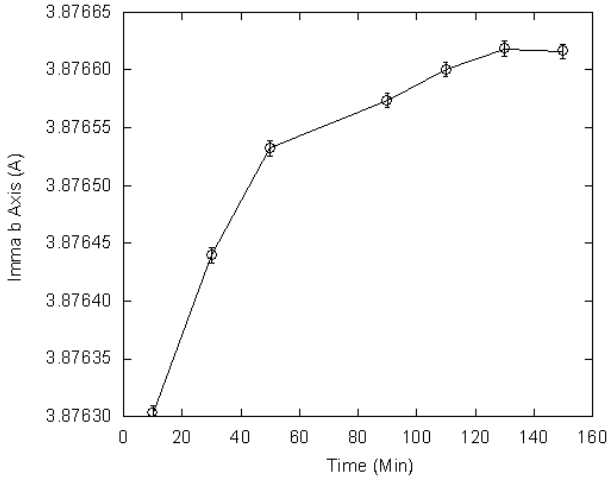

Figure 5.15: Time evolution of normalised (b/2) Imma ***b*** axis at 75 K

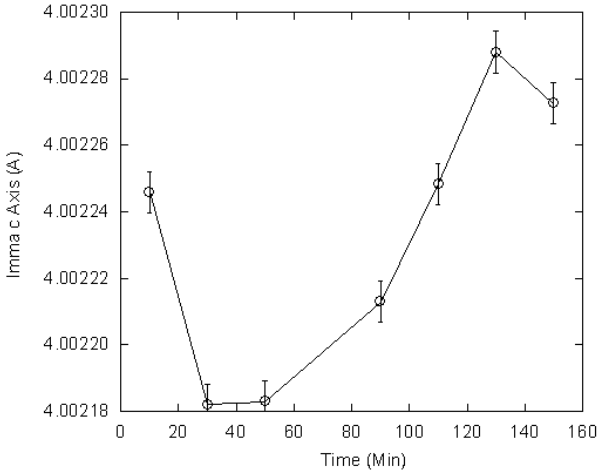

Figure 5.16: Time evolution of normalised (c/√2) Imma ***c*** axis at 75 K

The largest changes in the normalised lattice parameters of the *Pnma* phase fraction are an expansion of the ***b*** axis and a contraction of ***c,*** as shown in Figures 5.17 – 5.19.

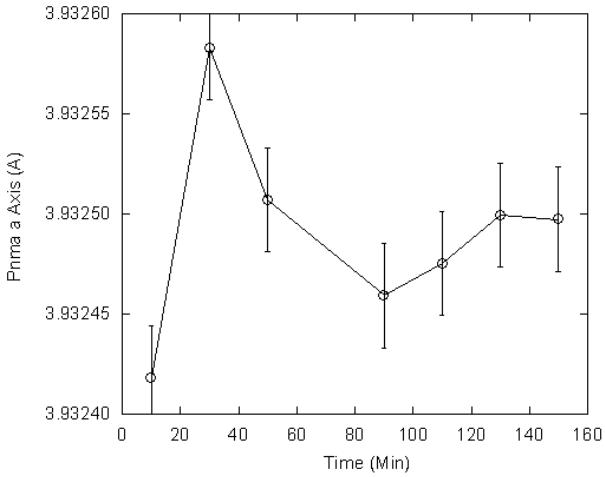

Figure 5.17: Time evolution of normalised (a/√2) Pnma ***a*** axis at 75 K

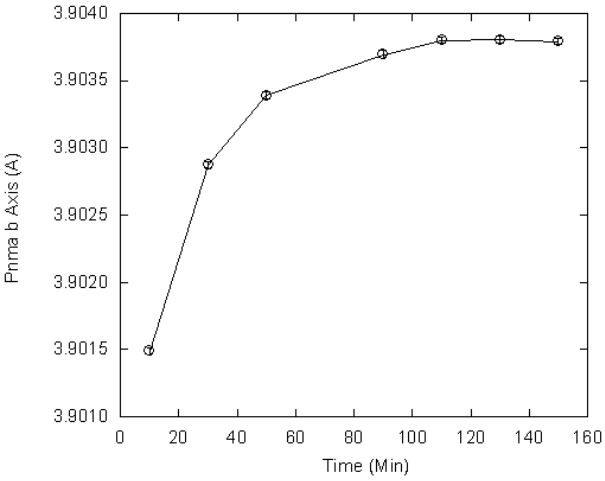

Figure 5.18: Time evolution of normalised (b/2) Pnma ***b*** axis at 75 K

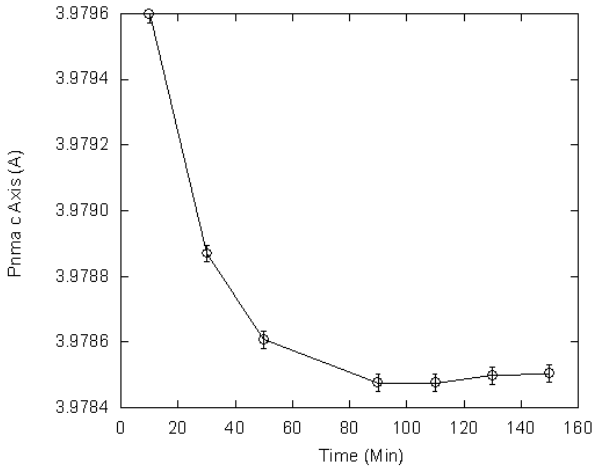

Figure 5.19: Time evolution of normalised (c/√2) Pnma ***c*** axis at 75 K

The lattice microstrain was calculated from the Lorentzian broadening ($\Gamma = Y\tan\Theta$) of both phases as a function of time at 75 K. The instrumental contribution (0.036 %) was calculated from a silicon standard and subtracted off. As shown in Fig. 5.20, the emerging *Pnma* phase fraction is highly strained, whereas the *Imma* lattice strains are much smaller and almost time independent.

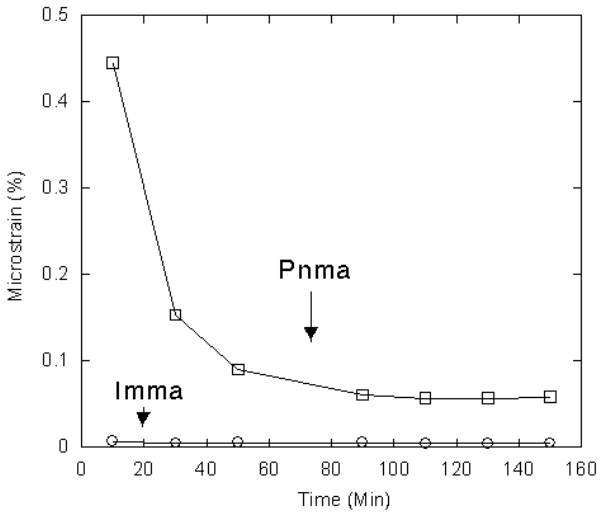

Figure 5.20: Lattice microstrain (%) of *Pnma* and *Imma* phase fractions at 75 K as a function of time

5.3.4. Synchrotron Powder X-ray Diffraction: Sample 2

For this sample, data were collected whilst cooling at 2 K/min to 10 K and on heating back up to 150 K also at 2 K/min. The refined lattice parameters are shown as a function of temperature in Fig. 5.21. Significant hysteresis (ca. 20 K) is seen at the 75 K *Imma-Pnma* phase transition.

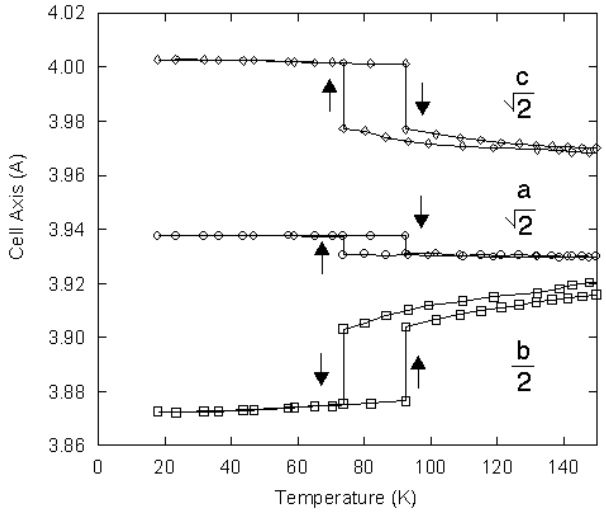

Figure 5.21: Refined lattice parameters from cooling and heating runs on $PbRuO_3$, sample 2

The base temperature achieved in this experiment was 9.7 K. Close inspection of the diffraction profiles revealed that this sample had undergone a further phase transition at 9.8 K. Selected diffraction patterns from the cooling run are shown in Fig. 5.22, importantly, complete transformation from *Pnma* to *Imma* is observed on cooling, prior to the new transition.

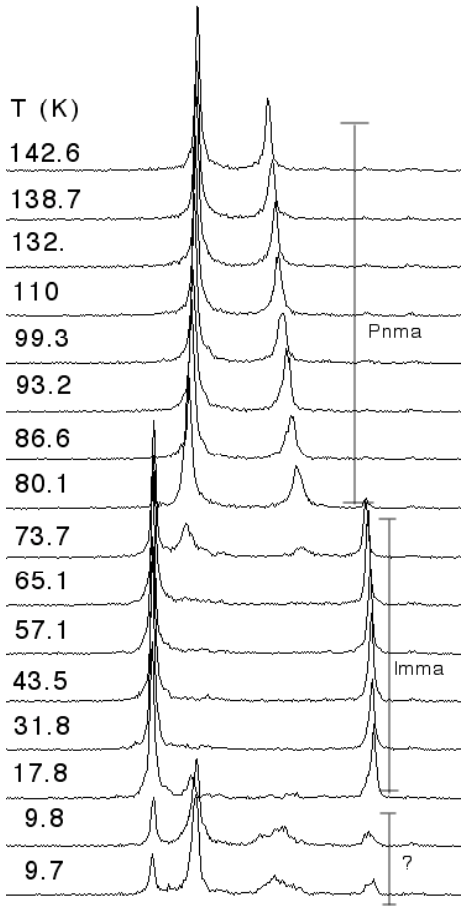

Figure 5.22: Peak splitting at pseudo-cubic (211) position of $PbRuO_3$ (sample 2), data collected on cooling.

The (020) and (040) reflections from the new phase are extremely broad, which may indicate an increase in the cell size, initial anaysis also suggests a monoclinic distortion. Unfortunately, the quality of the data recorded and phase coexistence prevented structural determination.

5.4. Discussion

At room temperature, the *Pnma* structure of $PbRuO_3$ is similar to that seen in $SrRuO_3$ [13] with the addition of antiferroelectric Pb^{2+} displacements. Comparison of the room temperature Ru – O – Ru bond angles in $PbRuO_3$ (159.5, 159.8 °) with those in $SrRuO_3$ (162.7,

162.8 °) shows the structure is also more distorted. The structure of $PbRuO_3$ at room temperature is shown in Fig. 5.23.

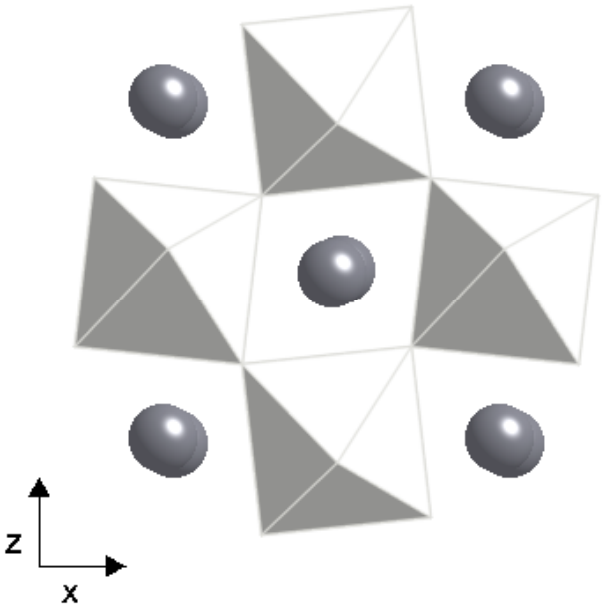

Figure 5.23: *Pnma* structure of $PbRuO_3$ at 300 K projected down [010].

The above results show that $PbRuO_3$ undergoes a transition to an orbitally ordered *Imma* phase at ~ 75 K with an associated metal-insulator transition. The refined bond lengths (Fig. 5.9) show that below 75 K, the Ru^{4+} d_{xz} orbital is preferentially occupied, leading to an expansion of the ***c*** axis and a contraction along ***b***. The octahedral distortion parameter at 10 K (15.3×10^{-4}) is smaller than values observed in first row Jahn-Teller distorted systems such as $LaMnO_3$ ($\Delta d = 33.1 \times 10^{-4}$) or $KCrF_3$ ($\Delta d = 46.2 \times 10^{-4}$) [11,14], but highly significant for a second row transition metal with degenerate t_{2g} orbitals. The *Imma* structure of $PbRuO_3$ is shown in Fig. 5.24.

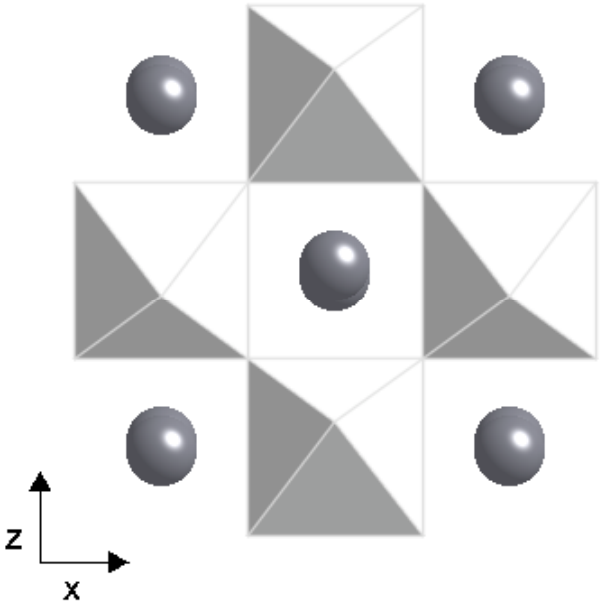

Figure 5.24: *Imma* structure of $PbRuO_3$ at 10 K projected down [010].

Jahn-Teller distortions occur when the energy gained by removing electronic degeneracy is greater than that lost to lattice deformation. Generally, in $ARuO_3$ perovskites with degenerate t_{2g} orbitals this condition is not satisfied. It is therefore plausible that the orbital order transition in $PbRuO_3$ is induced by the peak seen in Pb^{2+} displacements at ~125 K. A small increase in the resistivity is also seen at this temperature, if 125 K is indeed the onset of orbital order, this increase could be due to carrier scattering by localised moments. Signatures of the incomplete orbital ordering in Ca_2RuO_4 are also observed more than 200 K above the transition [15].

Displacive transitions in perovskite oxides usually occur very quickly, and it is rare for a material to reach an equilibrium state as seen in $PbRuO_3$ at 75 K. The sluggish phase transition seen in $PbRuO_3$ is thus extremely unusual and confirms that the *Imma* and *Pnma* phases have very different electron lattice couplings. Very long relaxation times (several hours) are also seen from the field induced ferromagnetic state in the bilayer perovskite $(La,Pr)_{1.2}Sr_{1.8}Mn_2O_7$. The slow kinetics in this material were attributed to competition between double exchange and Jahn-Teller distortions [16]. The unusually slow dynamics in $PbRuO_3$ may therefore originate in the interplay between orbital order and ferroelectric displacements. The time evolution of the *Pnma* phase fraction at 75 K can be fitted by an

Avrami equation with k = 0.02(1) min^{-1} and n = 1.1(1). The Avrami exponent is related to the dimensionality of crystal growth at a phase change., and in $PbRuO_3$, therefore suggests a one dimensional mechanism. Given the large mismatch in ***b*** and ***c*** lattice parameters between *Imma* and *Pnma* phases in $PbRuO_3$, it is not unreasonable to conclude that the phase transition proceeds by nucleation along the ***a*** axis. Our diffraction measurements also show the emerging *Pnma* phase fraction to be highly strained, as expected for epitaxial type growth.

The second phase change seen at 9.8 K in sample 2 is intriguing and will be the subject of future work (see below). The limited data available suggests a lowering of lattice symmetry and an increase in cell size.

5.5. Conclusions

The above results show that $PbRuO_3$ is the first example of a simple perovskite ruthenate to show orbital order and a metal insulator transition. As the related materials $SrRuO_3$ and $CaRuO_3$ do not show orbital order and are metallic, it is proposed that the origin of the orbital order in $PbRuO_3$ may be ferroelectric displacements of Pb^{2+}. The transition from *Pnma* to *Imma* seems to be accompanied by a magnetic transition, although the magnetic groundstate is not clear due to problems inherent in high pressure sample preparation. In particular, the presence of magnetic impurities makes interpreting the suseptibility measurements difficult. Small traces of RuO_2, Ru and $Pb_2Ru_2O_{6.5}$ were detected in the synchrotron X-ray patterns. All of these materials will add a Pauli paramagnetic (temperature independent) contribution to the measured susceptibilty, leading to poor agreement with the Curie-Weiss law. However, it is unclear at this stage if the high temperature *Pnma* phase of $PbRuO_3$ will indeed show Curie-Weiss or Pauli Paramagnetic behaviour. Experiments with additional samples are required to resolve this issue. One other interesting observation from the synchrotron powder X-ray diffraction experiment was the presence of several very weak unidentified peaks, suggesting that there are as-yet undiscovered phases in the Ru – Pb – O ternary system at high pressure and temperature.

5.6. Further Work

More synchrotron diffraction experiments need to be performed on this material in order to solve the low temperature structure and to check if differences in sample quality or preparation conditions are important. As the centricity of the low temperature structure is unknown, dielectric measurements should also be performed. It would also be extremely interesting to follow the phase change between *Imma* and *Pnma* as a function of time using synchrotron diffraction over a range of temperatures. This would allow the calculation of an activation energy for this process.

Collecting powder neutron diffraction data as a function of temperature for $PbRuO_3$ would also be an ideal experiment. In particular, it would help clarify the magnetic properties of $PbRuO_3$. As neutron diffraction is much more sensitive to oxygen displacements in this system, it may also be possible to look for fluctuations in Pb – O or Ru – O bond lengths etc above 75 K.

References

[1] P.G. Khalifah, R. Osborn, Q. Huang, H.W. Zanderbergen, R. Jin, Y. Liu, D. Mandrus, R.J. Cava, *Science*, **297**, 2237 (2002)

[2] S. Lee, J-G. Park, D.T. Adroja, D. Khomskii, S. Streltsov, K.A. McEwen, H. Sakai, K. Yoshimura, V.I. Ansimov, D. Mori, R. Kanno, R. Ibberson, *Nature Materials*, **5**, 471 (2006)

[3] H. Wu, Z. Hu, T. Burnus, J.D. Denlinger, P.G. Khalifah, D. Mandrus, L-Y. Jang, H.H. Hsieh, A. Tanaka, K.S. Liang, J. W. Allen, R.J. Cava, D.I. Khomskii, L.H. Tjeng, *Phys. Rev. Lett.*, **96**, 256402 (2006)

[4] T. Mizokawa, L.H. Tjeng, G.A. Sawatzky, G. Ghiringhelli, O. Tjemberg, N.B. Brookes, H. Fukazawa, S. S. Nakatsuji, Y. Maeno, *Phys. Rev. Lett.*, **87**, 077202 (2001)

[5] T. Hotta, E. Dagotto, *Phys. Rev. Lett.*, **88**, 017201 (2001)

[6] I. Zeginoglou, J. Strempfer, C.S. Nelson, J.P. Hill, J. Chakhalian, C. Bernhard, J.C. Lang, G. Srajer, H. Fukazawa, S. Nakatsuji, Y. Maeno, B. Keimer, *Phys. Rev. Lett*, **95**, 136401 (2005)

[7] J.M. Longo, P.M. Raccah, J.B. Goodenough, *J. Appl. Phys.*, **39**, 1327 (1968)

[8] J.A. Kafalas, J.M. Longo, *Mat. Res. Bull.*, **5**, 193 (1970)

[9] M. Tachibana, Y. Kohama, T. Shimoyama, A. Harada, T. Taniyama, M. Itoh, H. Kawaji, T. Atake, *Phys. Rev. B*, **73**, 193107 (2006)

[10] A.M. Glazer, *Acta Cryst. B*, **28**, 3384 (1972)

[11] M.W. Lufaso, P.M. Woodward, *Acta Cryst. B*, **60**, 10 (2004)

[12] M. Avrami, *J. Chem. Phys.*, **7**, 1103 (1939)

[13] C.W. Jones, P.D. Battle, P. Lightfoot, W.T.A. Harrison, *Acta Cryst. C*, **45**, 365 (1989)

[14] S. Margadonna, G. Karotsis, *J. Mat. Chem.*, **17**, 2013 (2007)

[15] M. Braden, G. Andre, S. Nakatsuji, Y. Maeno, *Phys. Rev. B*, **58**, 847 (1998)

[16] M. Matsukawa, M. Chiba, A. Akasaka, R. Suryanarayanan, M. Apostu, A. Revcolevsch, S. Nimori, N. Kobayashi, *Phys. Rev. B*, **70**, 132402 (2004)

Chapter 6

Structure and Magnetism of Lead Manganese Oxides

6.1. Introduction

Manganese oxides have attracted much attention in recent years, principally due to the wide and varied properties of the manganite perovskite family (CMR, charge order, orbital order, phase separation etc.). The properties of non-perovskite manganese oxides have also been widely studied, including the $REMn_2O_5$ (RE = rare earth) materials, which show anomalous ferroelectricity induced by incommensurate magnetic order [1-4] and the CMR pyrochlore $Tl_2Mn_2O_7$ [5,6]. The aim of this chapter is the characterisation of two low dimensional non-perovskite lead manganese oxides; Pb_2MnO_4, which has a structure consisting of edge sharing chains of MnO_6 octahedra (Fig. 6.1) and $Pb_3Mn_7O_{15}$, which has a structure consisting of 1/2 filled Kagomé layers connected by ribbons of edge sharing MnO_6 octahedra (Fig. 6.2). Pb_2MnO_4 is reported to crystallise in the non-centrosymmetric, non-polar space group P-42_1c, and has been predicted to show piezoelectric properties [7,8]. Assigning the space group of the more complex mixed valence material $Pb_3Mn_7O_{15}$ has proved controversial, and it has variously been reported to be non-centrosymmetric *Cmc*2_1 (Darriet *et al*, 1978) [9], centrosymmetric *Cmcm* (Marsh *et al*, 1983) [10] and *P*6_3/*mcm* (Calvert *et al*, 1984) [11]. The later revisions of the space group for $Pb_3Mn_7O_{15}$ are all based on refinement of the structure factors reported in 1978, no new single crystal preparations have subsequently been reported.

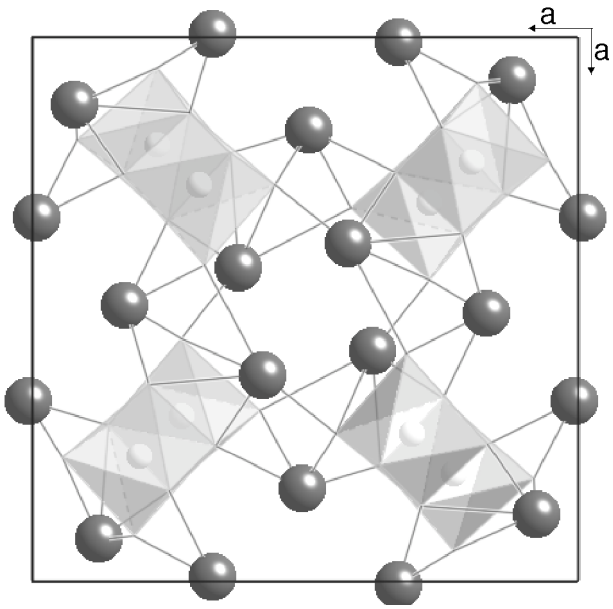

Figure 6.1: Structure of Pb_2MnO_4 projected down [001], light octahedra are MnO_6, dark spheres are Pb^{2+}.

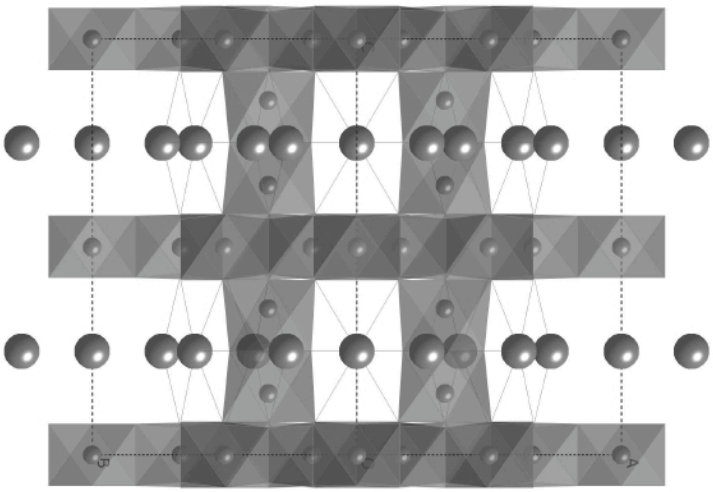

Figure 6.2: Structure of $Pb_3Mn_7O_{15}$ showing 1/2 filled Kagomé lattice connected by ribbons of edge sharing MnO_6 octahedra. Spheres represent Pb^{2+} cations.

This chapter is divided into two sections. The identification of the magnetic point group symmetry of Pb_2MnO_4 and proposed 'multipiezo' behaviour and the effect of oxygen stoichiometry on the structure and magnetic properties of $Pb_3Mn_7O_{15}$.

6.1.1. Experimental

Polycrystalline Pb_2MnO_4 was synthesised from PbO (99.999%, Aldrich) and Mn_2O_3 (99.999%, Aldrich). Stoichiometric quantities of the reagents were intimately ground, pelleted and reacted under air for a total of one week at 730°C with several intermediate regrinds. Phase purity was checked by powder X-ray diffraction. Magnetisation measurements were performed using a Quantum Design SQUID magnetometer under field (1 T) and zero field cooled conditions. Time of flight neutron powder diffraction data were recorded using the instrument OSIRIS at the ISIS facility, UK. A 10g sample of Pb_2MnO_4 was placed in a vanadium can and data were collected at 1.5K for 20 hours.

Polycrystalline $Pb_3Mn_7O_{15}$ was synthesised from PbO (99.999%, Aldrich) and Mn_2O_3 (99.999%, Aldrich). Stoichiometric quantities of the reagents were intimately ground, pelleted and reacted under air for a total of four days at 830 °C with several intermediate regrinds. Single crystals were synthesised by heating the polycrystalline material together with a $PbCl_2$ flux/transport agent in a tube furnace to 830 °C and cooling over the course of several days. The crystals were removed from the flux using dilute acetic acid and consisted of shiny black hexagons. Powder X-ray and neutron diffraction data were collected using ID31 at the ESRF and Super-D2B at the ILL, with wavelengths 0.45621 Å and 1.594 Å respectively. Single crystal intensities were collected by the crystallographic service of the School of Chemistry, University of Edinburgh. Magnetisation measurements were performed using a Quantum Design SQUID magnetometer under field and zero field cooled conditions. A Quantum Design PPMS system was used for heat capacity and M(H) measurements. The General Structure Analysis System (GSAS) was used to fit the powder diffraction profiles.

6.2. Magnetic Point Group Symmetry and Proposed 'Multipiezo' Behaviour in Pb_2MnO_4

6.2.1. Magnetisation Results

The magnetic susceptibility and inverse susceptibility measurements shown in Figure 6.3 reveal a sharp transition to a three-dimensionally ordered antiferromagnetic state below T_N = 18 K. The inverse susceptibility follows a Curie-Weiss law with an observed paramagnetic moment of 3.8(1) μ_B, in excellent agreement with the predicted spin-only moment for Mn^{4+} (3.87 μ_B). The Weiss constant is negative (-42(1) K) indicating dominant antiferromagnetic interactions between Mn^{4+} spins. No divergence between field and zero-field cooled measurements was observed, confirming that the ground state is antiferromagnetic with no spontaneous magnetisation.

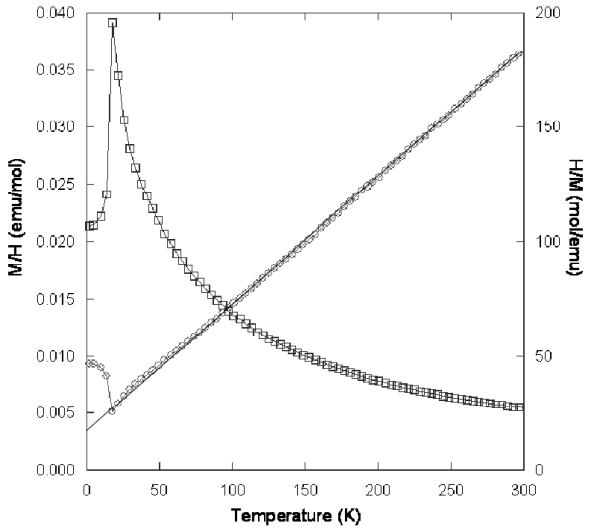

Figure 6.3: Magnetic susceptibility and inverse susceptibility of Pb_2MnO_4 as a function of temperature. The line shows a Curie-Weiss fit in the range 100-300 K, extrapolated to low temperature.

6.2.2. Neutron Powder Diffraction Results

No distortion from tetragonal symmetry was apparent in the 1.5 K neutron data (Fig. 6.4), so these were fitted using the previously reported room temperature structural model in space group $P\bar{4}2_1c$. The diffraction peak shape was modelled with a convolution of an Ikeda-Carpenter and a pseudo-Voigt function [12] and the background was fitted by a linear interpolation function. After fitting the contributions from the crystal structure, several peaks at high d- spacing showed extra intensities and three additional weak peaks were also evident (see Figs. 4b and c), at d = 3.39, 4.46 and 12.78 Å, corresponding respectively to the (221), (111) and (100) reflections. These are systematically absent from the $P\bar{4}2_1c$ space group. No other magnetic peaks were seen, so several possible antiferromagnetic models were constructed with a (000) propagation vector. The possible Shubnikov groups are: $P\bar{4}2_1c$, $P\bar{4}'2'_1c$, $P\bar{4}'2_1c'$ and $P\bar{4}2'_1c'$ (where the primed symbols have a time reversal symmetry operation) and only those having the $\bar{4}'$ operation generate the above weak peaks that are systematically absent in the parent group symmetry. Only models having Shubnikov group symmetry $P\bar{4}'2_1c'$ gave a good fit to the intensities. The Mn^{4+} moments are oriented in [110] or [$\bar{1}$10 directions and are parallel to the ***ab***-plane, as shown in Fig. 6.1. The final fit of the crystal and magnetic structures to the 1.5 K neutron data gave residuals R_p = 3.49% and wR_p = 3.51% and the results in Tables 1 and 2. The structuralparameters are in agreement with those previously reported for tetragonal Pb_2MnO_4 at 300 K, but are more precise. The refined moment of 2.74(2) μ_B shows a typical reduction from the ideal value of 3 μ_B for Mn^{4+} due to covalency effects

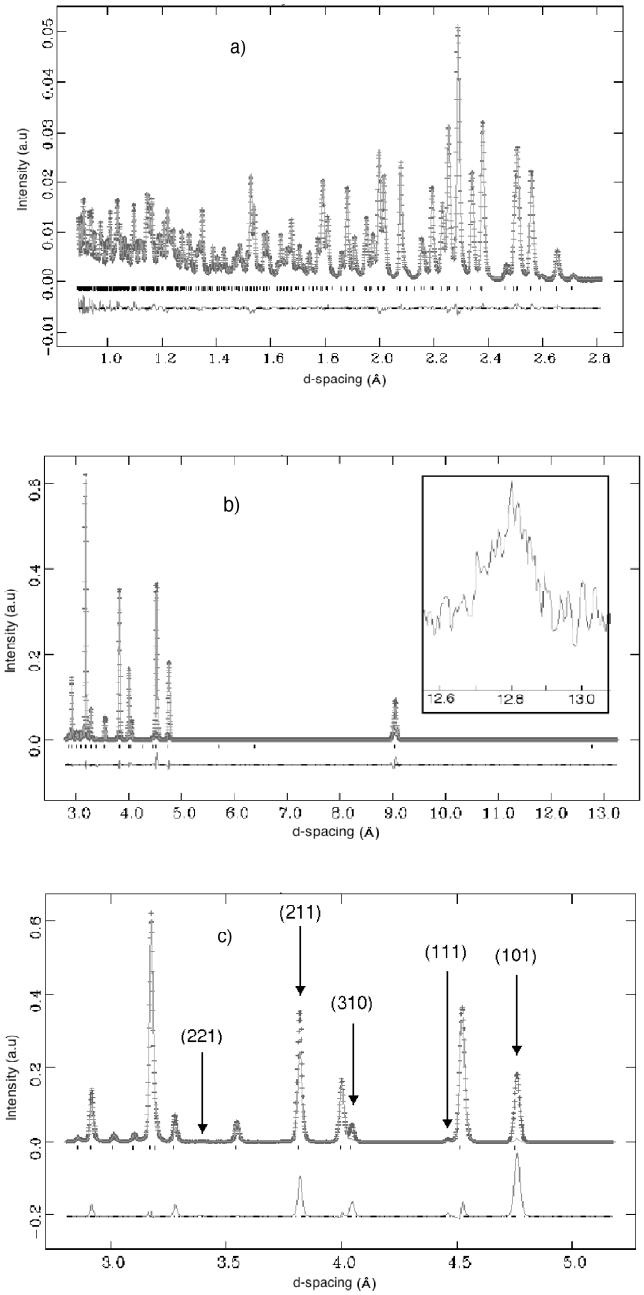

Figure 6.4: Observed, calculated and difference Rietveld fits to the 1.5 K time-of-flight neutron diffraction profile of Pb_2MnO_4. (a) and (b) display the final fit of the nuclear and magnetic structures. (c) shows a fit of only the nuclear structure with prominent magnetic peaks labelled; the additional weak (100) magnetic peak is shown in the inset to (b).

Table I: Refined atomic coordinates and isotropic displacement parameters for Pb_2MnO_4 at 1.5 K in space group $P\bar{4}2_1c$. The refined cell parameters are a = 12.78027(10) Å and c = 5.12418(6) Å. Wyckoff sites are: Pb (*8e*), Pb2 (*8e*), Mn1 (*8e*), O1 (*8e*), O2 (*8e*), O3 (*8e*), O4 (*8e*)

Atom	x	y	z	U_{iso} (Å^2)
Pb(1)	0.07798(6)	0.12310(5)	0.2459(2)	0.0044(3)
Pb(2)	0.00754(5)	0.33043(6)	0.7940(1)	0.0027(3)
Mn	0.3072(1)	0.2706(1)	0.2572(5)	0.0014(6)
O(1)	0.3155(1)	0.4143(1)	0.1560(3)	0.0057(5)
O(2)	0.2802(1)	0.1405(1)	0.4355(3)	0.0050(5)
O(3)	0.3252(1)	0.7567(1)	0.4241(2)	0.0018(5)
O(4)	0.2703(1)	0.5581(1)	0.5993(3)	0.0067(5)

Table II: Selected bond distances (Å) and angles (°) for Pb_2MnO_4 at 1.5 K.

Mn – O(1)	1.911(3)
Mn – O(2)	1.928(3)
	1.893(4)
Mn – O(3)	1.955(3)
	1.939(3)
Mn – O(4)	1.871(3)
<Mn – O>	1.916(3)
Mn – O(2) – Mn	99.81(12)
Mn – O(3) – Mn	97.31(11)
Pb(1) – O(1)	2.245(2)
Pb(1) – O(2)	2.770(2)
Pb(1) – O(3)	2.282(2)
Pb(1) – O(4)	2.753(3)
	2.333(2)
<Pb-O(1)>	2.476(2)
Pb(2) – O(1)	2.231(2)
Pb(2) – O(2)	2.319(2)
<Pb – O(2)>	2.372(2)

6.2.3. Discussion

The magnetic structure of Pb_2MnO_4 is illustrated in Fig. 6.5 and consists of antiferromagnetic chains with moments parallel to the ***ab*** plane, coupled antiparallel to those in the nearest neighbour chains. The intrachain Mn-O-Mn angles of 100 and 97° would be expected to lead to ferromagnetic superexchange, but direct Mn-Mn exchange leads to antiferromagnetic interactions. Weaker superexchange interactions via Mn-O-Pb-O-Mn bridges lead to long range spin order. The Mn-Mn distance within the chains is 2.92 Å, whereas the shortest interchain Mn-Mn distance is 5.96 Å, so that some one-dimensional behaviour might be expected. However, the magnetic susceptibility (Fig. 6.3) shows that Pb_2MnO_4 behaves as a three dimensional antiferromagnet with no short range correlations evident above the Neel transition at T_N = 18 K.

The bulk properties of a magnetically ordered material can be predicted from the magnetic point group using Neumann's principle. In the case of Pb_2MnO_4, the point group $-4'2_1c'$ is predicted to allow piezomagnetism (a stress induced ferromagnetic moment). This property is described by the relation $\boldsymbol{M}_i = \boldsymbol{c}_{ij}\boldsymbol{s}_j$, where $\boldsymbol{c}_{ij}$ is the piezomagnetic tensor. Piezomagnetism is less studied than piezoelectricity, but the $\boldsymbol{c}_{ij}$ components have been determined experimentally in crystals of the centrosymmetric fluorides CoF_2 and MnF_2 [13]. The Shubnikov group $P\bar{4}'2_1c'$ has c_{14} and c_{36} as the only non-zero piezomagnetic coefficients, the Mn^{4+} moments of 2.74 μ_B lie parallel to the ***ab***-plane and so it is expected that a stress that breaks the tetragonal magnetic symmetry will give rise to a large c_{14} [14].

The piezoelectric response in oxides is dominated by ionic polarisability and in Pb_2MnO_4, this will be large due to the off centre coordination of Pb^{2+}. The inequivalent Pb(1) and Pb(2) sites are coordinated by five and four oxygen's respectively, and the atomic coordinates in Table I allow the displacement vectors of the Pb^{2+} cations from the centres of their coordination spheres to be estimated. The directions of the Pb^{2+} displacements are shown in Fig. 6.5 and are seen to lie near-parallel to the *ab* plane. The induced polarisation $\boldsymbol{P}_i$ is related to the stress tensor $\boldsymbol{s}_j$ via the piezoelectric modulus $\boldsymbol{d}_{ij}$: $\boldsymbol{P}_i = \boldsymbol{d}_{ij}\boldsymbol{s}_j$. The crystal structure of Pb_2MnO_4 belongs to point group $\bar{4}2m$ and so the only non-zero piezoelectric coefficients are d_{14} and d_{36}. d_{14} is expected to be significant given the orientation of the Pb^{2+} displacements as above.

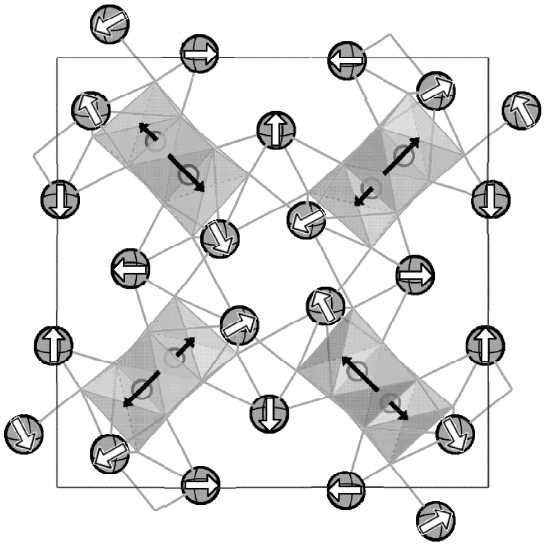

Figure 6.5: [001] projection of the crystal and magnetic structures of Pb_2MnO_4, with Pb^{2+} displacements marked as white arrows and Mn^{4+} magnetic moments as black arrows. MnO_6 octahedra are shaded and Pb-O bonds are shown as lines.

The piezomagnetic and piezoelectric coefficients in Pb_2MnO_4 hence have comparable symmetry and coupled properties may occur. A similar scenario is realised in composite magnetoelectrics, these combine a magnetostrictive phase and a piezoelectric phase, for example, $CoFe_2O_4$ and $BaTiO_3$. Applying a magnetic field yields a large polarisation via internal stresses, up to several orders of magnitude higher than that shown in single phase magnetoelectric materials [15]. We therefore identify Pb_2MnO_4 as a material likely to show stress coupled magnetoelectric effects and label this potential new class of materials 'multipiezos'. Initial attempts to measure the piezomagnetic response of Pb_2MnO_4 were unsuccessful as the polycrystalline pellets tend to crack under stress. Single crystals or epitaxial films of Pb_2MnO_4 may be necessary to observe the symmetry allowed piezo properties in Pb_2MnO_4.

6.3. Effect of Oxygen Stoichiometry on Structure and Magnetism in $Pb_3Mn_7O_{15}$

6.3.1. Structure of single and polycrystalline $Pb_3Mn_7O_{15}$

Single crystal intensities were recorded by the School of Chemistry crystallographic service at 100 K using a small hexagonal crystal. The data were indexed and refined by Mr. C. Spanswick in the $P6_3/mcm$ structure proposed by Calvert *et al* [11], data are given in Table III. A room temperature diffraction pattern was also recorded on a powdered sample of the single crystals using the synchrotron beamline ID31 at the ESRF with λ = 0.45621 Å. All of the peaks in the powder pattern could be indexed by the hexagonal model used for the single crystal refinement, however, significant broadening was present for all reflections. Together with preferred orientation, this prevented a good fit to this data set. A portion of the observed and calculated patterns, which illustrates these problems, is shown in Fig. 6.6.

Table III: Refined atomic positions for $Pb_3Mn_7O_{15}$ single crystal at 130 K. Lattice parameters are a = 9.9651 Å, c = 13.5123 Å. Wyckoff positions are Pb1 (*6g*), Pb2 (*6g*), Mn1 (*12i*), Mn2 (*8h*), Mn3 (*6f*), Mn4 (*2b*), O1 (*24l*), O2 (*12j*), O3 (*12k*) O4 (*12k*).

Atom	*x*	*y*	*z*
Pb(1)	0.6118(1)	0.6118(1)	0.75
Pb(2)	0.2652(1)	0.2652(1)	0.75
Mn(1)	0.8316(3)	0.1682(2)	0.5
Mn(2)	0.3333	0.6667	0.1460(3)
Mn(3)	0.5	0.5	0.5
Mn(4)	0	0	0
O(1)	0.49(1)	0.334(6)	0.08(1)
O(2)	0.520(5)	0.170(1)	0.25
O(3)	0.835(5)	0.835(5)	0.925(4)
O(4)	0.666	0.666.	0.065(4)

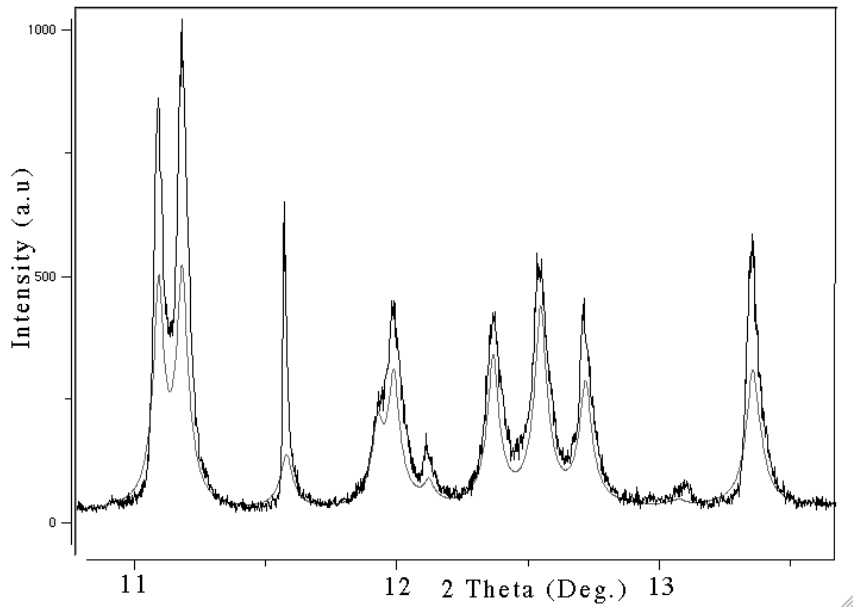

Figure 6.6:Section of observed (dark) and calculated (light) profiles for Rietveld fit to X-ray diffraction profile of powdered $Pb_3Mn_7O_{15}$ single crystals.

A room temperature X-ray diffraction pattern was also recorded for the polycrystalline (ceramic) sample of $Pb_3Mn_7O_{15}$ using ID31. This pattern contained multiple splittings that were not accounted for by the hexagonal model, but which could be indexed using the orthorhombic *Cmcm* model of Marsh *et al*. In this case, no problems with peak shapes or preferred orientation were observed. The peak shape was described by a pseudo-voight function and the background modelled by a linear interpolation function. Anomalous scattering corrections were calculated for lead and manganese using the program Fprime. The refinement converged with $\chi^2 = 10.96$, ${}_wR_p = 0.1642$ and $R_p = 0.1229$. The refined lattice parameters were $a = 17.29561(8)$, $b = 10.03624(4)$ and $c = 13.59789(6)$ Å. The observed, calculated and difference profiles are shown in Figure 6.7.

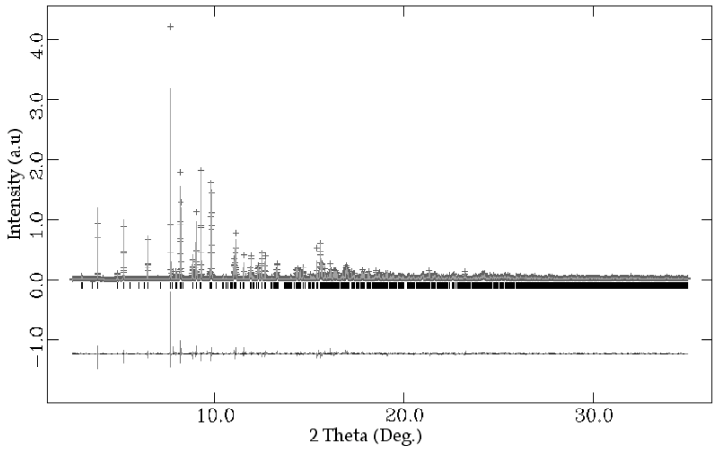

Figure 6.7: Observed, calculated and difference plots for the Rietveld fit to synchrotron X-ray diffraction profile of $Pb_3Mn_7O_{15}$ at room temperature.

The refined atomic coordinates and displacement parameters are shown in Table IV.

Table IV: Refined atomic coordinates and thermal displacement parameters for $Pb_3Mn_7O_{15}$ at room temperature from XRD. Wyckoff sites are: Pb1 (*8g*), Pb2 (*8g*), Pb3 (*4c*), Pb4 (*4c*), Mn1 (*8e*), Mn2 (*16h*), Mn3 (*16h*), Mn4 (*8d*), Mn5 (*4a*), Mn6 (*4b*), O1 (*16h*), O2 (*8g*), O3 (*16h*), O4 (*8f*), O5 (*8f*), O6 (*16h*), O7 (*16h*), O8 (*8g*), O9 (*8g*), O10 (*16h*).

Atom	Site	*x*	*y*	*z*	Uiso ($Å^2x10^2$)
Pb(1)	*8g*	0.19433(11)	0.18879(1)	0.25	1.779(23)
Pb(2)	*8g*	0.13172(10)	0.13929(1)	0.75	1.779(23)
Pb(3)	*4c*	0	0.26055(2)	0.25	1.779(23)
Pb(4)	*4c*	0	0.39495(2)	0.75	1.779(23)
Mn(1)	*8e*	0.16755(38)	0	0	0.82(4)
Mn(2)	*16h*	0.08335(27)	0.2541(4)	0.00217(35)	0.82(4)
Mn(3)	*16h*	0.16724(30)	0.4951(5)	0.14815(25)	0.82(4)
Mn(4)	*8d*	0.25	0.25	0	0.82(4)
Mn(5)	*4a*	0	0	0	0.82(4)
Mn(6)	*4b*	0	0.5	0	0.82(4)
O(1)	*16h*	0.2436(9)	0.0855(17)	0.0814(14)	0.77(13)
O(2)	*8g*	0.2380(14)	0.3991(24)	0.25	0.77(13)
O(3)	*16h*	0.0790(9)	0.4141(15)	0.9218(14)	0.77(13)
O(4)	*8f*	0	0.1652(24)	0.9297(20)	0.77(13)
O(5)	*8f*	0	0.3433(23)	0.4251(21)	0.77(13)
O(6)	*16g*	0.3375(10)	0.1718(17)	0.9174(14)	0.77(13)
O(7)	*16g*	0.0859(9)	0.0844(16)	0.0714(12)	0.77(13)
O(8)	*8g*	0.0828(16)	0.4336(28)	0.25	0.77(13)
O(9)	*8g*	0.1792(17)	0.3668(27)	0.75	0.77(13)
O(10)	*16g*	0.1665(9)	0.1747(17)	0.930(1)	0.77(13)

Synchrotron X-ray diffraction patterns were also recorded for the polycrystalline sample whilst cooling to 85 K. The orthorhombic peak splittings showed strong temperature

dependence, Fig. 6.8 shows the temperature variation of the splitting at the (110) hexagonal position.

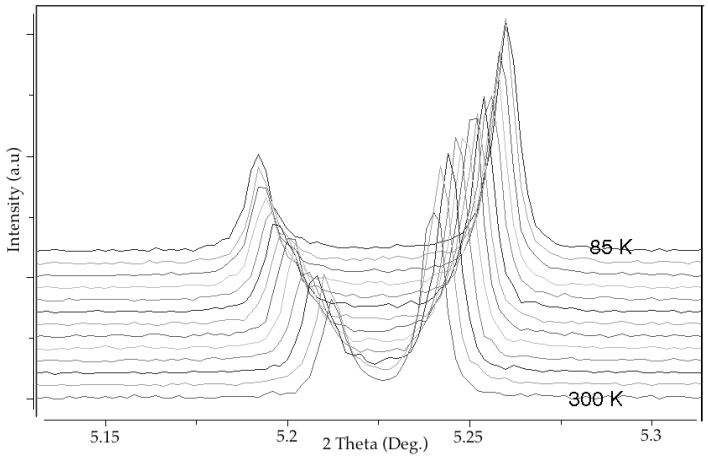

Figure 6.8: Temperature evolution of peak splitting at hexagonal (110) position.

Powder neutron diffraction data were also collected for the polycrystalline sample at 5, 25, 45, 65 and 85 K. Clearly resolved peak splittings were again observed, and same *Cmcm* model as the synchrotron X-ray data was refined. The observed, calculated and difference plots for the fit to the 85 K data set are shown in Fig. 6.9, the refinement converged with χ^2 = 7.49, $_wR_p$ = 0.0658 and R_p = 0.0516. The refined coordinates from the low temperature neutron diffraction data sets are shown in Tables VI - X in appendix one. As the neutron scattering lengths for lead (0.94 x 10^{-12} cm) , manganese (-0.39 x 10^{-12} cm) and oxygen (0.58 x 10^{-12} cm) are similar in absolute magnitude, the site occupancies were refined from the 85 K data set. The only sites whose occupancy differed significantly from unity were O(8) and O(9) with refined occupancies of 0.88(3) and 0.83(3) respectively. The overall stoichiometry of the polycrystalline material is therefore $Pb_3Mn_7O_{14.7}$.

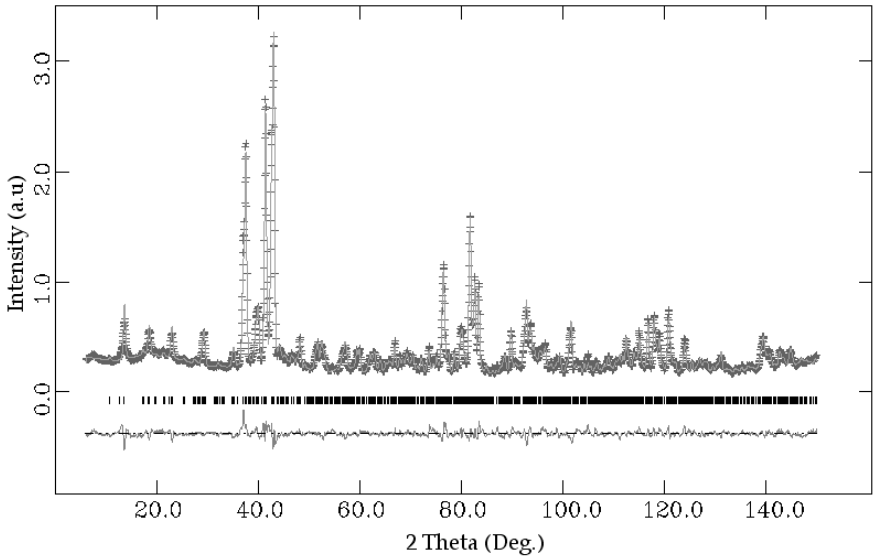

Figure 6.9: Observed, calculated and difference plots for the Rietveld fit to the powder neutron diffraction profile of $Pb_3Mn_7O_{15}$ at 85 K.

Bond valence sums for the polycrystalline material were calculated using the program Valence [16] from the 85 K neutron diffraction data set. The results are shown in Table V.

Table V: Bond Valence sums of manganese sites in polycrystalline $Pb_3Mn_7O_{15}$ calculated from Rietveld fit to 85 K neutron diffraction profile.

Manganese Site	Multiplicity	BVS (85 K, ND)
Mn(1)	*8e*	3.687
Mn(2)	*16h*	3.469
Mn(3)	*16h*	3.014
Mn(4)	*8d*	3.981
Mn(5)	*4a*	3.947
Mn(6)	*4b*	3.253

From these results it is clear that the polycrystalline material is partially charge ordered, the Mn(3) site (the ribbons linking neighbouring planes) is occupied by Mn^{3+} whilst the sites in the 1/2 filled Kagomé planes have a range of valences. By combining the neutron diffraction data and the X-ray diffraction data, it is possible to plot the temperature evolution of the cell parameters and volume (Fig. 6.10). The lattice parameters from the PND experiment were normalised to the values from the XRD experiment at 85 K. The lattice parameters *a*, and *c* contract normally over the temperature range 10 – 250 K, however *b* shows a smooth increase. The refined cell volume shows normal thermal contraction. Small anomalies are seen in all three lattice parameters just above 85 K, these could be the result of magnetostructural effects, or more likely, they are artefacts produced by the rapid cooling in the synchrotron powder diffraction experiment.

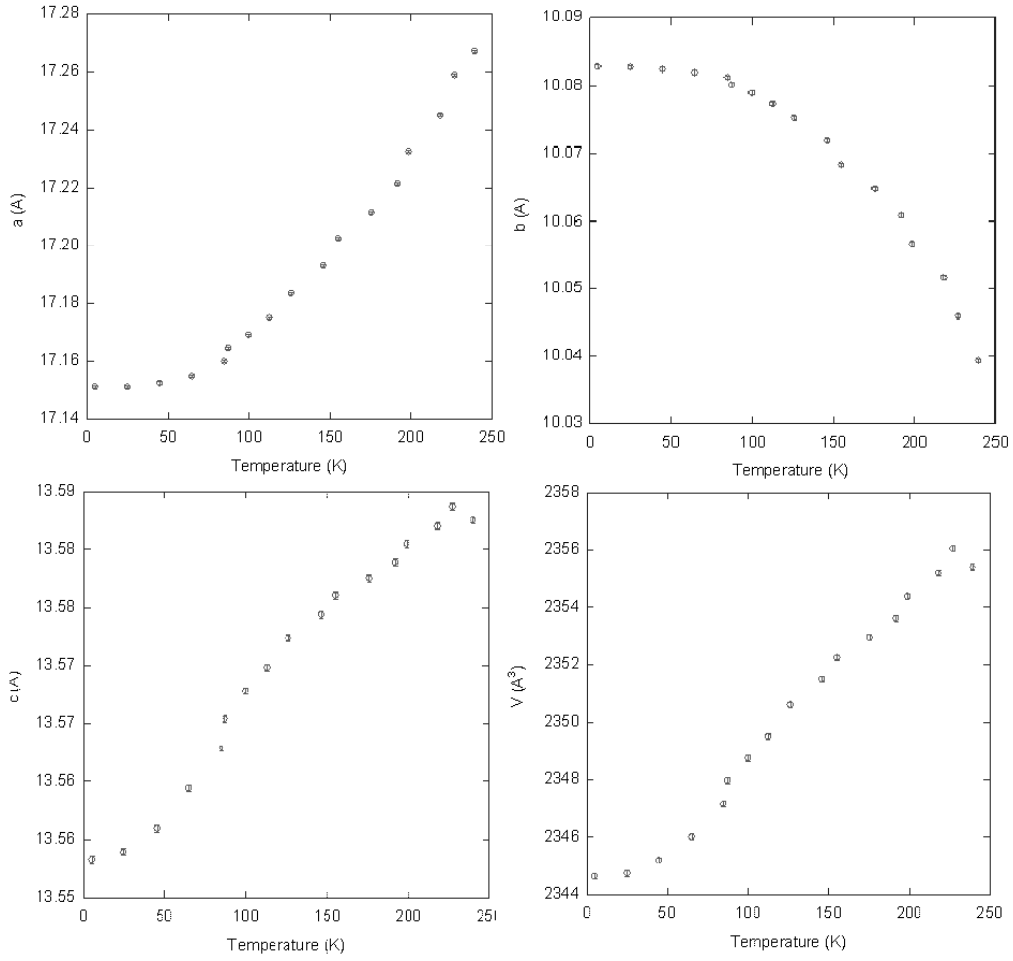

Figure 6.10: Refined lattice parameters and volume of polycrystalline $Pb_3Mn_7O_{15}$ from powder X-ray and neutron diffraction, error bars are smaller than symbols.

As shown in Fig. 6.11, the lattice parameters of $Pb_3Mn_7O_{15}$ tend towards a metrically hexagonal cell ($a/b = \sqrt{3} \approx 1.732$) above room temperature.

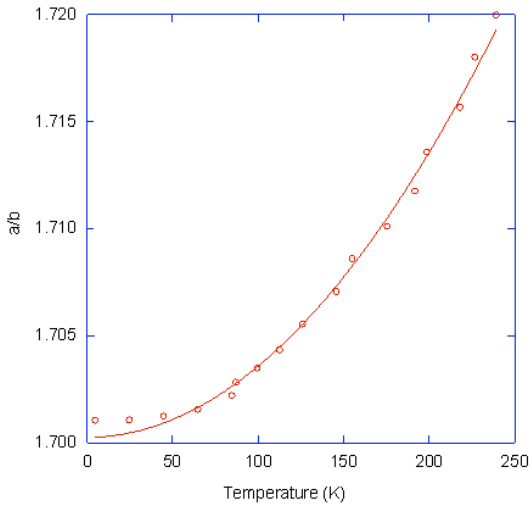

Figure 6.11: Ratio *a/b* plotted versus temperature for polycrystalline $Pb_3Mn_7O_{15}$,

6.3.2. Physical Properties of Single and Polycrystalline $Pb_3Mn_7O_{15}$

The magnetic susceptibilities of the powdered single crystal and polycrystalline sample were measured using a Quantum Design MPMS system. The susceptibilities for the powdered single crystals measured in a 500 Oe field over the range $1.8 < T < 300$ K are shown in Fig. 6.12.. A magnetic transition is observed at 55 K with divergence of the field and zero field cooled measurements. The inverse susceptibility obeys the Curie-Weiss law with a calculated moment of 3.43 μ_B per manganese, the Weiss constant is negative (-492 K), indicating strong antiferromagnetic superexchange interactions. The ratio $|\Theta|/T_N \approx 9$, implying geometrical frustration.

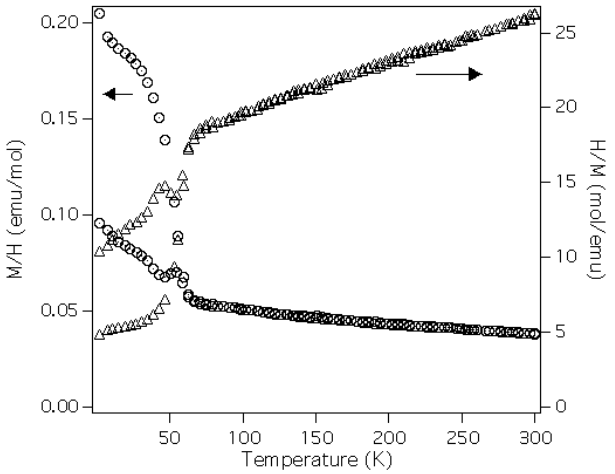

Figure 6.12: Field (500 Oe) and zero field cooled magnetic susceptibilities of powdered single crystal $Pb_3Mn_7O_{15}$.

The heat capacity of the single crystal sample of $Pb_3Mn_7O_{15}$ was measured in a 0 and 9 Tesla field using a Quantum Design PPMS over the range $2 < T < 200$ K (Fig. 6.13). No sharp Lambda anomaly, which would indicate a long range ordering transition, was observed in either measurement. Together with the divergence in the field and zero cooled susceptibilities, this implies spin glass behaviour. The heat capacity measured in a 9 T field is significantly lower over the range $55 < T < 200$ K. This is because an applied field aligns the magnetic moments in the paramagnetic regime, the magnetic entropy is therefore displaced to higher temperature.

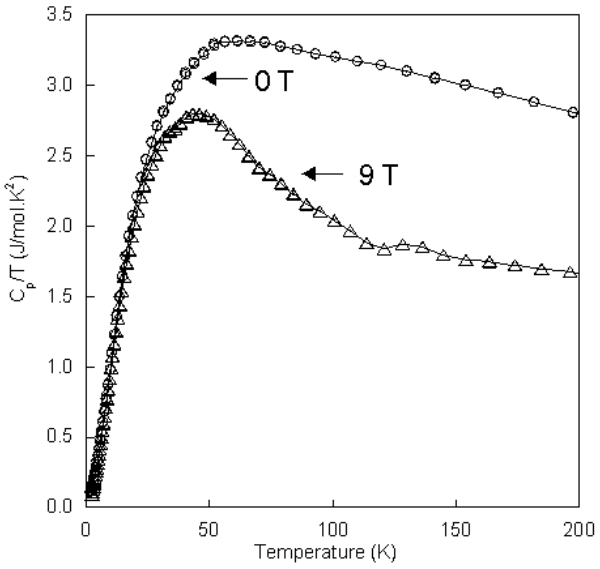

Figure 6.13: Heat capacity of $Pb_3Mn_7O_{15}$ single crystals measured in 0 and 9 Tesla field.

The magnetic susceptibilities of the polycrystalline $Pb_3Mn_7O_{15}$ sample were also measured in field (500 Oe) and zero field cooled conditions and are shown in Fig. 6.14.

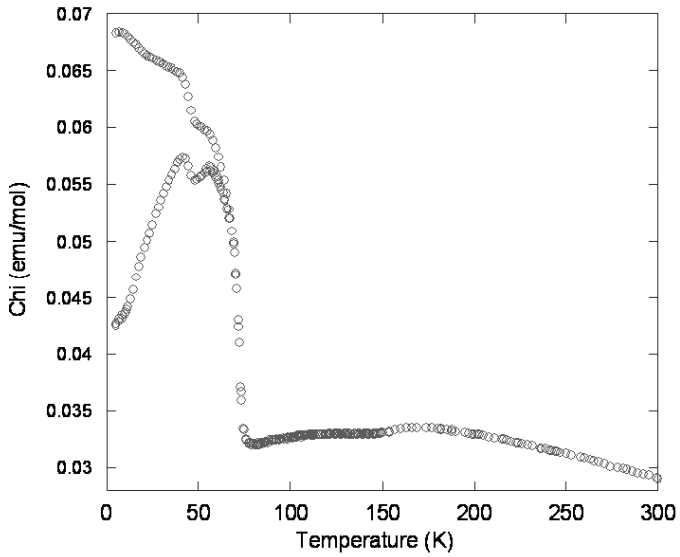

Figure 6.14: Field (500 Oe) and zero field cooled magnetic susceptibilities of polycrystalline $Pb_3Mn_7O_{15}$.

Several differences between the polycrystalline and single crystal samples are apparent, at high temperature there is a broad hump in both the zero and field cooled measurements, characteristic of short range antiferromagnetic order. Furthermore, an additional transition is seen at 45 K, this probably results from a trace of ferrimagnetic Mn_3O_4 impurity. Closer inspection also shows that the magnetic transition seen in the powdered single crystals has also shifted to higher temperature (75 K). The additional features present in this measurement prevent the fitting of a Curie Weiss law to the inverse susceptibility.

The resistivity of the polycrystalline material was also measured as a function of temperature (Fig 6.15). Semiconducting behaviour was observed, a plot of ln(ρ) vs. 1000/T is shown in the inset to Fig. 6.15, the calculated bandgap, E_g = 65(1) meV.

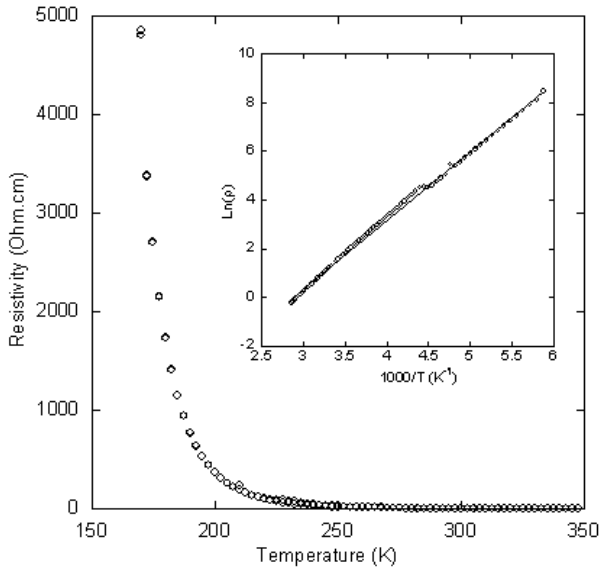

Figure 6.15: Resistivity of polycrystalline $Pb_3Mn_7O_{15}$ as a function of temperature, inset shows plot of ln(ρ) vs. 1000/T.

Field isotherms were also measured at several temperatures in order to check for evidence of magnetoresistance. The measured isotherm at 200 K is shown in Fig. 6.16, the maximum magnetoresistance (MR = [ρ(H) - ρ(0)/ ρ(0)] x 100 %) is ca. 1.6 % at 9 Tesla.

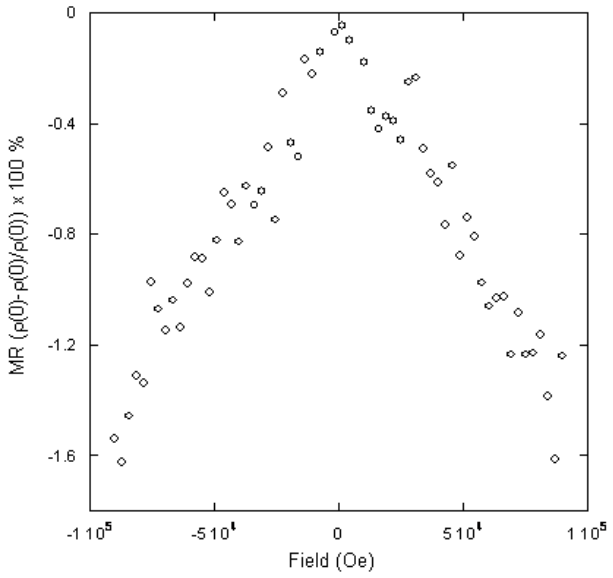

Figure 6.16: Magnetoresistance of polycrystalline $Pb_3Mn_7O_{15}$ at 200 K.

The low temperature neutron powder diffraction patterns collected for the polycrystalline sample of $Pb_3Mn_7O_{15}$ show the emergence of long range magnetic order. The low angle

portions of the observed diffraction profiles as a function of temperature are shown in Fig. 6.17.

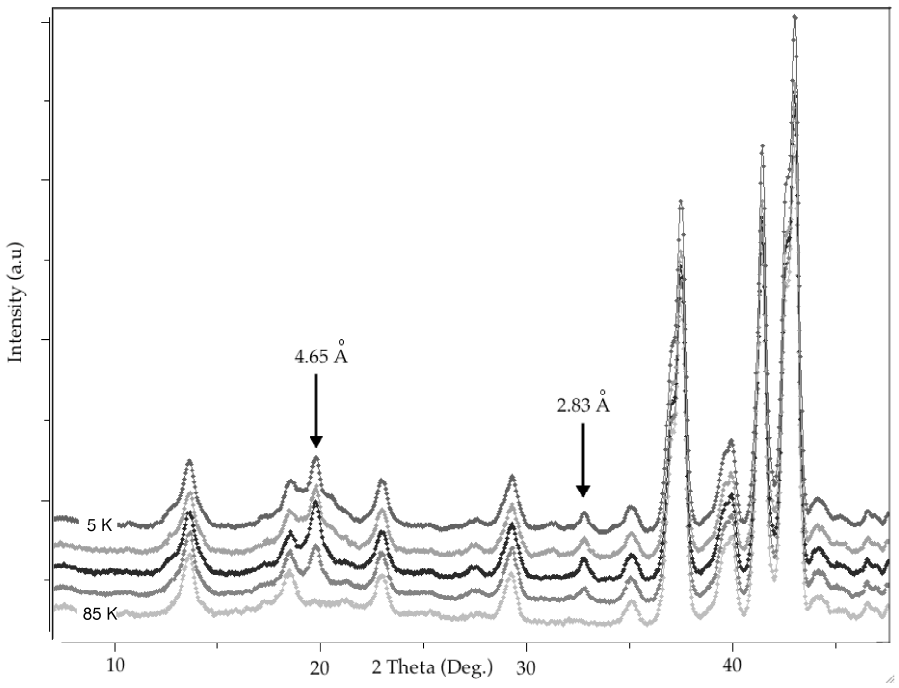

Figure 6.17: Low angle portion of neutron powder diffraction profile of $Pb_3Mn_7O_{15}$ at 5, 25, 45, 65 and 85 K.

Multiple attempts to find the propagation vector of this magnetic structure were performed. This procedure was complicated by the very large cell (17.1515(4) x 10.0832(3) x 13.5554(3) Å at 5 K) and the relatively short wavelength used (1.594 Å) giving many closely spaced reflection markers even with k = (0,0,0). Many of the magnetic peaks observed also appear to have satellite reflections (see for example, the peak at 4.65 Å in Fig. 6.15) this may be an indication of incommensurability. It should also be noted that the *Cmcm* cell for $Pb_3Mn_7O_{15}$ contains a total of 56 manganese sites, for comparison, the magnetic cell of Pb_2MnO_4 only contains 8. The magnetic structure of $Pb_3Mn_7O_{15}$ was not solved due to the inability to find a satisfactory propagation vector using the Super-D2B data.

6.3.3. Discussion

The results presented above show there are significant differences in the structural and magnetic properties of $Pb_3Mn_7O_{15}$ prepared in single and polycrystalline forms. In particular, the lattice symmetry of the polycrystalline material is lower (orthorhombic). The orthorhombic cellalso contains twice as many atoms as the hexagonal cell and is hence much larger. These observations may be rationalised by considering the small oxygen deficiency (≈ 0.3) shown by the polycrystalline product. The greater proportion of Jahn-Teller distorted Mn^{3+} requires a decrease in point symmetry at several manganese sites. Indeed,two of the manganese sites in the hexagonal structure, which both have three-fold point symmetry (*12l* and *6l*) split into sites with 8 + 16 and 8 + 4, multiplicity respectively as a direct result of this.

It seems likely that the difference in oxygen stoichiometry is also responsible for the different magnetic behaviour seen. The two oxygen sites (O(8), O(9)), which show reduced occupancies, are located on the ribbons joining the 1/2 filled Kagomé planes. Partial depletion of these sites will decouple neighbouring layers and may be the cause of the low dimensional feature at high temperature in the magnetic susceptibility of the polycrystalline product. The magnetic ground state of $Pb_3Mn_7O_{15}$ also seems to vary as a function of oxygen content from a spin glass like state to coherent long range order. A spin glass state is favoured in hexagonal $Pb_3Mn_7O_{15}$ due to the presence of both disorder (valence and bond) and frustration [17]. In orthorhombic $Pb_3Mn_7O_{15}$, partial charge ordering may remove some of the valence and bond disorder and favour a long range ordered magnetic groundstate. Further experiments (e.g. neutron diffraction and ac susceptibility measurements) will be required to confirm this picture. Variations of structural and magnetic properties with oxygen content are ubiquitous in transition metal oxides, examples include manganese perovskites [18] and layered ruthenocuprates [19].

6.4. Overall Conclusions

The basic structural and magnetic properties of two low dimensional lead manganese oxides containing Pb^{2+} lone pairs have been reported. In particular, the above

symmetry and structural considerations show that Pb_2MnO_4 is an excellent candidate multipiezo material for stress-induced magnetoelectric properties below the magnetic ordering temperature of 18 K. The acentric but non-polar crystal symmetry is unchanged down to 1.5 K, and the spin structure has a compatible symmetry. Furthermore, the Pb^{2+} displacements are approximately parallel to the ***ab***-plane, and the relatively large Mn^{4+} magnetic moments are also parallel to this plane, so that polarisation and magnetisation responses are anticipated via d_{14} and c_{14} when tetragonal symmetry is broken by an applied stress. Converse effects may also be observable, so that application of an electric or magnetic field will generate a strain via the converse piezoelectric or magnetostrictive effects.

The structure and physical properties of $Pb_3Mn_7O_{15}$ prepared in single and polycrystalline forms have been compared. Single crystals appear to be hexagonal, although broadening of the synchrotron powder X-ray diffraction profile evidences a high degree of inhomogeneity. This phase is seen to be a spin glass by a divergence in the field and zero field cooled susceptibilities and the absence of a lambda anomaly in the heat capacity. measurements. In contrast, the polycrystalline product is orthorhombic and partially charge ordered. Magnetisation and powder neutron diffraction measurements show that at least some of the moments undergo long range order at ca. 75 K. Unfortunately, the extremely complex magnetic structure was unsolved.

6.5. Future Work

Our initial attempts to observe a piezomagnetic response from sintered pellets of Pb_2MnO_4 were unsuccessful, and suitable single crystals or epitaxial films will be needed to provide experimental demonstrations of the expected properties. Future work for $Pb_3Mn_7O_{15}$ might include collecting long wavelength powder neutron diffraction data for the polycrystalline sample and applying group theory analysis once the propagation vector is known. Additionally, treating the polycrystalline material in flowing nitrogen to reduce the oxygen content still further may result in increased magnetoresitances.

Appendix 1: Results of Rietveld fits to powder neutron powder diffraction profiles of $Pb_3Mn_7O_{15}$ at various temperatures.

Table VI: Refined atomic coordinates and thermal displacement parameters for $Pb_3Mn_7O_{15}$ at 85 K from neutron diffraction.

Atom	Site	*x*	*y*	*z*	Uiso ($Å^2x10^2$)
Pb(1)	*8g*	0.1940(4)	0.1841(7)	0.25	1.15(6)
Pb(2)	*8g*	0.1304(4)	0.1434(7)	0.75	1.15(6)
Pb(3)	*4c*	0	0.2569(9)	0.25	1.15(6)
Pb(4)	*4c*	0	0.3981(9)	0.75	1.15(6)
Mn(1)	*8e*	0.1656(10)	0	0	0.50(6)
Mn(2)	*16h*	0.0836(7)	0.2588(11)	0.0006(9)	0.50(6)
Mn(3)	*16h*	0.1667(7)	0.4880(8)	0.1450(6)	0.50(6)
Mn(4)	*8d*	0.25	0.25	0	0.50(6)
Mn(5)	*4a*	0	0	0	0.50(6)
Mn(6)	*4b*	0	0.5	0	0.50(6)
O(1)	*16h*	0.2448(5)	0.0804(8)	0.0788(6)	1.33(4)
O(2)	*8g*	0.2434(7)	0.3962(10)	0.25	1.33(4)
O(3)	*16h*	0.0800(5)	0.4181(8)	0.9120(5)	1.33(4)
O(4)	*8f*	0	0.1604(11)	0.9298(8)	1.33(4)
O(5)	*8f*	0	0.3328(11)	0.4283(9)	1.33(4)
O(6)	*16g*	0.3312(5)	0.1803(6)	0.9252(6)	1.33(4)
O(7)	*16g*	0.0837(4)	0.0768(8)	0.0755(4)	1.33(4)
O(8)	*8g*	0.0922(7)	0.4278(12)	0.25	1.33(4)
O(9)	*8g*	0.1767(8)	0.3642(13)	0.75	1.33(4)
O(10)	*16g*	0.1678(5)	0.1744(7)	0.9308(5)	1.33(4)

Table VII: Refined atomic coordinates and thermal displacement parameters for $Pb_3Mn_7O_{15}$ at 65 K from neutron diffraction.

Atom	Site	*x*	*y*	*z*	Uiso ($Å^2x10^2$)
Pb(1)	*8g*	0.19409(34)	0.1815(6)	0.25	0.77(6)
Pb(2)	*8g*	0.13056(35)	0.1446(6)	0.75	0.77(6)
Pb(3)	*4c*	0	0.2558(8)	0.25	0.77(6)
Pb(4)	*4c*	0	0.3977(8)	0.75	0.77(6)
Mn(1)	*8e*	0.1656(10)	0	0	0.73(7)
Mn(2)	*16h*	0.0818(7)	0.2571(11)	0.0041(8)	0.73(7)
Mn(3)	*16h*	0.1634(8)	0.4846(9)	0.1436(6)	0.73(7)
Mn(4)	*8d*	0.25	0.25	0	0.73(7)
Mn(5)	*4a*	0	0	0	0.73(7)
Mn(6)	*4b*	0	0.5	0	0.73(7)
O(1)	*16h*	0.2442(4)	0.0823(8)	0.0806(6)	1.41(4)
O(2)	*8g*	0.2446(7)	0.3965(10)	0.25	1.41(4)
O(3)	*16h*	0.0813(5)	0.4164(8)	0.9140(6)	1.41(4)
O(4)	*8f*	0	0.1674(11)	0.9288(8)	1.41(4)
O(5)	*8f*	0	0.3306(11)	0.4251(9)	1.41(4)
O(6)	*16g*	0.3311(5)	0.1779(6)	0.9237(6)	1.41(4)
O(7)	*16g*	0.0823(5)	0.0799(8)	0.0750(5)	1.41(4)
O(8)	*8g*	0.0931(7)	0.4290(11)	0.25	1.41(4)
O(9)	*8g*	0.1772(8)	0.3639(13)	0.75	1.41(4)
O(10)	*16g*	0.1666(5)	0.1748(7)	0.9322(5)	1.41(4)

Table VIII: Refined atomic coordinates and thermal displacement parameters for $Pb_3Mn_7O_{15}$ at 45 K from neutron diffraction.

Atom	Site	*x*	*y*	*z*	Uiso ($Å^2x10^2$)
Pb(1)	*8g*	0.19414(34)	0.1818(6)	0.25	0.75(6)
Pb(2)	*8g*	0.13016(35)	0.1440(6)	0.75	0.75(6)
Pb(3)	*4c*	0	0.2557(8)	0.25	0.75(6)
Pb(4)	*4c*	0	0.3978(8)	0.75	0.75(6)
Mn(1)	*8e*	0.1678(10)	0	0	0.72(8)
Mn(2)	*16h*	0.0820(7)	0.2578(11)	0.0043(8)	0.72(8)
Mn(3)	*16h*	0.1631(8)	0.4850(9)	0.1434(6)	0.72(8)
Mn(4)	*8d*	0.25	0.25	0	0.72(8)
Mn(5)	*4a*	0	0	0	0.72(8)
Mn(6)	*4b*	0	0.5	0	0.72(8)
O(1)	*16h*	0.2438(4)	0.0822(8)	0.0800(6)	1.41(4)
O(2)	*8g*	0.2449(7)	0.3962(11)	0.25	1.41(4)
O(3)	*16h*	0.0811(5)	0.4172(8)	0.9147(6)	1.41(4)
O(4)	*8f*	0	0.1675(11)	0.9299(8)	1.41(4)
O(5)	*8f*	0	0.3310(12)	0.4247(9)	1.41(4)
O(6)	*16g*	0.3307(5)	0.1780(7)	0.9235(6)	1.41(4)
O(7)	*16g*	0.0826(5)	0.0802(8)	0.0755(5)	1.41(4)
O(8)	*8g*	0.0934(7)	0.4293(12)	0.25	1.41(4)
O(9)	*8g*	0.1770(8)	0.3619(14)	0.75	1.41(4)
O(10)	*16g*	0.1664(5)	0.1747(7)	0.9319(5)	1.41(4)

Table IX: Refined atomic coordinates and thermal displacement parameters for $Pb_3Mn_7O_{15}$ at 25 K from neutron diffraction.

Atom	Site	*x*	*y*	*z*	Uiso ($Å^2x10^2$)
Pb(1)	*8g*	0.19399(34)	0.1815(6)	0.25	0.72(6)
Pb(2)	*8g*	0.13043(36)	0.1444(6)	0.75	0.72(6)
Pb(3)	*4c*	0	0.2558(8)	0.25	0.72(6)
Pb(4)	*4c*	0	0.3979(8)	0.75	0.72(6)
Mn(1)	*8e*	0.1663(10)	0	0	0.60(7)
Mn(2)	*16h*	0.0819(7)	0.2591(11)	0.0043(8)	0.60(7)
Mn(3)	*16h*	0.1626(7)	0.4839(9)	0.1431(6)	0.60(7)
Mn(4)	*8d*	0.25	0.25	0	0.60(7)
Mn(5)	*4a*	0	0	0	0.60(7)
Mn(6)	*4b*	0	0.5	0	0.60(7)
O(1)	*16h*	0.2438(4)	0.0812(8)	0.0813(6)	1.36(4)
O(2)	*8g*	0.2448(7)	0.3967(11)	0.25	1.36(4)
O(3)	*16h*	0.0810(5)	0.4166(8)	0.9146(6)	1.36(4)
O(4)	*8f*	0	0.1687(11)	0.9291(8)	1.36(4)
O(5)	*8f*	0	0.3306(12)	0.4241(9)	1.36(4)
O(6)	*16g*	0.3306(5)	0.1783(7)	0.9240(6)	1.36(4)
O(7)	*16g*	0.0821(5)	0.0812(8)	0.0752(5)	1.36(4)
O(8)	*8g*	0.0932(7)	0.4299(12)	0.25	1.36(4)
O(9)	*8g*	0.1769(8)	0.3640(13)	0.75	1.36(4)
O(10)	*16g*	0.1666(5)	0.1748(7)	0.9322(5)	1.36(4)

Table X: Refined atomic coordinates and thermal displacement parameters for $Pb_3Mn_7O_{15}$ at 5 K from neutron diffraction.

Atom	Site	*x*	*y*	*z*	Uiso ($Å^2x10^2$)
Pb(1)	*8g*	0.19425(33)	0.1816(6)	0.25	0.69(6)
Pb(2)	*8g*	0.13030(35)	0.1446(6)	0.75	0.69(6)
Pb(3)	*4c*	0	0.2561(8)	0.25	0.69(6)
Pb(4)	*4c*	0	0.3979(8)	0.75	0.69(6)
Mn(1)	*8e*	0.1672(10)	0	0	0.67(8)
Mn(2)	*16h*	0.0822(7)	0.2588(11)	0.0040(8)	0.67(8)
Mn(3)	*16h*	0.1630(7)	0.4842(9)	0.1437(6)	0.67(8)
Mn(4)	*8d*	0.25	0.25	0	0.67(8)
Mn(5)	*4a*	0	0	0	0.67(8)
Mn(6)	*4b*	0	0.5	0	0.67(8)
O(1)	*16h*	0.2440(4)	0.0811(8)	0.0813(6)	1.31(4)
O(2)	*8g*	0.2449(7)	0.3966(10)	0.25	1.31(4)
O(3)	*16h*	0.0810(5)	0.4164(8)	0.9142(6)	1.31(4)
O(4)	*8f*	0	0.1689(11)	0.9291(8)	1.31(4)
O(5)	*8f*	0	0.3309(11)	0.4244(8)	1.31(4)
O(6)	*16g*	0.3303(4)	0.1784(6)	0.9244(6)	1.31(4)
O(7)	*16g*	0.0821(5)	0.0809(8)	0.0749(5)	1.31(4)
O(8)	*8g*	0.0934(7)	0.4297(11)	0.25	1.31(4)
O(9)	*8g*	0.1770(8)	0.3635(13)	0.75	1.31(4)
O(10)	*16g*	0.1665(5)	0.1746(7)	0.9319(5)	1.31(4)

Table XI: Refined lattice parameters from powder neutron diffraction.

Temperature (K)	*a* (Å)	*b*(Å)	*c*(Å)
85 K	17.1570(4)	10.0795(2)	13.5625(3)
65 K	17.1553(3)	10.0823(2)	13.5616(3)
45 K	17.1529(4)	10.0828(2)	13.5580(3)
25 K	17.1518(4)	10.0831(2)	13.5561(3)
5 K	17.1515(4)	10.0832(2)	13.5553(3)

References

[1] N. Hur, S. Park, P.A. Sharma, J.S. Ahn, S. Guha, S.W. Cheong, *Nature*, 2004, **429**, 392

[2] L.C. Chapon, G.R. Blake, M.J. Gutman, S. Park, N. Hur, P.G. Radaelli, S.W. Cheong, *Phys. Rev. Lett*, 2004, **93**, 177402

[3] G.R. Blake, L.C. Chapon, P.G. Radaelli, S. Park, N. Hur, S.W. Cheong, J. Rodriguez-Carvajal, *Phys. Rev. B*, 2005, **71**, 214402

[4] L.C. Chapon, P.G. Radaelli, G.R. Blake, S. Park, S.W. Cheong, *Phys. Rev. Lett*, 2006, **96**, 097601

[5] Y. Shimakawa, Y. Kubo, T. Manako, *Nature*, **379**, 53 (1996)

[6] M.A. Subramanian, B.H. Toby, A.P. Ramirez, W.J. Marshall, A.W. Sleight, G.H. Kwei, *Science*, **273**, 81 (1996)

[7] A. Teichert, H.K. Muller-Buschbaum, *Z. Anorg. Allg. Chem.*, **598/599**, 319 (1991)

[8] P.S. Halasyamani, K.R. Poeppelmeier, *Chem. Mat.*, **10**, 2753 (1998)

[9] B. Darriet, M. Devalette, B. Latourrette, *Acta. Cryst. B*, **34**, 3528 (1978)

[10] R.E. Marsh, F.H. Herbstein, *Acta. Cryst. B*, **39**, 280 (1983)

[11] Y. Lepage, L.D. Calvert, *Acta. Cryst. C*, **40**, 1787 (1984)

[12] W.I.F. David, *J. Appl. Cryst.*, **19**, 63 (1986)

[13] A.S. Borovik-Romanov, *Sov. Phys. JETP*, **11**, 786 (1960)

[14] International Tables for Crystallography: Volume D (Kluwer Academic Publishers, Dordrecht, 2003)

[15] C.W. Nan, *Phys. Rev. B*, **50**, 6082 (1994)

[16]I.D. Brown, *Acta. Cryst. B.*, **48**, 553 (1992)

[17] J.A. Mydosh, *Spin Glasses: An Experimental Introduction* (Taylor and Francis, London, 1993)

[18] C. Ritter, M.R. Ibarra, J.M. De Teresa, P.A. Algarabel, C. Marquina, J. Blasco, J. Garcia, S. Oseroff, S-W. Cheong, *Phys. Rev. B*, **56**, 8902 (1997)

[19] A.C. Mclaughlin, L. Begg, C. Harrow, S.A.J. Kimber, F. Sher, J.P. Attfield, *J. Amer. Chem. Soc.*, **128**, 12364 (2006)

List of Publications

S.A.J. Kimber, A.C. Mclaughlin, J.P. Attfield, *High Pessure Neutron Diffraction Study of the Magnetosresistive Ruthenocuprate,* $RuSr_2Nd_{0.9}Y_{0.2}Ce_{0.9}Cu_2O_{10}$, Materials Research Bulletin, **41**, 1001 (2006)

A.C. Mclaughlin, L. Begg, C. Harrow, S.A.J. Kimber, F. Sher, J.P. Attfield, *Chemical Tuning of Positive and Negative Magnetoresistances, and Superconductivity in 1222-Type Ruthenocuprates,* Journal of the American Chemical Society, **128**, 12364 (2006)

S.A.J. Kimber, J.P. Attfield, *Disrupted Antiferromagnetism in the Brannerite* MnV_2O_6, Physical Review B, **75**, 064406, (2007)

A.C. Mclaughlin, F. Sher, S.A.J. Kimber, J.P. Attfield, *Induced Antiferromagnetism and Large Magnetoresistance in* $RuSr_2(Nd,Y,Ce)_2Cu_2O_{10-\delta}$ *Ruthenocuprates*, Physical Review B, **76**, 094514 (2007)

S.A.J. Kimber, J.P. Attfield, *Magnetic Order in Acentric* Pb_2MnO_4, Journal of Materials Chemistry, **17**, 4885 (2007)

S.A.J. Kimber, M.A. de Vries, J. Sanchez-Benitez, K.V. Kamenev, J.P. Attfield, *Triplet Dimerisation Crossover in* In_2VO_5, Physical Review B, **77**, 014428 (2008)